A Study on Processing and Analysis of Biomedical Temporal-Quasiperiodic Information using Statistical and non-Stationary Methods

September 2021

Patashov Dmitry

A Study on Processing and Analysis of Biomedical Temporal-Quasiperiodic Information using Statistical and non-Stationary Methods

Graduate School of Science and Technology

Degree Programs in Systems and Information Engineering

University of Tsukuba

September 2021

Patashov Dmitry

Table of Contents

Abstract

In this study we present methods for processing of the biomedical information that take into consideration the limitations, unique characteristics and challenges of this field. One of the common routines of biomedical information analysis is the detection of extrema points within the data. For that, we proposed a method called Sequential Desmoothing Extremum Tracking (SDET). This algorithm allows for the automatic detection of the extrema points of quasi-periodic, noisy signals. The approach is robust and insensitive to noise or variations of the signal's cycles. This method was shown to work reliably on different types of biomedical signals, provided the correct subroutines. Additional dedicated solutions were proposed for obstacle avoidance strategy assessment in the study of human gait. Gait Related Potential (GRP) variability assessment procedure named Amplitude Pattern Variability (APC) was presented in gait assessment using electroencephalography (EEG). A novel algorithm called Cumulative Curve Fitting Approximation (CCFA) is presented for missing samples approximation, resampling and signal filtration. It was used in a study of human gait for accurate approximation of the missing samples within the recorded data. When compared to the conventional methods, CCFA's performance was more accurate by a large margin. Just like SDET, it was shown to work accurately on different types of biomedical signals. In the study of human brain using fNIRS technology, CCFA based filtering provides a robust and reliable solution for the removal of the time-dependent first statistical moment (i.e. signal drift). For the removal of high-frequency contamination sources, Intrinsic Component Filtering (ICF) method was developed. ICF uses Empirical Mode Decomposition (EMD) that was presented in Hilbert-Huang Transform (HHT) as its core to avoid any stationarity assumptions. The performance of these filtering techniques was assessed using simulated short-Hemodynamic Response Function's (sHRF) signals. The comparison demonstrates that CCFA and ICF decouple the simulated sHRF from the noise with a higher fidelity and Signal to Noise Ratio (SNR) in comparison to Discrete Cosine Transform (DCT) and spectral based filtering as proposed in the widely used NIRS-SPM toolbox. Artifact detection methods: Maximal Variability Expectation (MVE), Cross Segment Validation (CSV) and spike detection using the 3 scaled Median Absolute Deviations (sMAD) away from the median, outlier detection are proposed. MVE is shown to be able to detect coupling artifacts within the fNIRS data with a very high accuracy. CSV provides a reliable detection of motion artifacts. sMAD based detection of the outliers together with MVE and CSV provides a full integrity map of the recorded data. The integrity map shows the quality of the recorded data in regard to artifact occurrences as well as providing their exact locations within the signals.

Keywords

Biomedical Signals, CCFA, DCT, Detrending, EEG, EMD, Extrema Detection, fNIRS, Gait Analysis, GLM, HRF, Missing Data, Noisy Signals, non-Stationary Signals, Quasi-Periodic Signals, SNR.

Introduction

General

The field of information processing and analysis is very broad. It overlaps with countless of other fields, for example: Electrical Engineering, Communications Engineering, Biomedical Engineering, Smart devices/vehicles/houses, and many more. Temporal information is one of the main types of assessed information since every action, sampling procedure or state can be observed in time to understand its behavior and patterns. Understanding how a certain process behaves in time can teach us many things about the nature of that process. This, in turn will allow us to better understand the phenomena that the process originated from. Understanding the natural phenomena allows us to use that knowledge to improve our technologies in the related fields. In most cases of quasi-periodic and state-based phenomena it is possible to predict future behavior and states to come. Being able to accurately predict future behavior of the phenomena, allows us to prepare in advance and use it for our purposes. It should be noted that the methods for processing and analysis of temporal information are applicable for many other, not temporal types of information. For example, methods used in multi-dimensional signal processing can be applied for temporal information as well as for spatial information processing, or at that point, for any process that has at least one dependent and one independent variable. The field of computer vision is a good example of information that can be treated as a multi-dimensional signal. The image can be seen as a collection of samples of a 2-dimentional function, where the coordinates of a pixel are the independent variables, while the value (or vector of values) of that pixel is the dependent one. Following this logic, video becomes a temporal information possessing one more independent variable which is time. This shows how broad this field is and how many different applications there are for the methods developed in this field.

Biomedical field has a long history and is quickly progressing. Nowadays, most of the information collected for biomedical purposes is digital and a lot of efforts are made to digitalize the information collected before global digitalization took place. The reason for wanting to digitalize every bit of information is the ability to quickly process and analyze it using advanced technologies and state of the art algorithms. The utilization of modern technologies and advanced methods allows to study phenomena faster and more accurately, in turn allowing for faster and more accurate disorder and disease diagnoses and treatments. The knowledge and understanding of certain phenomena, may not only help to improve the treatment, but also allow for preventive procedures to take place. The vast majority of the information collected in the biomedical field is temporal. This is due to the fact that almost all biological processes are time dependent, thus the best way to understand them is to analyze their behavior in time. A large number of biomedical information sources are also quasi-periodic. Thus, the usage of techniques dedicated to quasi-periodic information analysis is also important. Most of the processes in this field are non-stationary. Non-stationarity increases the complexity of the processing and analysis stages. Therefore, in order to achieve high accuracy, reliable results, it is essential to use non-stationary and in some cases non-linear methods.

Information processing and analysis is very important and unavoidable field for improving our knowledge, understanding, and as a result, our technologies. It is being widely studied in every corner of the globe, by countless researchers, scientists and engineers. Every day, new discoveries are made, novel methods are developed and modern technologies are utilized to collect, process and analyze information from various sources and fields. Among those fields, biomedicine is one of the leaders in terms of interest, information accumulation and funding. This is because biomedicine is directly related to the wellbeing, life span and the quality of life of people, animals and other lifeforms. Thus making it one of the most important fields for research. For many years, biomedicine was mainly researched by people who specialized in medicine, biology or alike. Today, in the era of digital technologies, this field is changing drastically. Mathematicians, engineers and other exact sciences' specialists widely research the field, introducing new ideas, methods and solutions for processing and analysis of the biomedical information. This already broad and complicated field is becoming even larger and more complex than ever before. The multi-disciplinarity of the modern-day biomedicine requires specialists from various disciplines to work together. That said, at this time, the majority of researchers in the field, come from biomedicine related backgrounds. The community of exact science's specialists working in this field is still comparably small, even though it is growing rapidly. This leads to the circumstances where biomedicine specialists have to learn fields like engineering and mathematics, for example, to perform a reliable and advanced research in the field. Sometimes, it leads to incorrect usage of some methods. In some extreme cases, those methods can even become a "gold standard" for some procedures, even though there are major fundamental issues in their applications. A good example of misused approaches is the usage of methods that assume stationarity of the process, being used on a non-stationary process. Sometimes, it may produce some meaningful results and even progress the field, while in others it may completely distort the results and conclusions of the study. It is important to fully understand the limitations and the advantages of each method in order to use them properly. The commonly used approach of referencing a successful usage of a method in a similar study to justify its use in another one, may not always be correct when dealing with complex biological systems and advanced algorithms. In the field of biomedicine, it is important to understand when and how to use the methods, and to understand the unique characteristics of the biomedical information. Therefore, it is essential to consult and collaborate with specialist from both spheres (biomedicine and exact sciences) in order to provide robust and reliable solutions.

Background

Today, in the digital era of biomedicine, information processing and analysis methods are drastically changing. Thanks to the advanced computational abilities of modern technologies, digital data analysis provides more accurate and reliable results much faster than before. It allows the biomedicine specialists to reach conclusions and to accumulate knowledge very quickly. Digital information processing and analysis methods are playing a big role in the progress of biomedical field, since a large portion of the biomedical data is in digital form. Processing and analysis tools, methodologies and algorithms from many fields are quickly adopted into the field of biomedicine. Though the adaptation of new techniques is essential for the growth of the field, it also brings its own issues with it. It is not uncommon to see exact sciences' specialists using methods that neglect certain biomedical factors or biomedicine specialists using models that are not suitable for the task.

The aim of this study is to develop methods dedicated to processing and analysis of the biomedical information. By involving specialists from the relevant fields, we aim to provide solutions for biomedical information analysis issues while taking into consideration the limitations of both biomedicine and exact sciences. Many of the algorithms currently used in the field are general purpose solutions that are not designed with biomedicine as their primary use. When used correctly, those methods indeed, provide good quality results. That said, just like in many other fields, solutions that are designed specifically for biomedical engineering, usually provide better results. That is also true if those methods are applicable as general-purpose solutions. Methods from other fields can and should also be used in the field of biomedicine. However, it is important to adapt them to the unique qualities of the biomedical information. Which is one of our tasks as well. By properly adopting and integrating the methods from other fields, we further contribute to the growth of the biomedical field.

Gait Analysis

Gait abnormalities and falls are omnipresent among older adults and patients with common neurological diseases. In fact, more than twenty percent of older people worldwide fall every year [1]. Although falling once increases the chances of falling again [2], only one of two older subjects report the fall to their doctor [1]. Based on these statistics, it is evident that studying the risks of falls among older adults and methods to reduce those risks is an important task. Advancements in this field may significantly improve the quality of life of people with gait abnormalities.

Gait assessment is an important component of both neurologic and orthopedic examinations. Visual gait analysis provides significant contribution to the diagnosis of neuromuscular disorders, treatment planning and follow-up. However, three-dimensional motion of the lower limb segments during walking cannot be visually observed simultaneously in all planes. 3D motion analysis systems have been used to overcome these and other limitations of visual gait assessment. These systems present extracted gait cycle parameters in the form of graphs for the use of clinicians with knowledge about functional anatomy, neural control of locomotion, muscle and motion mechanics, and kinesiological electromyography to interpret these data [3].

Quantitative gait analysis while walking on a treadmill was reported in several studies ([4]–[7]). The advantage of this approach is the possibility of controlling speed and environmental factors. In recent years, there has been a growing interest in studying kinematic patterns, features and alterations of gait while walking on a treadmill ([8]–[11]) using measuring devices, sensors and video logging. One of the main interests is to test the putative effect of integrating treadmill training with a virtual reality environment on gait performance ([12]–[14]). V-TIME is a treadmill-training program augmented by virtual reality (VR) to decrease fall risk in older adults [15]. This program provided evidence to the added value of VR treadmill-training to address motor-cognitive interactions [15] and advantage in reducing falls and fall risk as compared to treadmill training alone ([16], [17]). However, the patterns of gait improvement while walking on the treadmill were not evaluated as of yet.

In order to study gait performance, in general, and gait improvement, in specific, kinematic properties should be extracted and analyzed. Extremum detection is essential for many applications including gait analysis. There are many algorithms for detection of local extremum, however, some of them are not suited for noisy and/or quasi-periodic signals ([18], [19]), while others usually require many input parameters or are restricted to a very specific type of signal ([20]–[22]). Scholkmann et al. [23] tackled that problem and have reported reasonable results. A major limitation of their suggested algorithm is, however, that it is very dependent on the signal's average period and does not have the flexibility to choose which wave pattern to track. In other words, it provides the extrema locations only of the most frequent waveform. Furthermore, Scholkmann et al. [23] made an assumption about a frequency range, which may be incorrect in some particular cases. Du et al. [24] propose a continuous wavelet transform-based pattern matching algorithm that they used for peak detection in mass spectrum, but it can also solves a variety of other, more general, peak detection problems. On one hand, this algorithm requires an approximation of a waveform to be detected and a few thresholds that may be hard to approximate, on the other hand, if provided with accurately approximated parameters, produces very promising results. Du et al. [24] present a method that is not restricted to quasi-periodic signals, but at the same time is less flexible in cases that were present in our data, where a system error would split a wave form into two similar waves. In such case, the algorithms proposed by Du et al. [24] would either not detect a peak in that period or detect two peaks instead of one, depending on the predetermined parameters.

In order to study the changes of gait due to obstacle avoidance task, automatic detection of change in walking pattern is essential. For such, signal segmentation methods can be used. Signal segmentation techniques that are based on abrupt changes in the signal [25] are well suited for the detection of step above obstacle, but are less reliable when trying to detect preparation and recovery in obstacle avoidance process, especially when a treadmill based system is used. This is due to a constant pace dictated by the treadmill making the changes in the walking pattern more meager. Methods utilizing the changes in signal power [26] are affected by the time-dependent changes in the first statistical moment (time-dependent expectancy or time-dependent first statistical moment). Though it can be removed, doing so would affect the behavior of the signal indicating the preparation and recovery related to obstacle avoidance. Hence, resulting in inaccurate segmentation. Preparation and recovery phases near the obstacle have overlapping characteristics with the drift of the signal itself, thus cannot be separated. Wavelet based algorithms [27] can be a powerful tool when a sudden change occurs in frequency pattern. In our case, the frequency patterns in close proximity to the obstacle may change significantly, but preparation and recovery regions are not affected as much and can be almost undetectable using these techniques.

For several reasons some sampling systems experience data loss while recording. Unfortunately, the system used in this study was no exception. To improve the quality of assessment, the missing information should be restored or approximated when possible. Commonly used methods for approximation of missing samples are interpolations. The most basic approach is to perform a Linear or Spline Interpolation [28]. Although this approach is frequently used, the accuracy of its results is usually dependent on a type of the signal and its patterns. Auto Regressive (AR) models [29] tend to be more robust to the type and structure of the signal. They usually provide more accurate results than Interpolation methods, thus they are also popular for missing data approximation.

To accommodate for the issues explained above, two general purpose methods and one tailormade solution were developed. Algorithm named Sequential Desmoothing Extremum Tracking (SDET) ([30], [31]) was proposed as a solution for peak detection within noisy, quasi-periodic data. The procedure presented in [30] was adjusted to the specifics of the data collected from V-Time system. A combination of signal segmentation technique and a kernel-based clustering method was proposed for the detection of the preparation and recovery phases, as well as for the detection of abnormal steps related to obstacle avoidance task. Missing samples approximation method named Cumulative Curve Fitting based Adjustment (CCFA) [30] was also presented. In the following studies, as well as in this work, this method is called Cumulative Curve Fitting Approximation (CCFA). The experimental research was funded by the European Commission and done in collaboration between multiple research institutions worldwide. The developed algorithms and solutions were developed based on the needs and requirements of Tel Aviv Sourasky Medical Center's: Center for the study of Movement, Cognition and Mobility (CMCM), Department of Neurology in Israel and were used by their researchers to process and analyze the collected data.

Gait and the Brain

Gait is one of the keys to functional independence. Walking is achieved by coordinated movements of body segments while integrating external and internal factors. It is now well established that gait is controlled and defined by higher cognitive processes involving complex neural networks that incorporates sensory information with motor adaptation ([32], [33]). Hausdorff et.al. [34] and Yogev-Seligmann et.al. [35] show that adding a simultaneous task to walking taxes executive function and attention, and leads to changes in gait performance. This effect is exacerbated with ageing and neurodegenerative diseases such as Parkinson's Disease (PD) ([33], [35], [36]), and is related to falls [36] providing indirect evidence of the importance of the interconnection between motor and cognitive functions during walking.

In recent years, various neuroimaging techniques were used to study the role of cognitive resources during walking. fMRI studies used motor imagery ([37], [38]) and alternating movements of feet ([39], [40]) to mimic gait in the scanner. These studies reported increased activation in various frontal regions related to the attentional networks ([37], [38], [40]), however the findings are limited as they do not directly capture actual gait. Recent studies using functional Near Infrared Spectroscopy (fNIRS), a neuroimaging technique measuring blood oxygenation levels from the brain convexity during actual walking, showed increased activation of the prefrontal cortex in healthy young and older adults during dual task walking, as compared to usual walking ([41]–[43]). Patients with PD presented similar findings but also showed increased activation already during usual walking [44] suggesting a reliance on cognitive resources already during simple tasks. However, similar to fMRI, the temporal resolution of the fNIRS is low and it measures hemodynamic responses only in specific superficial areas of interest, unable to distinguish isolated effects from network function [45].

Spontaneous electroencephalographic (EEG) recording as well as event-related potentials (ERPs) are direct measurements of neuronal activity, with high temporal resolution, that can be applied during walking. In recent years, the use of EEG to explore the neural mechanism of gait is starting to emerge ([46]–[49]). The high temporal resolution of EEG allows for the assessment of the coupling between gait cycle phases and electrical activity, and reveal the neurophysiology of gait. Most studies utilized Event Related Spectral Perturbation (ERSP) to identify alterations in the EEG oscillations of different frequency bands during a gait cycle ([46]–[49]). The main finding was that neural oscillations of alpha, beta, and gamma frequency bands are modulated and time locked to gait cycle phases in specific brain areas such as the sensorimotor cortex and the supplementary motor cortex ([46], [48], [50]). Variations in ERP responses including amplitude, polarity, distribution, and latency have been associated with various cognitive measures ([51]–[53]). Changes were mainly observed in P300, the most studied ERP related to attention and cognitive decline, elicited using the ‘‘oddball” task. Task in which a random sequence of stimuli is presented and subjects are required to mentally count the rare target events [54]. Accumulating evidence from EEG and fMRI studies show that P300 generation stems from the connection between frontal lobe and hippocampal/temporoparietal function ([55]–[57]). It has been suggested that frontal areas account for the attention mechanism that directs neural responsivity to a new stimulus ([58], [59]), whereas the tempo-parietal regions correspond to the attentional resources used to maintain memory entries ([55], [60]). Patients with PD have decreased P300 amplitude and increased peak latency during sitting tasks as compared to healthy older adults and as the severity of cognitive dysfunction increases [61]. Although these changes in P300 were highly sensitive to cognitive decline and attentional impairments [62], they were also observed in other pathologies such as Alzheimer's disease [63] showing low specificity.

In our study [64], we combined the oddball task with walking to evaluate the dual-task effect of an attentional demanding task while walking in healthy young adults, healthy older adults and patients with PD. Using this approach, we aimed to reveal specific changes in P300 while walking and dual-tasking in older adults and patients with PD. The high temporal resolution EEG findings provide an additional layer to our knowledge regarding executive function deficits in aging and PD demonstrating new direct evidence of the physiological recruitment of attentional networks during walking and their impact by ageing and disease [64]. ERP is a direct measurement of neuronal activity that is commonly used in neurocognitive science. Variations in ERP responses including amplitude, polarity, and latency have been associated with various motor and cognitive impairments ([51], [53], [65]). This approach can also be applied to gait analysis and variations in ERPs of a gait cycle can be measured to evaluate motor and cognitive interactions, aging and dual tasking [31]. There are no reports of work examining ERPs during a gait cycle but as gait is an automatic learned function, one would expect that it would generate a specific electrical potential that will have a recognized pattern similar to that of cognitive response [31]. The studies used EEG to explore the effects of dual tasking on electrical activity mainly concentrate on attention and cognitive decline elicited during "oddball" and "visual Go-NoGo" tasks ([64], [66]). Relative delay and attenuation of these ERPs were observed during walking compared to standing in young and older adults ([64], [66]). These findings suggest that walking increases the motor-cognitive load that in turn reduces the attentional processing speed and prolongs latency [64]. However, changes in the electrical pattern induced by a cognitive task performed during gait have not been evaluated. It is most likely that activation of neural networks associated with the cognitive task will interact with motor networks that elicit the electrical pattern of gait [31].

To evaluate the dual-task effect of an attentional demanding task while walking, we combined the oddball task with walking and assessed the ERP measurements [64]. Next, we explored the stereotypical electrical brain pattern during gait cycle, Gait Related Potential (GRP), and investigated the effects of aging and a secondary attentional, dual task on this pattern [31]. One of the main challenges when assessing GRP is the strong noise resulting from motion. The conventional methods of assessment provide faulty results due to being overwhelmed by these noise. Algorithm SDET ([30], [31]) was used to overcome the noise interference when detecting GRPs and evaluating their parameters. A new analysis procedure named: Amplitude Pattern Consistency (APC) [31] was proposed for comparison of different subject groups. This research was conducted in collaboration with Tel Aviv Sourasky Medical Center's: Laboratory for Early Markers of Neurodegeneration (LEMON) in Israel. All of the solutions were developed in respect to the requirements set by the researchers from the medical field and used by them for the processing and analysis of the collected data.

Brain Research

Near infrared spectroscopy (NIRS) is used to study variations in cerebral hemodynamics and oxygen saturation during predetermined tasks and at rest [67]. During the past three decades, functional NIRS (fNIRS) has shed light on the hemodynamic response to cognitive, visual and motor tasks, as well as assessed hemodynamic connectivity (sometimes referred to as functional or resting state functional connectivity) ([68], [69]). However, despite an extensive research activity by hundreds of researchers ([45], [70]), there are currently no widely accepted clinical applications, based on fNIRS, that enable diagnosis or monitoring of brain health or disease. One of the reasons for this is the lack of accepted protocols and algorithms that outline the required preprocessing steps and pipeline for analyzing fNIRS signals, as are available for functional Magnetic Resonance Imaging (fMRI)[71].

NIRS measurements are based on detection of red and near-infrared light that travels through perfused tissue. Light is introduced through the skin, and scattered light is collected at a certain distance from the emitting source. The distance between the emitter and collector (or detector) determines the path through which the collected light travels. In order to reach the cerebral vasculature, the emitter-collector separation should be larger than 2.5cm in adults [67]. The detected signal is affected by the coupling of light into and out of the tissue. This coupling is affected by hair follicles, sweat and movement of the emitter or the collector. Changes in this coupling affect the signal's quality. In addition, as the light travels through extracerebral layers on its way in and out of cerebral layers, changes in blood flow and oxygen saturation within the extracerebral vasculature are picked up during collection and may contaminate the cerebral related hemodynamic response. Consequently, preprocessing methods should focus on reducing the effect of physiologic and extracerebral contamination on the collected signals. Such preprocessing methods should be robust enough, but also sensitive enough, such that cerebral hemodynamics are correctly identified and analyzed. Some of the mixed interferences are quasi-periodic, while others are completely random, thus increasing the complexity of the task. These temporal information sources are mixed together in the recorded signals. Since many of such sources are non-stationary, it is important to use suitable methods in order to receive reliable results.

The goal of our study is to develop robust methods for preprocessing fNIRS signals that can be automatically applied to any fNIRS data and provide a comprehensive approach for analysis. Identifying artifacts that result from coupling issues is an important task that should be performed early on in the processing pipeline to assure that those artifacts don't affect the received results and conclusions. The contamination of the Hemodynamic Response Function (HRF) by extra-cerebral sources is heavy and leads to Signal to Noise Ratio (SNR) of the HRF being negative. In addition to severe contamination of the information function, it is also a non-stationary process. Meaning that the filtration of the signals should be carefully designed taking those factors into account, since some solutions may create a severe distortion of the information function. Although this temporal mixture of many sources is quasi-periodic, due to strong contribution of cardiorespiratory source, the brain hemodynamics do not necessarily have any type of periodicity.

In most NIRS systems, light is coupled into and out of the tissue using optical fibers, lenses or light-guides [72]. These coupling elements are positioned in close contact to the skin, which has a different index of refraction. In addition, hair follicles, sweat or debris also affect the coupling efficiency. Most commercial NIRS systems analyze the detected light intensity, and the level of noise in order to determine coupling efficiency and identify Noisy Channels (NCs). It is clear that low light levels will result in a poor signal and low SNR. However, there are additional features of the signal that can indicate whether the coupling efficiency is adequate.

As red and near infrared light travels through the tissue, it is mainly absorbed by the hemoglobin chromophores (mainly oxygenated and de-oxygenated hemoglobin). Their concentration is modulated by the dilation and constriction of the arterial blood vessels during the cardiac cycle. This modulation is manifested by a clear peak in the power spectra of the detected light intensity (or in the calculated chromophore concentrations), at the cardiac rhythm. The modulation is missing in the case of poor coupling, as the light travels outside the tissue. Several groups have identified this modulation as a feature for determining coupling efficiency ([73], [74]). In addition to cardiac modulation of the signal, respiration and blood pressure modulation also affect the detected signals [75], we therefore collectively call these noise sources "cardio-respiratory" sources.

As the optical elements are in free contact with the skin, any relative movement between them results in an artifact. Such artifacts may exhibit a sharp change (spike). In addition, slow movements, due to drift or shifts in the coupling of the optical elements are also apparent. There are several approaches for identifying these events, some examine the individual channel and determine whether and when a motion artifact occurs ([76], [77]) while others look at the collective dynamics of all channels and analyze their statistics ([78], [79]). Different strategies, ranging from spline interpolation [76] to wavelets [79] have been recently described for reducing the effect of motion artifacts on the detected data.

The low frequency trend, or drift, in the recorded signals is observed in the majority of physical or natural processes. Such temporal processes are stochastic by nature, thus it is logical to use the field of probability and statistics when processing and analyzing these types of data. Therefore, the trend or drift can be regarded as a time-dependent first statistical moment. Whereas cases with a constant offset (instead of a changing trend) demonstrate time-independent first statistical moments. The definition of Wide Sense Stationarity (WSS) demands the first two statistical moments to be time independent. Hence, the signals with a drift are automatically labeled as non-stationary. That said, in many cases, the non-stationarity resides mainly in the first statistical moment, thus if removed, the signals may become stationary. Even though it is extremely hard, and in some cases not possible, to remove the time dependency of the second statistical moment, it is still highly recommended to remove the time-dependent first statistical moment. The resulted signals will still remain non-stationary, but the effect of the non-stationarity on the processing and analysis tools' performance will be significantly reduced.

In order to extract the hemodynamic changes that are related to neuronal activity from the detected signal, the contribution of systemic physiological sources, should be identified and reduced. Open-source tools for fNIRS analysis, like HOMER 2&3 [80] or SPM-fNIRS [81], use bandpass filtering to reduce the effect of the cardiac and respiratory dynamics. Recent, more sophisticated approaches include using short-separation channels (using a shorter distance than 2.5cm between the emitter and collector) that collect light from superficial layers that are not related to cerebral hemodynamics ([82], [83]). Alternatively, Principal Component Analysis (PCA)[84] or targeted PCA [85] and other filtering techniques including wavelets [85], have been proposed to remove the effect of physiological sources, in the absence of a short-separation signal.

There is currently no accepted gold standard for evaluating the efficiency and quality of different filtering techniques for removal of physiological sources or motion artifacts. Pinti et. al. [86] have recently reviewed common filtering techniques, and have compared their performance using artificial data combined with real NIRS data acquired during rest. The outcome of different filtering techniques was evaluated in the framework of a General Linear Model (GLM). Yet, it is still unclear which processing procedure is the optimal one. If we assume that the cardio-respiratory, physiologic, noise sources are quasi-periodic and stationary, then simple band-pass filtering can remove their contributions. However, simple band-pass filtering, and even more elaborate wavelet-based filtering of the NIRS signal, fail to remove all of the physiologic contributions. This is demonstrated in the high correlation between different NIRS channels during rest [68]. Empirical Mode Decomposition (EMD), is an empirical method for processing non-stationary signals [87]. It has been used extensively for filtering EEG signals and removing common noise sources [88]. We've applied this filtering method to NIRS signals and compared its output to that of wavelet filtering [89]. This technique has also been applied to NIRS signals in order to extract the cardiac component of the signal [90] and motion artifact correction [91]. EMD decomposes the signal into Intrinsic Mode Functions (IMFs), that are extracted using the formulation of Huang [87]. Each IMF contains a certain source that was mixed in the signal, therefore the decomposition allows for independent processing of signal's source components.

To address the challenges of fNIRS processing we developed methods for artifact detection and filtering of the signals. The NCs detection algorithm, called Maximal Variability Expectation (MVE), looks at the statistical distribution of a random parameter representing the behavior of variance within the signals, and compares it between the recorded signals. Our underlying assumption is that efficient coupling is demonstrated by a strong cardio-respiratory component in the signals. Consequently, noisy channels introduce an increased skewness of the Probability Mass Function (PMF) of the calculated random variable, similarly to the idea presented in [85], where wavelet coefficients were assessed using kurtosis. Therefore, noisy channels are identified as the ones that increase the skewness of the PMF above the predefined threshold. The motion artifact detection algorithm, called Cross Segment Validation (CSV), is aimed at identifying substantial motion artifacts, that result in a large variability between channels during a relatively short period of time. We start by identifying a minimal variability section to serve as a reference segment. The potential artifact segments are then compared to this reference based on two parameters extracted from the data of the individual subject. Periods with higher variability than a fixed threshold are identified as artifacts. The recorded fNIRS signals have quite significant drifts that hold no value regarding the information of the brain hemodynamic activity. Therefore, the detrending procedure is commonly done at the early stage of the processing to remove the time-dependent first statistical moment. The common methods of detrending include High-Pass Filter (HPF)[86] and Discrete Cosine Transform (DCT)[81]. The CCFA algorithm [30] was initially developed for high accuracy filtration and missing samples approximation. It was shown that this algorithm can reconstruct the missing information from the surrounding samples with an exceptionally high accuracy. Therefore, we decided to use CCFA algorithm [30] with some adaptations. CCFA is a non-stationary, non-linear method of data filtration. The idea of the algorithm is to reconstruct a filtered signal by sequentially assessing the curve of the data using curve fitting within a predefined moving window. Our proposed extracerebral and physiologic hemodynamic contribution filtration method employs EMD. Once the data is decomposed into the IMFs, we calculate their frequency ranges and remove IMFs with main power contributors lying outside of the desired frequency band. The proposed methods were tested based on ([79], [92], [93]). The above mentioned methods and their applications are explained in a work entitled: *"Artifact Detection in fNIRS Data and non-Stationary Preprocessing Methods"* by D.Patashov et.al. This research was partially funded by the BSMT consortium of the Israeli Innovation authority and began as a large collaboration of multiple industrial companies and research institutions. For comparison of fNIRS and fMRI was collected at Tel Aviv Sourasky Medical Center's: Laboratory for Brain and Emotion Experience Sagol Brain Institute, Wohl Institute for Advanced Imaging in Israel.

Summary

To summarize, in this work we address the challenges of information related to motoric and neurologic activity using the main assessment devices in that field (i.e. EEG, fNIRS, fMRI, Video, IMU). Gait Analysis section provides solutions for the assessment of human gait for orthopedic and neurologic assessment. Gait and the Brain section presents the way to assess the complicated relation between the gait and the neural activity, as well as how they affect each other. Brain Research section proposes methods that allow the assessment of the neural activity through the hemodynamics of the brain and the solutions for the detection of motor activity distorting the information source.

Methods

Sequential Desmoothing Extremum Tracking – SDET

Sequential Desmoothing Extremum Tracking or SDET for short, can be used as a general-purpose solution for peak detection in noisy, quasi-periodic, multidimensional signals. It can be applied to many types of sources, not necessarily temporal ones. Also, depending on the chosen procedure steps, it can be used for both stationary and non-stationary signals. SDET is a heuristic algorithm that can be adjusted to many types of tasks due to its flexibility. The adjustment is only needed once. The following filtrations of the same signal type can all be performed automatically.

SDET – General Heuristic Procedure:

1. Filter the signal using any smoothing procedure until the highest frequency of the filtered signal is the same as the pattern that is being assessed. Denote this filtered signal as $f_1(\bar{x})$.
2. Filter the signal using same smoothing procedure multiple times with decreasing smoothness of the resulted signal. The smoothest signal should be the one resulting from step "1" and the least smooth one should be the original signal. Denoted as $f_1(\bar{x}), \dots, f_k(\bar{x})$, where k is the number of filtration stages. The order of $f_1(\bar{x}), f_2(\bar{x}), \dots$ creates a sequential desmoothing, meaning that the higher the index the less smooth the signal is, up to $f_k(\bar{x})$ which is the original unfiltered signal.
3. Detect all the local extrema points on the $f_1(\bar{x})$, that is the smoothest signal. Denote the time stamps of these extrema points as $\bar{x}_1^{(1)}, \dots, \bar{x}_p^{(1)}$, where p is the number of extrema points and the upper index is the iteration number.

Begin the sequential procedure (set $m = 1$):

4. Use $\bar{x}_1^{(m)}, \dots, \bar{x}_p^{(m)}$ as starting points on $f_{1+m}(\bar{x})$. Adjust each of the points to match the peaks of $f_{1+m}(\bar{x})$, producing $\bar{x}_1^{(m+1)}, \dots, \bar{x}_p^{(m+1)}$. Gradient ascent can be used before adjustment to accommodate for the shape distortion created by the filtration.
5. Increment m by one and repeat step <4>. The procedure should be repeated until $m = k - 1$ (included) to receive the peaks on the original signal.

Using the proposed procedure, it is possible to detect peaks of different quasi-periodic components within the assessed process accurately as long as other peak contributors can be filtered out. By removing any other sources creating the undesired peaks, we are able to assess the number of the peaks that we are aiming to detect as well as a rough estimation of their locations. In cases where a lower frequency band creates additional peaks, it can be filtered out as well in step <1> and then slowly restored through the desmoothing procedure from step <2>. The logic in this case would be exactly the same, where the larger the m the closer the $f_m(\bar{x})$ to the original unfiltered signal. The number of timestamps in step <3> provides us with the number of peaks to be detected, while their temporal values provide an estimation of the peaks' locations. In step <4>, the estimated peaks indicate that the correct peak for that iteration is in the close by area. Therefore, the peaks should be adjusted to suit the current filtration stage of the signal. The adjustment should be made based on the desired type of the peak. For example, if the desired outcome is the highest position, then the adjustment should select the highest point near the current estimation. If the desired outcome is the accurate time stamp, then the most centered one could be selected and so on. The number of filtration stages can be selected as a number of possible sequential filtration stages. This approach will provide an automatic solution that will always work and will not require additional adjustments, but at the same time, it would produce a higher runtime for the procedure. To reduce the runtime, filtration stages should be defined based on the components that reappear within the less filtered stages. Usually, the optimal solution would be based on the number of different patterns that were initially filtered out. It is best to avoid reintroduction of more than one pattern type per stage. Thus reducing the number of stages to the number of interfering patterns or to double of that number to create an additional safety margin. It should be noted that selection of a filtration method may be important in some cases. For example, when dealing with a non-stationary process, it is important to use filtration procedure that does not assume stationarity.

Cumulative Curve Fitting Approximation – CCFA

Cumulative Curve Fitting Approximation, shortly called CCFA is a multipurpose, non-stationary, non-linear method of signal processing that serves as a general solution for many types of tasks (e.g. filtration, missing samples approximation, resampling, etc.). The approximated process does not have to be quasi-periodic or temporal source of information either. The general definition of the algorithm is designed to provide a solution for a large variety of tasks, while being very adjustable to the specific requirements of each task and allowing the usage of additional information that is available in some cases, to increase the accuracy of the calculations.

CCFA – General Purpose Algorithm:

Denote CCFA algorithm order as k and a random process (i.e. signal) before any adjustments as: $\begin{pmatrix} s_1 \\ \vdots \\ s_L \end{pmatrix}^{(0)}$ where L is the length of the signal. The upper index indicates the iteration count, meaning the number of times the signal was adjusted. The iterative cumulative approximation procedure is defined as follows:

$$\begin{pmatrix} s_{i+1} \\ \vdots \\ s_{i+k} \end{pmatrix}^{(i+1)} = \chi \cdot \begin{pmatrix} \beta_{i+1} \\ \vdots \\ \beta_{i+k} \end{pmatrix}^{(i)} \circ \begin{pmatrix} s_{i+1} \\ \vdots \\ s_{i+k} \end{pmatrix}^{(i)} + (1-\chi) \cdot \begin{pmatrix} \gamma_1 \\ \vdots \\ \gamma_k \end{pmatrix}^{(i)} \circ \begin{pmatrix} f_1 \\ \vdots \\ f_k \end{pmatrix}^{(i)}$$

Where° is Hadamard multiplication, $i = 0, \dots, L-k$ is the running index, $\begin{pmatrix} f_1 \\ \vdots \\ f_k \end{pmatrix}^{(i)}$ is the weighted curve fitting function for the approximated section, $\chi \in (0,1)$ defines the balance between the signal and the curve fitted function for the correction procedure and $\begin{pmatrix} \beta_1 \\ \vdots \\ \beta_L \end{pmatrix}^{(0)}$ are the reliability weights for samples $\begin{pmatrix} s_1 \\ \vdots \\ s_L \end{pmatrix}^{(0)}$ where $\forall j, \quad \beta_j \in [0,1]$ with $\beta_j = 0$ treated as a missing sample. The value of β_j represents how reliable the corresponding sample s_j is. Whenever such information is available, it should be provided to the algorithm to increase the accuracy of the approximation process, otherwise, the values of β_j should be set to 1. The counterweights γ_τ are derived from the reliability weights and the balancing parameter:

$$\gamma_\tau^{(i)} = \frac{1 - \chi \cdot \beta_{i+\tau}^{(i)}}{1-\chi}$$

Where $\tau = 1,2,\dots,k$ is index within the sliding window. Counterweights' purpose is to assure the convergence of the iterative correction procedure by restoring the balance of the equation that is affected by the reliability weights. Next, the unreliable samples indicating function, δ_j is defined to provide the correct adjustment procedure to each sample within the signal:

$$\forall j, \quad \delta_j = \begin{cases} \lambda & \lambda \in \{0,1\} \\ \dfrac{1 - sign\left(\beta_j^{(0)} - \theta\right)}{2} & otherwise \end{cases}$$

$$sign(q) = \begin{cases} -1 & q \leq 0 \\ 1 & q > 0 \end{cases}$$

Where $\theta \in [0,1)$ being the reliability threshold. Any values of $\beta_j^{(0)}$ that are equal or lower than θ indicate the samples that would be approximated using closed loop procedure while others are approximated using open loop procedure, when semi-open loop procedure is performed. Parameter $\lambda \in \{0, 0.5, 1\}$ defines open, semi-open or closed loop procedure, respectively. When performing an open loop procedure, all the approximations are calculated using the original samples that were not tempered with in any way. In closed loop procedure, for each iteration, the used samples are those that resulted from the correction performed by the previous iteration. The semi-open loop procedure is the combination of the two, where some samples of the signal would be approximated using closed loop procedure, while others are approximated by the open loop procedure. The purpose of the semi-open loop procedure is mainly for cases with unreliable sample regions. For example, if there are large sections of missing samples within the processed signal, open loop procedure cannot be performed using a small order. For the procedure to work, order of the algorithm must be larger than the largest missing samples section. This is because CCFA is a window-based method, thus when the window that is defined by the order of the algorithm would be in a section of missing samples, there might not be enough existing samples for the curve fitting approximation if the selected window is too small. This issue does not exist when using the closed loop approximation since the procedure itself approximates these samples and then uses these approximations for the following steps. Semi-open loop procedure provides the solution for cases where the open loop procedure is needed to be performed with a window size that is small relative to the missing samples gap sizes. This is solved by performing an open loop procedure on all the reliable samples and closed loop procedure on the missing ones. Meaning that throughout the iterations, reliable samples are used for the approximation without any adjustments, while the unreliable ones being estimated in each iteration anew and then used for the approximation in that area in the following iterations. Correction of the reliability weights is performed as follows:

$$\beta_{i+\tau}^{(i+1)} = 1 - \varepsilon_\tau^{\delta_{i+\tau}} \cdot \left(1 - \beta_{i+\tau}^{(i)}\right) = \left(1 - \varepsilon_\tau^{\delta_{i+\tau}}\right) + \varepsilon_\tau^{\delta_{i+\tau}} \cdot \beta_{i+\tau}^{(i)}$$

$$1 - \lceil\lambda\rceil = \varepsilon_1 \leq \dots \leq \varepsilon_k = 1$$

Where $0^0 = 1$, ε_τ is the inaccuracy suppression rate function. Through the procedure, the samples of the signal are corrected with each iteration. Therefore, the reliability of these samples also improves throughout the procedure. To take this into account, reliability weights β_j are also corrected after each iteration. Meaning that with every correction of the signal's sample s_j, corresponding reliability weight's value is approaching the value of 1. The rate at which β_j will approach the value of 1 is defined by the ε_τ function. For example, evenly spaced ε_τ values would result in a constant increment rate of β_j, whereas logarithmically spaced ones would produce an increasing increment rate. The weighted curve fitting function $\begin{pmatrix} f_1 \\ \vdots \\ f_k \end{pmatrix}^{(i)}$ should be selected based on the properties of the approximated signal. It is defined by the operator $WCF\{\cdot,\cdot\}$ as a general operator for any type of weighted curve fitting function:

$$\begin{pmatrix} f_1 \\ \vdots \\ f_k \end{pmatrix}^{(i)} = WCF\left\{ \begin{pmatrix} \check{s}_{i+1} \\ \vdots \\ \check{s}_{i+k} \end{pmatrix}^{(i)}, \begin{pmatrix} w_1 \\ \vdots \\ w_k \end{pmatrix}^{(i)} \right\}$$

$$\begin{pmatrix} \check{s}_{i+1} \\ \vdots \\ \check{s}_{i+k} \end{pmatrix}^{(i)} = \begin{pmatrix} 1-\delta_{i+1} \\ \vdots \\ 1-\delta_{i+k} \end{pmatrix} \circ \begin{pmatrix} s_{i+1} \\ \vdots \\ s_{i+k} \end{pmatrix}^{(0)} + \begin{pmatrix} \delta_{i+1} \\ \vdots \\ \delta_{i+k} \end{pmatrix} \circ \begin{pmatrix} s_{i+1} \\ \vdots \\ s_{i+k} \end{pmatrix}^{(i)}$$

The approximation, $WCF\{\cdot,\cdot\}$ is calculated using weights $\begin{pmatrix} w_1 \\ \vdots \\ w_k \end{pmatrix}^{(i)}$ provided by:

$$\begin{pmatrix} w_1 \\ \vdots \\ w_k \end{pmatrix}^{(i)} = \begin{pmatrix} \alpha_1 \\ \vdots \\ \alpha_k \end{pmatrix} \circ \begin{pmatrix} \beta_{i+1} \\ \vdots \\ \beta_{i+k} \end{pmatrix}^{(i)}$$

With $\begin{pmatrix} \alpha_1 \\ \vdots \\ \alpha_k \end{pmatrix}$ being the distribution function for weighted curve fitting, where $\forall j, \quad \alpha_j \in [0,1]$. Note that it is assumed that $WCF\{\cdot,\cdot\}$ operator is either insensitive to the sum of the $\begin{pmatrix} w_1 \\ \vdots \\ w_k \end{pmatrix}^{(i)}$ values or that it performs normalization of the sum to 1 internally. The complete approximation procedure can be described by:

$$\tilde{s}_n = \chi^k \cdot s_n^{(0)} \cdot \prod_{j=0}^{k-1} \beta_n^{(n-j-1)} + (1-\chi) \cdot \sum_{m=0}^{k-1} \chi^m \cdot \gamma_{m+1}^{(n-m-1)} \cdot f_{m+1}^{(n-m-1)} \cdot \left[\prod_{j=0}^{m-1} \beta_n^{(n-j-1)} \right]^{\Delta(m)}$$

$$k \le n \le L-k \quad \Delta(q) = \begin{cases} 0 & q = 0 \\ 1 & otherwise \end{cases}$$

It is clear that parameter χ affects this procedure by influencing the curve fitting through the iterative procedure. In the final equation, it becomes a predefined recombination distribution in addition to the mentioned effect that resides inside parameters β, γ and f. Since there is no reason to limit the recombination distribution, the predefined χ multipliers were redefined to general recombination weights ω_j as follows:

$$\chi^k \to \omega_0 \quad , \quad (1-\chi) \cdot \chi^m \to \omega_{k-m}$$

Where $\omega_j \in [0,1]$ for $j = 1,2,\dots,k$, are the recombination distribution weights and $\omega_0 \in \mathbb{R}_0^+$ is the source function recombination weight. Due to this substitution, normalization of the equation is required to assure convergence to the desired curvature. Therefore, the final approximation equation is defined by:

$$\tilde{s}_n = \frac{\omega_0 \cdot s_n^{(0)} \cdot \prod_{j=0}^{k-1} \tilde{\beta}_n^{(n-j-1)} + \sum_{m=0}^{k-1} \omega_{k-m} \cdot \gamma_{m+1}^{(n-m-1)} \cdot f_{m+1}^{(n-m-1)} \cdot \left[\prod_{j=0}^{m-1} \tilde{\beta}_n^{(n-j-1)}\right]^{\Delta(m)}}{\omega_0 \cdot \prod_{j=0}^{k-1} \tilde{\beta}_n^{(n-j-1)} + \sum_{m=0}^{k-1} \omega_{k-m} \cdot \gamma_{m+1}^{(n-m-1)} \cdot \left[\prod_{j=0}^{m-1} \tilde{\beta}_n^{(n-j-1)}\right]^{\Delta(m)}}$$

$$k \leq n \leq L - k \quad \Delta(q) = \begin{cases} 0 & q = 0 \\ 1 & otherwise \end{cases}$$

Where $\tilde{\beta}_\tau^{(i)}$ are the normalized weights explained below. The equation above defines the approximation for a specific sample n within the processed signal. Since it is iterative moving window-based procedure, the number of the iteration can be substituted with the index of the sample. Thus allowing for the explicit form of the equation to be extracted. Every variable in the final formula is received through the iterative procedure defined above and then used in this equation to receive the filtered signal. Signal's samples are unchanged until they are within the moving window range, meaning that:

$$s_n^{(n-k)} = s_n^{(0)}, \quad \beta_n^{(n-k)} = \beta_n^{(0)}$$

The normalization of the weights is required for two reasons; First is to reduce the effects of the window size on the error estimations. Second is to avoid computational issue when calculating a large number of fraction multiplications.

$$\tilde{\beta}_\tau^{(i)} = \left(\beta_\tau^{(i)}\right)^\eta$$

$$\eta = \begin{cases} \dfrac{1}{\left(1 - \min\limits_j\{\beta_j\}\right) \cdot (k-1) + 1} & \left(\min\limits_j\{\beta_j\}\right)^k \leq \ell \\ 1 & otherwise \end{cases}$$

With ℓ being the calculation accuracy for β_j corrections. Notice that when the calculating machine's accuracy is sufficient, β_j weights are unchanged. This is because in cases where the accumulating error is much smaller than the calculation values, the result should be accurate without any additional steps. On the other hand, if the accumulating error is sufficiently large, the resulted approximation may be quite far off unless the calculation procedure is normalized in such a way that the approximated fractions are significantly larger than the accumulating error. The explicit formula for $\tilde{\beta}_n$ is:

$$\tilde{\beta}_n^{(n-m)} = 1 - \left(1 - \tilde{\beta}_n^{(0)}\right) \cdot \prod_{j=m+1}^{k} \varepsilon_j^{\delta_n} = \left(1 - \prod_{j=m+1}^{k} \varepsilon_j^{\delta_n}\right) + \tilde{\beta}_n^{(0)} \cdot \prod_{j=m+1}^{k} \varepsilon_j^{\delta_n} \quad 0 \leq m < k$$

It is also important to note that in most cases the signal should not have any missing samples and the reliability of each sample is also, often unknown. Therefore, the equation for the filtration of these common cases can be significantly simplified:

$$\tilde{s}_n = \frac{\omega_0 \cdot s_n^{(0)} + \sum_{m=0}^{k-1} \omega_{k-m} \cdot f_{m+1}^{(n-m-1)}}{\sum_{m=0}^{k} \omega_{k-m}} \quad k \leq n \leq L - k$$

In addition, default values can be used for many of the defined parameters. Our suggested default input parameters are: $\chi = \frac{1}{2}$, $\theta = 0$, evenly distributed ε_j, evenly distributed α_j and evenly distributed ω_j where $j = 1,2,\dots,k$. The correction accuracy is suggested to be: $\ell = 10^{-12}$. For weighted curve fitting approximation, we suggest using weighted polynomial curve fitting due to its flexibility. Recombination weight for the source function is suggested to be:

$$\omega_0 = \begin{cases} 0 & \lambda = 0 \\ \min\limits_{j}\{\omega_j\} & otherwise \end{cases}$$

In cases where the signal has no noise or inaccurate samples, when performing missing samples approximation, the source function recombination weight should be $\omega_0 \geq 1$ to reduce the distortion of the reliable samples. Proposed default parameters should provide relatively high accuracy results for most cases, while significantly simplifying the algorithm. Under the proposed settings, the remaining required parameters are: algorithm order k, procedure type λ and degree of the polynomial for the weighted curve fitting approximation p_{ord}. It should be noted that semi-open and closed loop approximations are asymmetrical, meaning that they will produce different results when perform in different directions on the signal. Similar phenomena may occur if asymmetric distribution is selected for ω_j or α_j. Therefore, in such cases using the algorithm twice - once in each direction (if applicable) and averaging the results may increase the accuracy.

CCFA can perform filtration and missing samples approximation routines simultaneously and independently. The ability to approximate missing samples also provides an additional use for this algorithm, which is the resampling of the processed signal. By adding missing samples in the locations of the desired samples, CCFA is able to approximate them and thus produce the resampled signal.

Gait Analysis

Gait: Experimental Setup

154 subjects (age: 70±12) with high incident rate of falls, participated in a six-week long training program on a V-Time system [15]. Data were acquired at five clinical centers across five countries (Belgium, Israel, Italy, Netherlands, and the UK). The study had full ethical approval from local human studies' committees. The subjects were informed about the experimental task to be undertaken prior to the experiment. The detailed description of the experiment is explained in [16].

V-Time program participants underwent a series of training sessions. In each session, the system continuously monitored the position of the subject's feet and the reference point for each trial was set as a mean of the feet coordinates. The recorded video was pre-processed by the V-TIME and provided data describing feet location in space as time series (temporal information). The system also stored training-related parameters, such as obstacle locations and their properties, e.g. height and length. Taking the system axes and gait cycle into consideration, the Toe Off (TO) and Heel Strike (HS) points along the Z-axis are in correlation with local maxima and minima, respectively, as shown in Figure 1.

Figure 1. V-Time system. VR augmented treadmill with Kinect and HD cameras upfront for gait detection and tracking while navigating in a virtual environment. Axes orientation is as shown.

Gait: SDET Peak Detection

Let us examine a quasi-periodic, noisy, temporal signal [Figure 2] collected during gait performance on the V-Time system. It can be clearly seen that the noise appearing in these signals are reducing the amplitude near the local maxima locations. In this dataset, there was little to no noise interfering with local minima points. System errors produces flat parts just as can be seen in the example. Both types of distortions were mainly near local maxima locations due to system setup limitations.

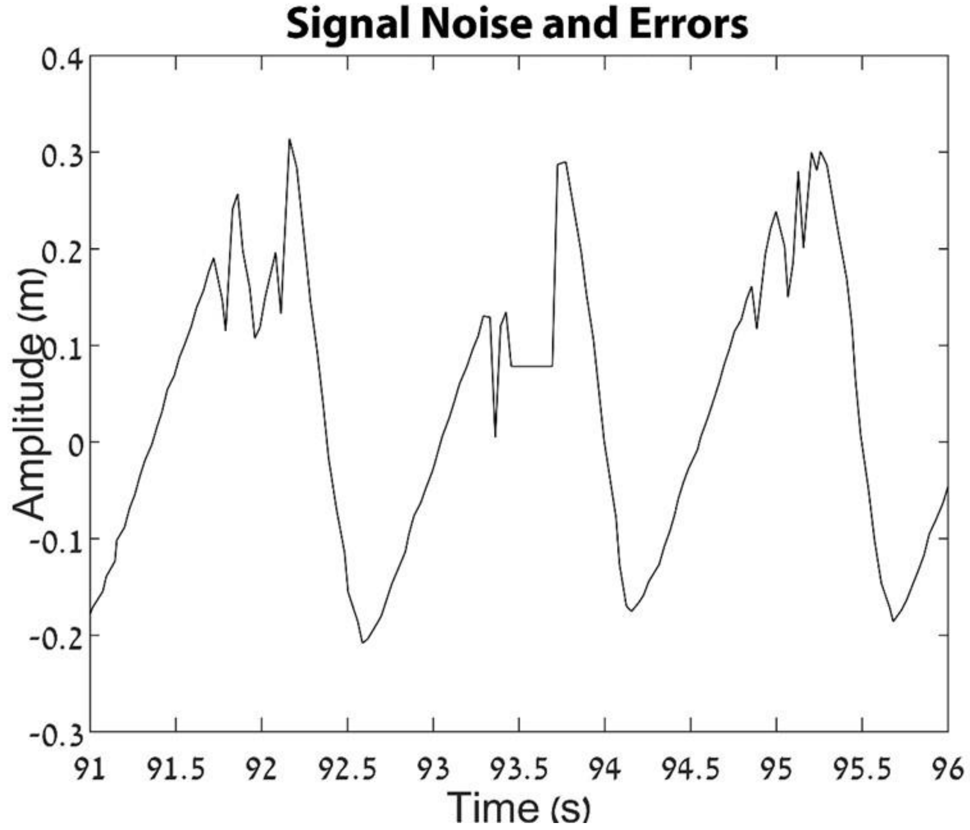

Figure 2. V-Time recorded signal. The upper part of the waveform has a strong noise affecting the pattern. The period within 93-94 seconds has a flat section beginning at 93.5 seconds resulting from a short duration system failure (i.e. missing samples). The amplitude shows the change in feet location along the treadmill length.

In order to reduce the effects of noise and errors on local extremum estimation, an optimization method for detection of a global extremum (or getting as close to it as possible) in each period of quasi-periodic functions was developed and used in a simplified form on our signals. The idea behind SDET algorithm was to create a sequence of filtered signals and track the changes of extrema points from the smoothest signal back to the original. First let us define all the parameters which will be used in this heuristic algorithm:

1. Let $f(\bar{x})$ be a quasi-periodic n-dimensional noisy signal.
2. Multi-dimensional ellipsoid body is defined as follows:

$$E = \left\{ \bar{x} = \begin{pmatrix} x_1 \\ \vdots \\ x_n \end{pmatrix}, \left(\frac{x_1}{a_1}\right)^2 + \cdots + \left(\frac{x_n}{a_n}\right)^2 \leq 1 \right\}$$

   where $a_1, \cdots, a_n \in \mathbb{R}_+$ which denotes the semi-major axes.

3. Denote by $\bar{c} = \begin{pmatrix} a_1 \\ \vdots \\ a_n \end{pmatrix}$ the vector of semi-major axes of E.
4. Define the sequence of concentric n-dimensional ellipsoid bodies: $E_1, \cdots, E_k$ with corresponding vectors $\bar{c}_1, \cdots, \bar{c}_k$ such that $(\bar{c}_{m+1} - \bar{c}_m) \in \mathbb{R}_+^n$ where $m = 1,2, \dots, k-1$.

5. The standard n-dimensional Fourier transform is:

$$\Im\{f(\bar{x})\} = \frac{1}{(2\pi)^{n/2}} \int_{\mathbb{R}^n} f(\bar{x}) e^{-i\bar{x}\bar{\omega}}\, d\bar{x} = F(\bar{\omega})$$

6. Define $f_m(\bar{x}) = \Im^{-1}\{F(\bar{\omega}) \cdot \mathbf{1}_{E_m}\}, \quad 1 \le m \le k$, where $\mathbf{1}_{E_m}$ denotes the indicator function of E_m.

Heuristic Algorithm – Low Pass Filtering based SDET:

1. Set $\bar{c}_1$ such that it filters the maximum range of frequencies under the constraint that the number of signal cycles after filtering does not change.
2. Choose $\bar{c}_2, \bar{c}_3, \dots, \bar{c}_{k-1}, \bar{c}_k$, where E_k contains the whole bandwidth of the signal without the high frequency noise.
3. Calculate $f_1(\bar{x}), \dots, f_{k-1}(\bar{x})$.
4. Find all the local maxima on $f_1(\bar{x})$.
5. Apply a Gradient Ascent method on the received local maxima's $\bar{x}$ values (from 4) using the values as a start location on $f_2(\bar{x})$ to calculate new local maxima positions related to $f_2(\bar{x})$.
6. Select n-dimensional parallelepiped taking into consideration $\frac{\|\bar{c}_m\|}{\|\bar{c}_{m+1}\|}$ and periods of the $f_1(\bar{x})$.
7. Adjust the center of the above-mentioned parallelepiped at the local maxima (from 5) and choose the largest value point of $f_2(\bar{x})$ within the parallelepiped as authentic local maxima for $f_2(\bar{x})$.
8. Repeat the procedure from (5), increasing the signal indices by one, i.e., instead of $f_1(\bar{x})$ use $f_{1+m}(\bar{x})$ and instead of $f_2(\bar{x})$ use $f_{2+m}(\bar{x})$, where m is the iteration number until exhausting all iterations such that $f_{2+m}(\bar{x}) = f_k(\bar{x})$ [Figure 3].

The above procedure provides a solution for Low Pass Filter (LPF) based highest point detection within each cycle of a quasi-periodic, noisy, multidimensional signal. This procedure, when referring to the general SDET definition, uses a LPF for smoothing steps. Point adjustment here is done after performing gradient ascent. The adjustment itself is defined to select a highest point within a precalculated time window. It is important to note that gait signals in this study were close to being WSS processes, thus allowing us to discard the effects of the present non-stationarity and use LPF for the smoothing steps. Secondly, in this particular task, the time stamp of the detected peak was not important for further processing. Hence, the highest point was selected when detecting the local extrema. The noise in this case, are non-Gaussian and asymmetric. More accurately, the noise always reduced the amplitude wherever they appeared and never the opposite (due to system limitations). Therefore, selecting the highest position would provide the closest value to the true amplitude of the peak.

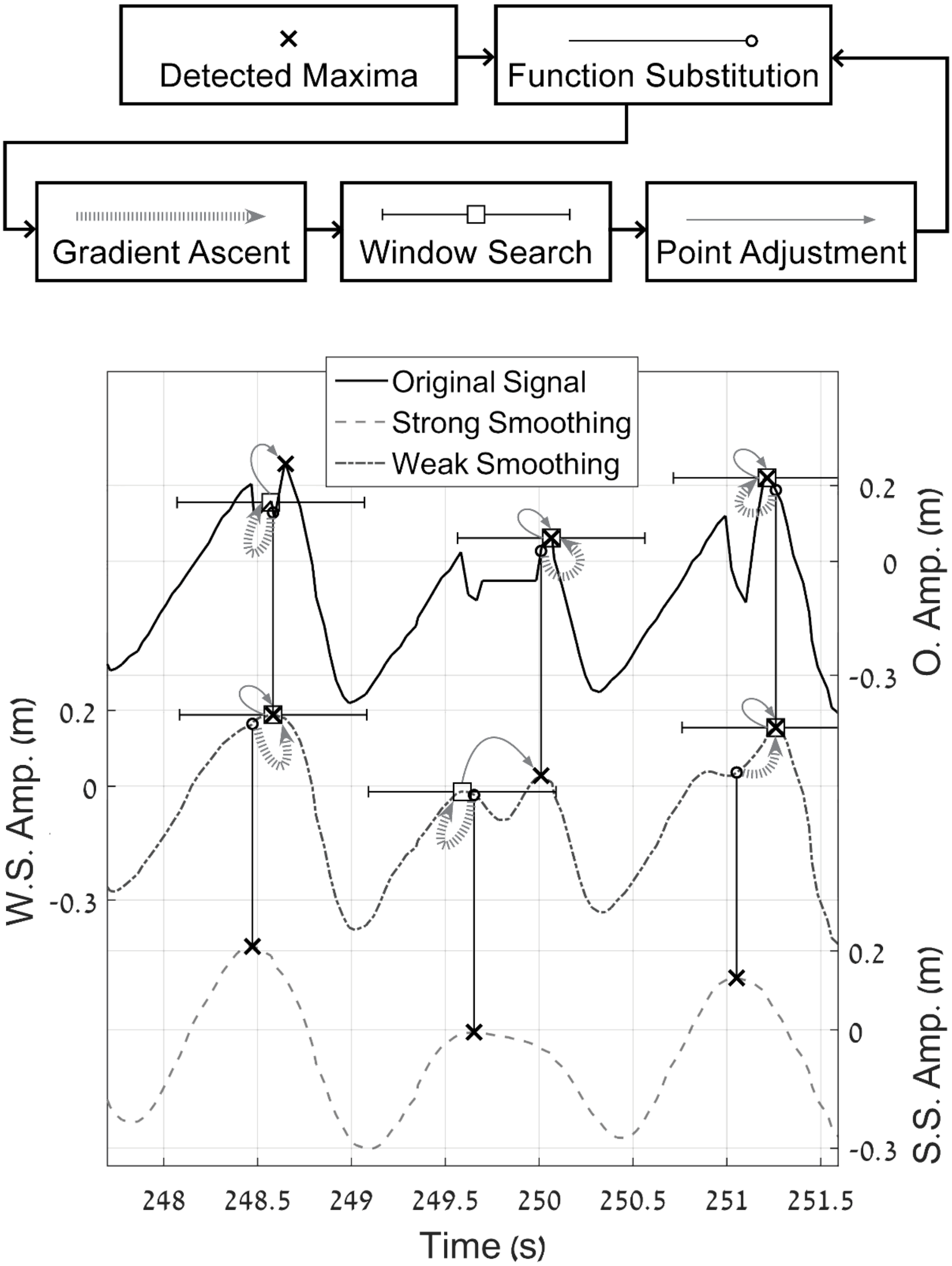

Figure 3. SDET flowchart and graphical illustration of two iterations (3-stage procedure) on the gait signal.

The above example shows the use of the algorithm on one dimensional signal. It should be noted that depending on the task, the logic of point adjustment step should be altered (e.g. instead of choosing the highest point within the given window, choosing a peak that is located on a section with more energy). Type of smoothing filtration should also be selected depending on a type of the signal.

In this study, the above explained procedure was used on one dimensional signal recorded along the Z-axis [Figure 2]. The optimal value of k was determined to be 3. Taking into consideration the period time and its variance among different subjects, the conclusion was that three is the minimum number of steps needed to locate all of the local extremum, which at the same time are global within their period. For three steps case, two filtered signals had to be calculated, therefore, two Low Pass Filters (LPF) were used independently: one that removed noise from Z-axis signal and one that removed both noise and system errors [Figure 3], thus receiving three signals (unfiltered signal, filtered signal containing errors and filtered signal without noise or errors). The first step was to determine the cutoff frequencies for the LPFs. After thoroughly analyzing the spectral patterns of our signals, it was found that the layout of the spectral power is almost identical for all the subjects. In order to extract this layout pattern, a Moving Average Filter (MAF) with a symmetric padding and window size of 20 samples (empiric size suited for 25-30 Hz sampling system) was applied, followed by the LPF (0.05 Hz), which preserved only the pattern line. On the resultant pattern line, if we define the maxima point located at 0Hz as maxima number zero and the following minima as minima number one, then the cutoff frequencies are at the second and third minima points [Figure 4].

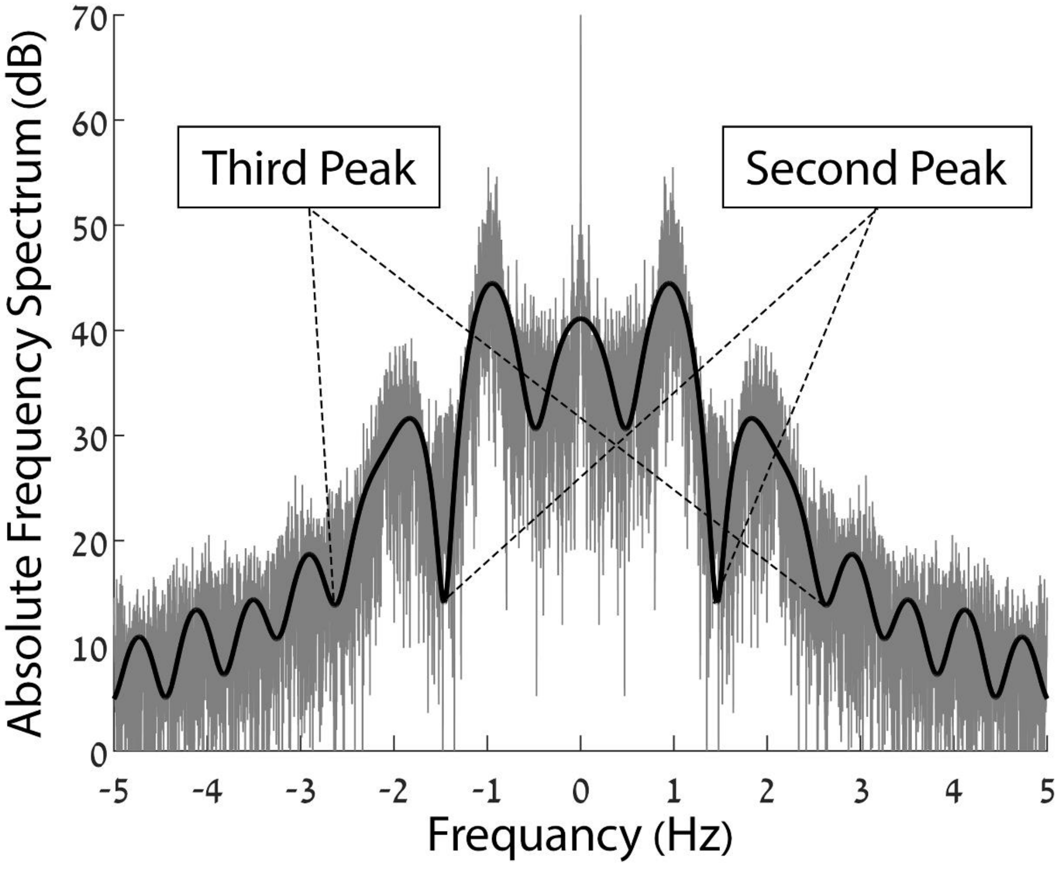

Figure 4. Trial absolute frequency spectrum in dB. The black line represents the pattern of the absolute frequency spectrum. The cutoff frequencies for LPFs are the second and third minima peak locations.

c_1 and c_2 were set as mentioned in the first step, providing the $\frac{\|\bar{c}_m\|}{\|\bar{c}_{m+1}\|}$ ratio suitable for the signal (in cases where determining all of c_k is unpractical, determine c_1 and use minimal step size allowed by the sampling rate). A window (parallelepiped in a 1D time series) was defined by a half window size equal to absolute value of time shift caused by the LPF. Window size was re-calculated in each iteration separately. The half window size must be smaller than the signal's shortest period.

Gait: Detection of Gait Abnormalities

Gait abnormalities can be assessed through the irregularities in the walking pattern and the obstacle avoidance performance. The location and parameters of the obstacles in the virtual course are known, thus the segmentation method can be targeted towards the areas of the obstacle occurrences, followed by detection of irregular steps to assess the gait avoidance strategy.

Signal segmentation

To assess walking performance related to obstacle negotiation, each signal was divided into segments with walking instability periods due to obstacle avoidance, i.e. comprising segments in which walking pattern changed due to proximity to obstacle avoidance task. First, the complex envelopes of the Z-axis signal were calculated for each foot. Linear interpolation was applied on each pair of consecutive extremum points (calculated using SDET) for envelope estimation. Next, the top mean envelope was defined as the mean of left and right foot signals' top envelopes. The bottom mean envelope was calculated in a similar manner and the total mean envelope was computed as an average of the two mentioned mean envelopes. The exponent was then applied for fluctuations hyperbolizing followed by subtraction of minimum from each of the resulted functions. The same procedure was done to the envelope means reflected across time-axis yielding six new auxiliary functions as a result. On these functions, any value below a threshold of 10% (empiric value) was detected. The segment was then defined to be part of the signal matching the time interval between two points closest to the obstacle (one on each side) and lower than the set threshold. For the m^{th} obstacle, denote I_k^m as time segment of k^{th} auxiliary function, where $k = 1,2,\dots,6$ and $m = 1,2,\dots,M$ with M being the total number of obstacles. Finally, the obstacle negotiation segment was defined as follows: $I^m = \bigcup_{k=1}^{6} I_k^m$ [Figure 5].

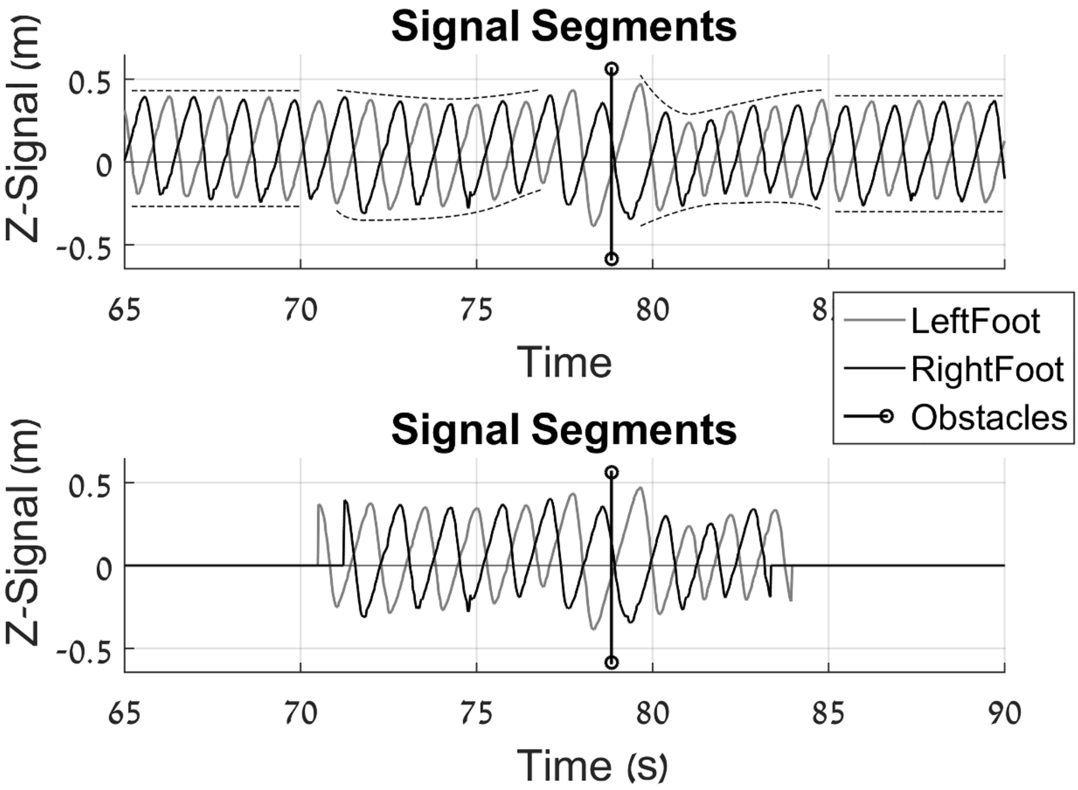

Figure 5. Signal segmentation. The bottom graph presents the segment related to obstacle avoidance, detected by the proposed approach. The upper graph shows the signal region containing the detected segment. Dashed lines provide a visual explanation for the detection.

Kernel based clustering

In order to statistically group steps or strides into different categories, Kernel based clustering was used. Let $\bar{f} \in \mathbb{R}^d$ be a feature vector of a single step. Assuming that we have n steps to classify, define $F = \{\bar{f}_1 \quad , \cdots , \quad \bar{f}_n\}$ and a kernel function $K_F : \mathbb{R}^d \to \mathbb{R}$ as:

$$K_F(\bar{f}) = \frac{1}{m} \left\| \begin{pmatrix} \|\bar{f}_1 - \bar{f}\|_2 \\ \vdots \\ \|\bar{f}_n - \bar{f}\|_2 \end{pmatrix} \right\|_1$$

Where $m = \max_{i,j} \|\bar{f}_i - \bar{f}_j\|_2 \;, \; 1 \le i,j \le n$. Denote $\bar{w} = \begin{pmatrix} K_F(\bar{f}_1) \\ \vdots \\ K_F(\bar{f}_n) \end{pmatrix}$. $\bar{w}$ can be regarded as one-dimensional signal. Thus, median filter can be applied to reduce its noise. Median filter order may vary depending on the feature vector parameters. Division into groups may be set in accordance with desired result classes. In this study, median filter with a half window size of 25 (empirical value) was applied, followed by division of the steps into two groups: regular and abnormal ones using a threshold calculated as follows:

$$\tau = mean(\bar{w}) + \frac{1}{2}\left(\max \bar{w} - \min \bar{w}\right)$$

Regular steps correspond to entries of $\bar{w}$ below the threshold. Our feature vector consisted of step length, step duration, distance from TO to HS and their differences between successive steps.

Gait: CCFA – Missing Samples Approximation

Assuming that the location of missing data region is known a priori, let us denote $[t_1, t_2]$ as a time period indexes of missing data. The missing data points between t_1 and t_2 were filled with values received from linear interpolation. CCFA algorithm requires input of algorithm order k_{ord}, procedure type λ and polynomial degree p_{ord} (in case of polynomial curve fitting). In this case, default settings were used for all relevant parameters. Reliability weights were neutralized $\forall j, \quad \beta_j = 1$ due to substitution of the missing samples section with interpolation values. Closed loop ($\lambda = 1$) procedure was used for the approximation. The ω_j weights were set to $\omega_{k-m} = (1-\chi) \cdot \chi^m$, $\omega_0 = \chi^k$. When using a default value for the balancing factor ($\chi = \frac{1}{2}$), the resulting recombination distribution is exponential. This type of distribution provides better ability of extending the approximation beyond the samples' range. Therefore, is more suitable to correct the missing samples that occurred in our data since they were always located near the local maxima locations (due to system limitations). Assuming that the correct input parameters (k_{ord} and p_{ord}) were provided, the procedure is provided by the following equation:

$$\tilde{s}_n = \left(\frac{1}{2}\right)^{k_{ord}} \cdot s_n^{(0)} + \sum_{m=0}^{k_{ord}-1} \left(\frac{1}{2}\right)^{m+1} \cdot f_{m+1}^{(n-m-1)}$$

The correction was performed only for the samples in the section $[t_1, t_2]$. Exponential distribution of the recombination weights is asymmetric, meaning that the results will be different if CCFA is performed in different directions along the signal. Therefore, the algorithm was used twice on each signal (once in each direction independently). The corrected section was defined as the average of the two results. In [30], this same procedure was defined differently. That is because at the time, the general form as presented in this work was yet to be developed. Nonetheless, the result and the calculations are the same since only difference are in the way that the procedure is presented and not in the procedure itself.

Gait: CCFA – Input Parameters Forecasting for Missing Samples Approximation

CCFA is very accurate algorithm if provided with correct parameters, but forecasting these parameters is a different task. We propose a Machine Learning (ML) algorithm that can forecast the required input parameters for CCFA. To evaluate this algorithm, we collected the recorded signals from subjects that had no missing samples occurrences, then chunks of information were removed to emulate missing data occurrences. These artificial data were designed to mimic the missing samples events observed in the recorded signals of the gait assessment trials. The created data contained almost 850,000 examples, which were randomly split into training and test sets, 80% and 20% of the data, respectively.

Let us define Training Data as: $TD \subset \mathbb{R}^l$. Each data sample $\bar{s} \in TD$ was normalized to unit vector $\hat{s}$. Assume that in TD the optimal parameters needed for CCFA to correct each sample signal are known. In our study, parameter range was limited to: $1 < k_{ord} \leq 50 \;\; and \;\; 1 \leq p_{ord} \leq 5$ in order to calculate the "best" input parameters for given examples (brute force approach). Since there are two parameters for each signal to be predicted, this was a Multi-Class Dual-Labeling, meaning that for each feature vector there was a 2D label vector with multiple classes for each component. Next, the Probability Mass Function (PMF) was approximated using statistical approach. PMF provides us with the probability of encountering each and every possible pair of parameters representing algorithm order denoted as k and polynomial degree denoted as p: $\wp(k, p)$. Using Bayes' theorem, probability vector of k if provided with p, was calculated. Bayes' theorem:

$$\wp(k|p) = \frac{\wp(p|k) \cdot \wp(k)}{\wp(p)} = \frac{\wp(k,p)}{\wp(p)}$$

Probability vector:

$$\wp(\bar{k}|p) = \begin{pmatrix} \wp(k_1|p) \\ \wp(k_2|p) \\ \vdots \\ \wp(k_m|p) \end{pmatrix}$$

Principal Component Analysis (PCA) was used to project the data into subspace with considerably smaller dimension: $D \subset \mathbb{R}^d$ where: $d \ll l$. The sum of d largest singular values made up 95% of the total sum of all the singular values from TD. Next, Random Forest Classifier (RFC) was applied on D to train the model. The process was done twice - independently for parameter k and for parameter p. After the model was trained as explained above, the parameters k and p could be calculated for a new signal containing missing data [Figure 6].

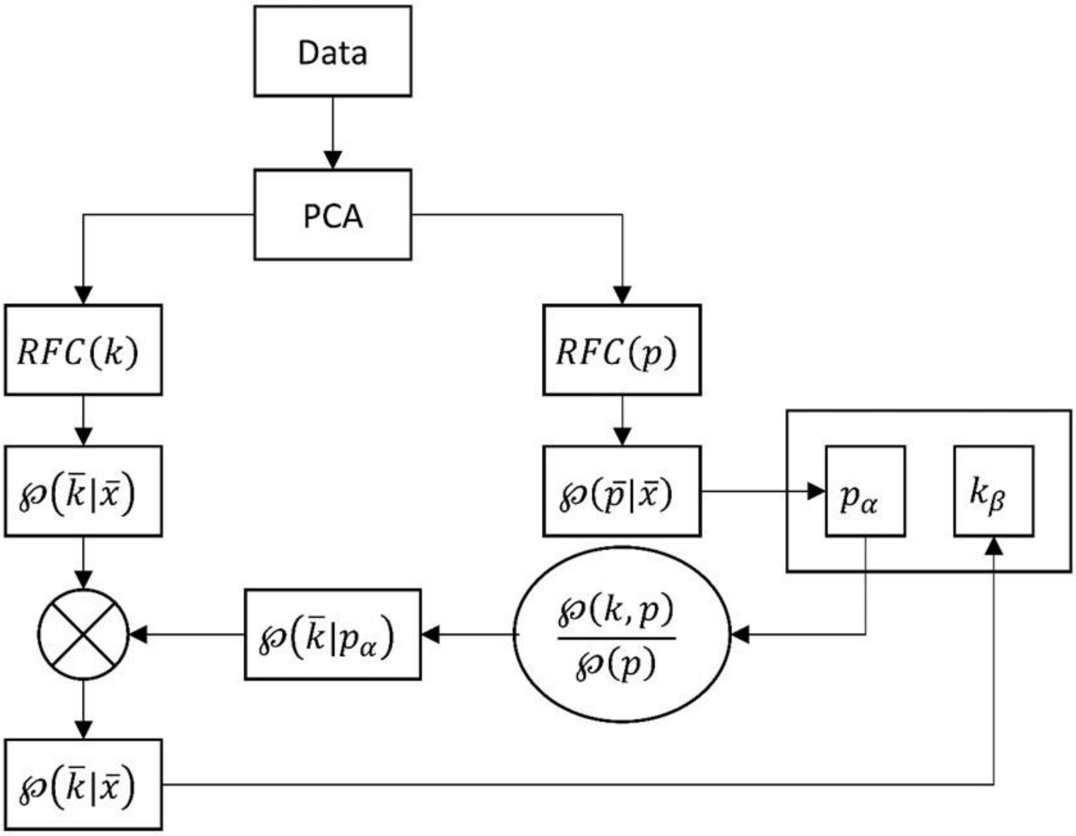

Figure 6. Machine Learning algorithm flowchart. The flowchart describes the classification steps for both parameters (labels). PMF, PCA and RFCs were already calculated and trained.

For a new signal denoted by $\bar{x} \in \mathbb{R}^l$ with unknown parameters k and p, forecasting was done as follows: normalize the signal to a unit vector $\hat{x}$ and use PCA to project the data into same subspace as D: $\tilde{x} \in \mathbb{R}^d$. Next, use trained RFCs to calculate the probabilities for each k and p:

$$\wp(\bar{k}|\bar{x}) = \begin{pmatrix} \wp(k_1|\bar{x}) \\ \wp(k_2|\bar{x}) \\ \vdots \\ \wp(k_m|\bar{x}) \end{pmatrix}, \quad \wp(\bar{p}|\bar{x}) = \begin{pmatrix} \wp(p_1|\bar{x}) \\ \wp(p_2|\bar{x}) \\ \vdots \\ \wp(p_n|\bar{x}) \end{pmatrix}$$

Then, define:

$$\wp(p_\alpha|\bar{x}) = \max_i\{\wp(p_i|\bar{x})\}$$

Since parameter p has only five possible values, RFC forecasts it with fairly high accuracy, as opposed to parameter k. Parameter k was adjusted using the probability of k given p for which p_α calculated from RFC was used:

$$\wp_r(\bar{k}|\bar{x}) = \frac{\wp(\bar{k}|\bar{x}) \circ \wp(\bar{k}|p_\alpha)}{\wp(\bar{k}|\bar{x})^T \cdot \wp(\bar{k}|p_\alpha)}$$

where ∘ is Hadamard product of two vectors. Similarly to the calculation of p_α, k_β was calculated using the adjusted probability:

$$\wp_r\left(k_\beta|\bar{x}\right) = \max_i\{\wp_r(k_i|\bar{x})\}$$

The forecasted parameters for CCFA algorithm to correct signal $\bar{x}$ were $\left(p_\alpha, k_\beta\right)$. Using parameters calculated in that manner, high accuracy missing data approximations for the damaged gait signals were acquired.

Gait and the Brain

EEG: Protocol

Twenty subjects, 10 healthy young adults and 10 healthy older adults, participated in this study. Participants were excluded if they had: cognitive impairments as demonstrated by a score of less than 20 on the Montreal Cognitive Assessment [94], a history of any neurological disorder that would likely affect their walking or cognitive performance, the inability to walk at least five minutes, unstable medical condition including cardio-vascular instability, hearing problems or significant psychiatric or orthopedic co-morbidity. The study was approved by the local ethical committee of Sourasky Medical Center and was performed according to the principles of the Declaration of Helsinki. All participants gave their informed written consent prior to participation.

All participants walked on a treadmill with and without the simultaneous performance of the auditory oddball task. Wireless EEG was recorded via 20-channel EEG cap (Enobio 20 Neuroelectrics, Barcelona) and gait was assessed using 3D-inertial measurement units (IMUs) that were attached to the right and left ankles (Opal™, APDM). Subjects were secured by a harness attached to the ceiling and gait speed was set according to the comfortable speed of each subject. The same gait speed was used during usual and oddball walking. The auditory stimuli consisted of 600 Hz tone bursts as standard stimuli and 1200 Hz tone bursts as target stimuli. The tones were presented in a randomized order, with a stimulus interval raging between 2.8 and 3.2 seconds. Each of the oddball tasks lasted two minutes and consisted of 40 stimuli tones; 30 standard tones and ten odd high frequency tones considered the target stimuli (25% of total tones). The subjects were instructed to count the target tones silently and report the total odd tones number at the end of each session. Three oddball tasks were performed during walking on a treadmill at the subjects' comfortable speed (a total of 90 standard tones and 30 odd tones) and one continuous walking task of two minutes on a treadmill without oddball. The order of the conditions was randomized. After completing the walking tasks, participants performed the color trail test (CTT) to assess attentional and executive function.

EEG: SDET Peak Detection

EEG signals during walking are extremely noisy and distorted. To compensate for that, the filtering technique must be robust and accurate. Furthermore, the decision of point adjustment cannot be simply set to the highest peak, as it was in gait research, because unlike in case of gait, in EEG it is very important to accurately detect the time stamp of the peak. In [31], SDET was used to detect peak locations of the GRPs. These temporal signals were treated as quasi-periodic noisy signals which in this particular case had exactly two periods representing the two steps within the stride. The procedure was defined as follows:

Denote $f_0(t)$ as the signal with maxima points that we would like to detect. Next, denote $f_1(t)$, $f_2(t)$ and $f_3(t)$ as instances of $f_0(t)$ which underwent smoothing filtering (i.e. filtration stages):

1. Define $\lambda = 10^4$ (empirical value for this type of data)
2. Apply Hodrick-Prescott (HP) filter on $f_0(t)$ using the defined λ
3. Count the instances of local maxima
    a. If meets the set criteria (see below), denote filtered signal as $f_k(t)$, where $k = \{1,2,3\}$
    b. If not, define $\lambda = 1.01\lambda$ (an increase of 1% of filtration strength) and repeat the process beginning from step (2).
4. Complete when $f_1(t)$, $f_2(t)$ and $f_3(t)$ are defined.

In our case, the criteria were set to two instances for $f_3(t)$, three instances for $f_2(t)$ and four instances for $f_1(t)$. If one of the criteria was not met due to, for example, signal having only two or three waves to begin with, we excluded the corresponding stages from the process. Once all the filtered stages of the signal were calculated, we detect all local maxima points on each one of the four signals $f_n(t)$, where $n = \{0,1,2,3\}$. Denote M_n as a set of coordinates (x_i, y_i) representing local maxima of signal $f_n(t)$ where i is the index of a specific coordinate. Define (x_{01}, y_{01}) as first maxima point of $f_3(t)$ and (x_{02}, y_{02}) as second. Next, track the extremum locations of each of the two maxima back to the original and unfiltered signal as follows:

Define (x_a, y_a) as current maxima location (one of the maxima points from $f_3(t)$).

1. Define $p = 2$
2. For every (x_i, y_i) from M_p calculate: $w_i = \frac{\frac{y_i - y_a}{\Sigma_j(y_j - y_a)}}{\frac{|x_i - x_a|}{\Sigma_j|x_j - x_a|}}$ for each i
3. Set $(x_a, y_a) = (x_i, y_i)$ corresponding to $\max_i w_i$
4. Set $p = p - 1$ and repeat the process from (2) Continue until receival of extremum coordinates of $f_0(t)$.

Repeat this process for every maxima point from $f_3(t)$. At the end of the procedure, (x_a, y_a) are the coordinates of the correct peak location on the initial signal.

EEG: APC Assessment

To measure the consistency of ERP responses, we used an Amplitude Pattern Consistency (APC) parameter. Denote $f_0(\mathrm{t})$ as signal for assessment. Using linear transformation, the signal was rescaled into a range of [0,1]:

$$f_1(\mathrm{t}) = f_0(\mathrm{t}) - \min_{\mathrm{t}} f_0(\mathrm{t})$$

$$f_2(\mathrm{t}) = \frac{f_1(\mathrm{t})}{\max_{\mathrm{t}} f_1(\mathrm{t})}$$

Define $(\mathrm{x_p}, \mathrm{y_p})$ as local maxima of signal $f_2(\mathrm{t})$ where $\mathrm{p} = 1,2,3, \ldots \mathrm{n}$ is the index of a specific peak coordinate. Next, a matrix of amplitude ratios is constructed:

$$\mathrm{A} = \begin{bmatrix} \mathrm{a}_{1,1} & \cdots & \mathrm{a}_{1,\mathrm{n}} \\ \vdots & \ddots & \vdots \\ \mathrm{a}_{\mathrm{n},1} & \cdots & \mathrm{a}_{\mathrm{n,n}} \end{bmatrix}$$

Where $\mathrm{a}_{\mathrm{i,j}} = \frac{\mathrm{y_i}}{\mathrm{y_j}}$. The received matrix is adjusted using the following steps:

$$\mathrm{B} = \mathrm{A} - \min_{\mathrm{i,j}}(\mathrm{a}_{\mathrm{i,j}}) \cdot 1_{\mathrm{n}}$$

$$\mathrm{C} = \frac{1}{\max_{\mathrm{i,j}}(\mathrm{b}_{\mathrm{i,j}})} \cdot \mathrm{B}$$

where:

$$1_{\mathrm{n}} = \begin{bmatrix} 1 & \cdots & 1 \\ \vdots & \ddots & \vdots \\ 1 & \cdots & 1 \end{bmatrix}, \quad \mathrm{B} = \begin{bmatrix} \mathrm{b}_{1,1} & \cdots & \mathrm{b}_{1,\mathrm{n}} \\ \vdots & \ddots & \vdots \\ \mathrm{b}_{\mathrm{n},1} & \cdots & \mathrm{b}_{\mathrm{n,n}} \end{bmatrix}, \quad \mathrm{C} = \begin{bmatrix} \mathrm{c}_{1,1} & \cdots & \mathrm{c}_{1,\mathrm{n}} \\ \vdots & \ddots & \vdots \\ \mathrm{c}_{\mathrm{n},1} & \cdots & \mathrm{c}_{\mathrm{n,n}} \end{bmatrix}$$

APC parameter is then defined as:

$$\gamma = \frac{1}{\mathrm{n}^2} \sum_{\mathrm{i}} \sum_{\mathrm{j}} \mathrm{c}_{\mathrm{i,j}}$$

This parameter produces high values when signal has high consistency in amplitudes of signal wave pattern and low values when the amplitudes are inconsistent [Figure 7].

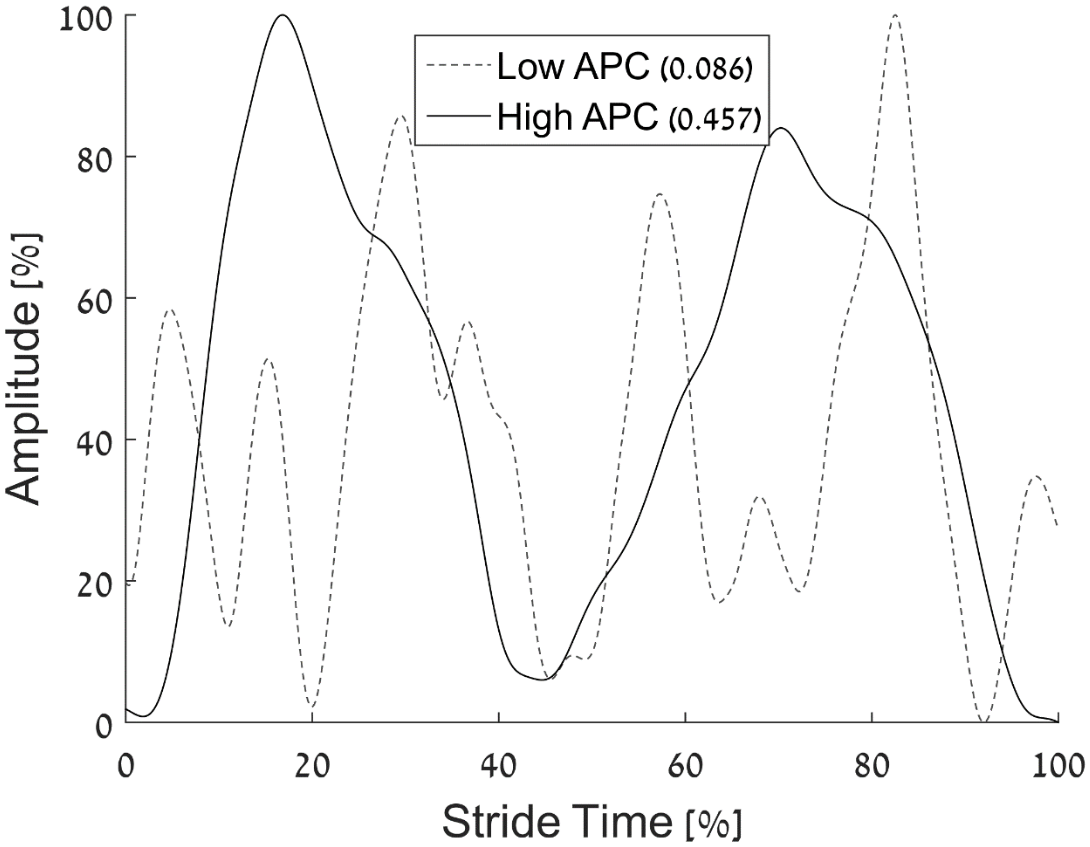

Figure 7. An example of electrical brain pattern of one subject with low APC – dashed line and one subject with high APC – solid line. Each pattern represents average of 200 gait cycles.

EEG: Other Procedures

Assessment of the effects of aging and PD on cognitive performance during dual task walking [64].

Data processing was performed to clean artifacts. This was done for both conditions; standing and walking, and included: (1) band pass FIR filter 1–40 Hz to reduce motion artifacts, drift and high-frequency contamination (2) rejection of channels with prominent artifact based on visual inspection, (3) adaptive independent component analysis mixture model algorithm (AMICA) using the default extended-mode training parameters, (4) rejection of artifactual components based on manually inspection and SASICA toolbox [95]. Matlab EEGLAB toolbox [96] was used for the analysis. The analyzed signals were divided into 3 seconds epochs, 1 second pre-stimulus and 2 seconds post-stimulus. Epochs with probability of occurrence >3 SD from the mean across all epochs were rejected from further analysis to reduce noise [97]. For ERP analysis, we randomly chose the same number of standard trials as the odd trails and averaged 20 different combinations to represent the ERP of standard trials. This was performed due to the different frequency of odd and standard trials (ratio of 1:4). P300 was identified from the maximum positive deflection peak between 250ms and 650ms from the stimulus. Amplitude and latency of the signal were evaluated at a 100ms time window (50ms before and after the P300 detected event) and compered to pre-stimulus (at 200ms). P300 was measured from channel Pz as P300 scalp distribution is defined as the amplitude change over the midline electrodes (Fz, Cz, Pz), which typically increases in magnitude from the frontal to parietal electrode sites [98].

Means and standard errors were calculated for all dependent variables. In order to account for variability and gain symmetry we transformed P300 latency into Log latency and P300 amplitude into square amplitude based on Box cox variance stability methods [99]. Liner mixed model analysis was used to examine the effect of condition (standing vs. walking), group (healthy young, healthy older adults, and patients with PD), and condition by group interaction on P300 amplitude and latency, while controlling for age, gender, and gait speed. Univariate ANOVA was performed to compare between groups during each one of the conditions (standing and walking) including measures of gait and cognition. The associations between P300 measurements and motor and cognitive performance were explored using Pearson correlation coefficients. Statistical significance was set to p = 0.05. Statistical analysis was performed using SPSS for Windows version 22.

Two 3D-IMUs attached to the right and left ankles (OpalTM, APDM) were used to determine spatiotemporal gait characteristics while walking on the treadmill. Gait measurements included gait speed and stride and step regularity, a measure of the consistency of the stride-to-stride or step-to-step pattern. These measures were calculated by an unbiased autocorrelation procedure that analyzed the pattern of acceleration in the vertical, mediolateral and anteroposterior directions [100]. Dual task (DT) cost, a measure that reflects the effect of the second task on gait ability, as compared with baseline single task walking was calculated as, DT cost = 100 x (single-task step/stride regularity - DT step/stride regularity)/single-task step/stride regularity.

In this section, the processing and analysis was performed mainly using the existing tools and previously proposed solutions with addition of our own, minor automation algorithms. This was essential part of assessment before analyzing the gait related potential that is described in the following section.

Assessment of gait related potential [31].

EEGLAB toolbox [96] was used for the preprocessing of the raw data collected during the trials. The data were filtered using 1-40Hz Band Pass Filter (BPF). Next, independent component analysis (ICA) was used to calculate components and remove artifacts. After the reconstruction of the signals from the remaining components, the data were cut into stride epochs, which were thereafter resampled using cubic-spline interpolation in order to match the number of samples in each epoch. Finally, the epochs were grand averaged to compute the stride activation patterns. Recording EEG while walking resulted in substantial noise, some of which remained after the above-mentioned process. These noise was mainly high frequency artifacts. Since EEG signals are non-stationary, Hilbert-Huang Transform (HHT) [101] was used to decompose the EEG signals into Intrinsic Mode Functions (IMF) using Empirical Mode Decomposition (EMD) [102]. Next, the IMF containing the highest frequency range was removed and the signals were reconstructed and slightly smoothened using Hodrick–Prescott (HP) filter with $\lambda = 10^4$.

To rule out the possibility of auditory events creating the observed patterns, we compared between epochs of auditory sound within the first half of the gait cycle (defined as a stance) and those within the second half of the gait cycle (defined as a swing). We assumed that if the GRPs are largely affected by sound, differences in the EEG signal spatiotemporal characteristics will be found between the two groups of epochs.

Means and standard errors were calculated for all dependent variables. Linear mixed model analysis was used to examine the effect of task (usual walking vs. dual task walking), group (healthy young vs. healthy older adults), and task x group interaction on gait measures (e.g., stride time, stride time variability) and GRPs in the central channels (e.g., amplitude, latency, and APC) while controlling for gender and gait speed. The associations between gait measures and electrical brain measures of gait cycle were explored using Pearson correlation coefficients. Statistical significance was set to p=0.05. Statistical analysis was performed using SPSS for Windows version 22.

The two 3D-IMUs were used to determine spatiotemporal gait characteristics while walking on the treadmill [103]. Gait measurements included gait speed that was constant during usual and dual task, mean stride time, and stride time variability. These measures were calculated by an unbiased autocorrelation procedure that analyzed the pattern of acceleration in the vertical, mediolateral and anteroposterior directions [100].

Heel strike events were detected using the accelerometers as described below [103]. By coupling the signals from both accelerometers, the algorithm detected regions in the signal that were defined as swings of each leg. Using the assumption that during gait only one leg can be at swing phase at a given time, parts of the signal were marked as stance regions. Heel strike was identified in the stance region as the minimum value in the medial-lateral angular velocity signal that occurs before the instant of maximum peak in the anterior-posterior acceleration of the same leg [103]. This process was repeated for each step and leg.

Brain Research

fNIRS: Setup

Twenty-five subjects (at the time of this report, the data is still being collected), 6 Major Depressive Disorder (MDD) patients, 7 Attention Deficit and Hyperactivity Disorder (ADHD) subjects and 12 healthy subjects were recruited as part of a general study on brain disorders. None of the subjects had any known cardio-respiratory ailments. The study was approved by the institutional ethical review board of Sourasky Medical Center, Tel Aviv, Israel. All subjects signed an informed consent.

The NIRS system (ETG-4000, Hitachi, Japan) includes 10 emitters (695nm and 830nm), and 10 detectors - Avalanche Photodiodes (APD), with a sampling frequency (f_s) of 10 Hz. They are coupled to the tissue using optical fibers and are positioned over the temporal lobes of the head. Figure 8 shows the locations of the emitters and detectors using the 10-20 system. Twenty-four (24) channels, defined between pairs of emitters and detectors located 3cm apart, (twelve on each hemisphere), are available using this topographical arrangement.

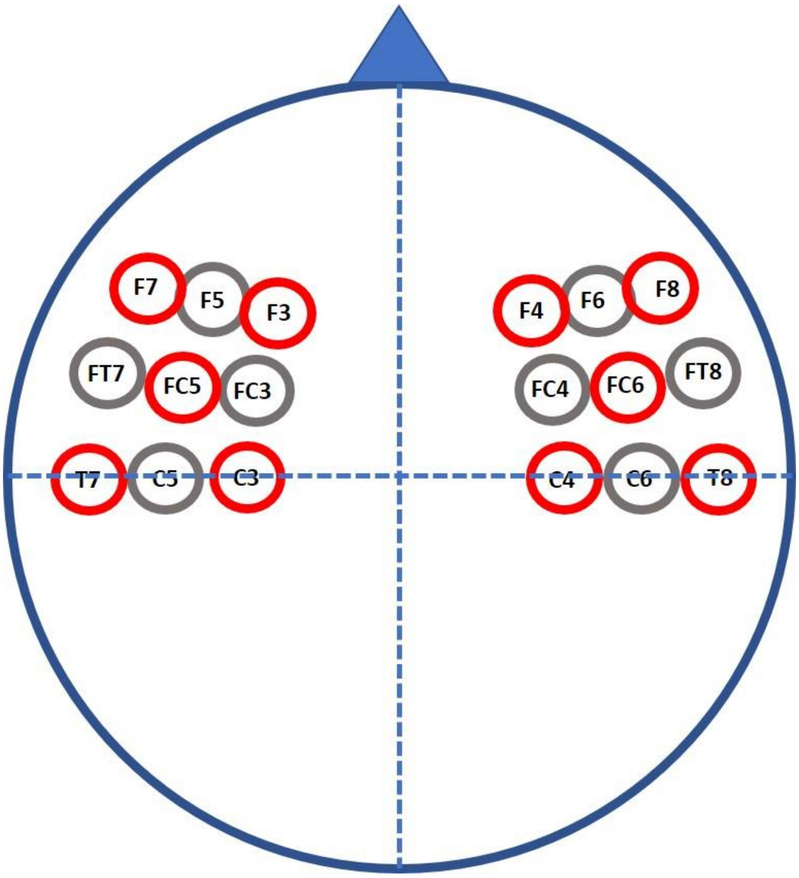

Figure 8. Arrangement of NIRS optodes based on the 10-20 system. RED-emitters, Grey-detectors.

Subjects were asked to sit quietly in front of a dark screen for 300 seconds, with their eyes open, while fixating on a white cross at the center of the screen. Following, they performed a cognitive Go-NoGo task that consisted of random letters. Whenever a letter appeared on the screen, the subjects were required to press a button using their finger. Any time the letter "X" appeared, they were to refrain from pressing the button. The task was composed of three (3) blocks of about 220 seconds long. A subgroup of subjects performed the experiment twice, once using NIRS setup as explained above and once more while lying supine inside a 3 Tesla MRI machine.

Definitions

Throughout the "Brain Research" section, the following parameters are fixed:

- The sampling frequency is denoted as f_s
- The half window size for window-based algorithms is 2.5 seconds long and the number of samples within that window is defined as N. That value was chosen because hemodynamic response function peaks at 6-8 seconds following stimulation [92]. Hence, our window size is 5sec ($2N$) when we require a window shorter than the response time and 10sec ($4N$) when the required window should be longer than the response time.
- The calculated change in concentration of oxyhemoglobin signals denoted as $\tilde{S}_c$ where $c = 1,2,\dots,\eta$ is the number of the channel and η is the total number of channels. In our case the initial value of η is 24.
- The number of samples in each signal is denoted as L.

fNIRS: MVE

When setting up a fNIRS headset, in some cases, the coupling of the fibers, or optical elements, to the head may introduce artifacts and noise due to poor coupling. These NCs should not be used for analysis regardless of the preprocessing methods. In Figure 9, an example of ΔHbO2 concentration recorded from one subject is presented. In the panel (a) all channels are shown, and in the lower panel the noisy channel (panel c) is separated from the remaining clean channels (panel b).

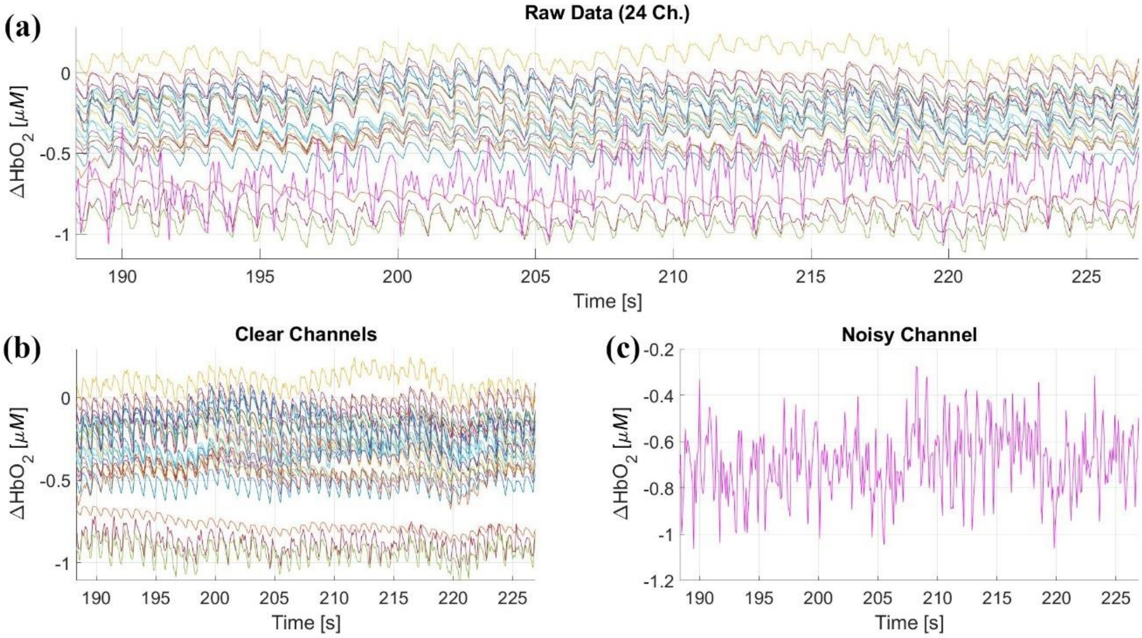

Figure 9. Presenting all the channels with one exhibiting a coupling artifact. Panel (a)-all channels, (b)-clean channels, without noise, (c)-noisy channel.

NCs, if not detected properly, affect the result of analysis and in some cases may even lead to wrong conclusions. Therefore, it is essential to detect them and exclude from any analyses of the data. In order to detect NCs automatically, we developed the Maximal Variability Expectation (MVE) algorithm. As fNIRS signals are strongly affected by the systemic physiological parameters. Cardio-respiratory activity becomes the main component of all the recorded signals regardless of their position on the head. This temporal activity is a quasi-periodic, nearly wide-sense stationary process that should demonstrate a statistical behavior of a bell-like shaped distribution. Chiarelli et. al. [85] for example, look for Gaussian distribution outliers within wavelet coefficients of the signals in order to detect the ones that correspond to artifacts. Our algorithm assumes bell-like or half bell-like shaped statistical distribution, but does not require a specific distribution type, therefore, in the following algorithms we refer to all such distributions as Quasi-Bell (QB) distributions. The expectation value of fNIRS signals holds no information regarding brain activity, and may complicate the statistical and probabilistic calculations, thus it is removed from each signal:

$$S_c = \tilde{S}_c - E\left[\tilde{S}_c\right]$$

Where $E[\cdot]$ represents the expectation operator. To simplify the following calculations let us assume that S_c is a gaussian random process. Following that assumption, the Running Standard Deviation (RSD) was calculated as follows:

$$\overleftrightarrow{S}_c(n) = \begin{cases} S_c(N+1-n) & , \quad 0 < n \le N \\ S_c(n-N) & , \quad N < n \le L+N \\ S_c(2L+N+1-n) & , \quad L+N < n \le L+2N \end{cases}$$

$$V_c(n) = \sqrt{\frac{1}{2N}\sum_{i=n}^{n+2N}\left(\overleftrightarrow{S}_c(i) - \frac{1}{2N+1}\sum_{j=n}^{n+2N}\overleftrightarrow{S}_c(j)\right)^2} \quad , \quad n = 1,2,\dots,L$$

The RSD procedure can be regarded as sampling of the standard deviation. The distribution of the sample variance collected from a gaussian process, has Chi-squared distribution ([104], [105]). In case of standard deviation, we get a root Chi-squared distributed random variable which has a Chi distribution. Chi distribution also falls under the QB type of distributions. Next, in order to maintain the signal's length we repeat the padding process as defined above, on the V_c while N is substituted with $2N$. The received $\overleftrightarrow{V}_c$ is used to calculate the Running Maximum:

$$M_c(n) = \max_{n \le i \le n+4N}\left\{\overleftrightarrow{V}_c(i)\right\} \quad , \quad n = 1,2,\dots,L$$

Similarly to RSD, the Running Maximum procedure can be seen as sampling of the maxima value. If we examine the maxima value distribution of Chi distributed process, the resulting process has a Gumbel distribution [106], which can also be categorized as a QB distribution. The expectation value of these Gumbel distributed random variables is then calculated:

$$e_c = E[M_c]$$

We can interpret e_c as observations that are calculated by a mean of a large number of samples from a Gumbel distributed random variable. Based on the Central Limit Theorem we can deduce that e_c are observations of some QB distributed random variable. Since cardio-respiratory dynamics are the same regardless of the location of the measurements, $\forall c, e_c$ is a sample of a random process tightly related to cardio-respiratory dynamics. When all of the channels are recording properly, every such sample is related to the same process, whereas any channel recording noise or some other high energy artifact throughout most of the recorded trial has a statistical probability that originates from a different source. Let us define $X \sim \widetilde{N}(\mu_x, \sigma_x)$ as a random variable originating from the cardiorespiratory source. We assume a QB distribution, denoted as $\widetilde{N}$, based on the explanation provided above. Let us denote Y as a random variable with an unknown distribution that originates from the non-cardiorespiratory sources and $\mu_y = E[Y]$. Meaning that $e = X$ with probability of p and $e = Y$ with probability of $1 - p$. Note that X cannot yield negative samples due to the procedure by which it was acquired. We assume that the recording was done properly, thus the majority of collected signals are reliable. Implying that $p \gg 1 - p$. We also assume that $\mu_y \notin \{\mu_x \pm \sigma_x\}$ [Figure 10].

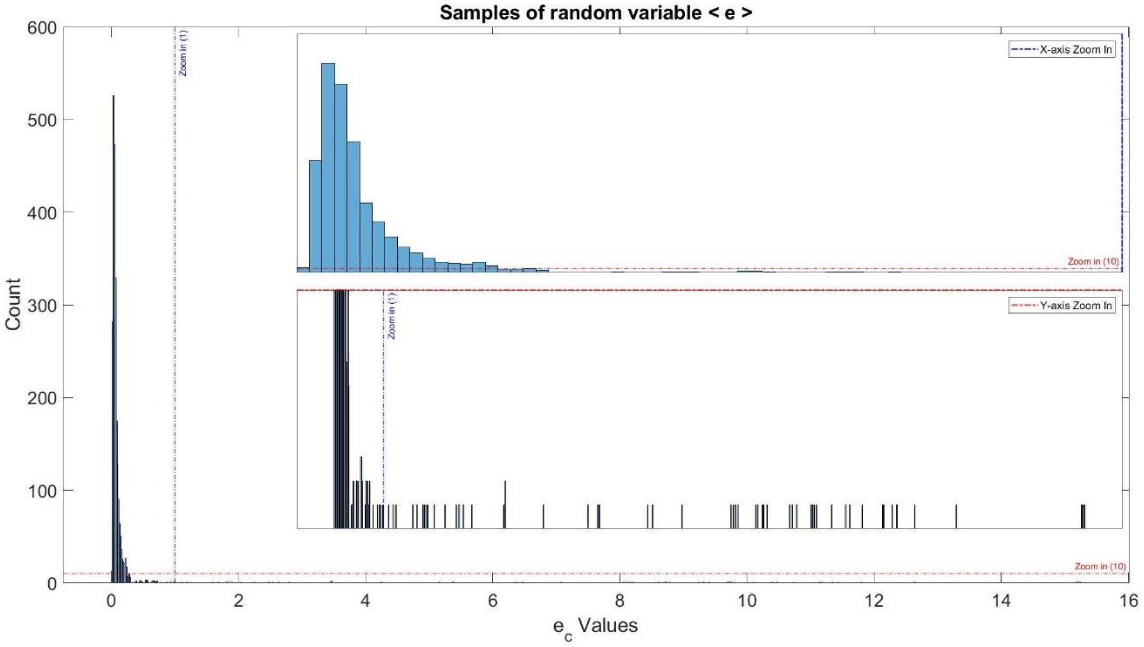

Figure 10. The graph presents samples of the random variable e collected from all the subjects. Zooming in on the X-axis (upper inset) shows a clear half-gaussian or QB distribution as was defined earlier. Zooming in on the Y-axis (lower inset) shows the unbalanced tail of the received QB distribution.

When examining Figure 10, it is evident that the assumptions made regarding the distributions of X and Y random variables were correct. We can see the QB distribution associated with random variable X (upper inset of Figure 10) that is tightly related to the cardio-respiratory dynamics and the high value readings associated with random variable Y that originate from unknown source (lower inset of Figure 10), unrelated to the cardio-respiratory dynamics. To the best of our knowledge, none of the subjects had any known disorders related to the cardiorespiratory system, thus it is safe to assume that samples of random variable e collected from different subjects would have a similar behavior, thus the presented graph provides some insights on the statistical behavior that should be expected for every subject independently. Next, the statistics of e are calculated:

$$\mu_e = E[e] \quad and \quad \sigma_e = \sqrt{E[(e-\mu_e)^2]}$$

$$\gamma_e = E\left[\left(\frac{e-\mu_e}{\sigma_e}\right)^3\right]$$

The received skewness value γ_e is then used to determine which of the samples e_c originated from random variable Y. Let us assume that:

$$e_1 \le e_2 \le, \dots$$

We truncate the set of samples $\{e_1, e_2, \dots\}$ until $\gamma_e < 1$. Meaning that the distribution of e is QB since a Half-Gaussian, or in our case a Half-Bell distribution has a skewness of just under 1. Our assumption is that all of the removed samples using this process originate from Y, meaning they represent the NCs.

fNIRS: CSV

The goal of the Cross Segment Validation (CSV) algorithm is to identify motion artifacts within the recorded signals. For this algorithm, it is important to exclude the NCs from the calculation as they heavily affect the results and accuracy of the method. Meaning that in our case, the value of η may be lower than 24. In addition, the CCFA algorithm was used to remove the time dependent first statistical moment ($k_{ord} = 4N$). Next, RSD is calculated in the same manner as in MVE (denoted as $\hat{V}_c$) using the CCFA filtered signals (denoted as $\hat{S}_c$) and followed by averaging:

$$V_A(n) = \frac{1}{\eta}\sum_{c=1}^{\eta} \hat{V}_c(n) \quad , \quad n = 1,2,\dots,L$$

Afterwards, ordered pair (t_s, t_e), representing borders of a section with the lowest variability are calculated as follows:

$$(t_s, t_e) = \left\{(n, n+4N) \quad \middle| \quad \frac{1}{4N+1}\sum_{i=n}^{n+4N} V_A(i) \le \frac{1}{4N+1}\sum_{i=m}^{m+4N} V_A(i) \quad , \quad \forall m\right\}$$

The running maximum M_A is calculated for V_A in the same manner as was described in the MVE algorithm. An auxiliary function is then constructed by quantization of M_A. A single quantization level is defined as:

$$q = \underset{4N}{\text{kmin}}\{V_A\}$$

Where $\underset{k}{\text{kmin}}\{\cdot\}$ is the kth smallest element operator. The quantization levels: $0,\ q,\ 2q,\ 3q, \dots$ define the possible values of the auxiliary staircase function as follows:

$$f(n) = \{iq \quad | \quad |M_A(n) - iq| \le |M_A(n) - jq| \quad , \quad \forall j\}$$

We determined that sections containing potential artifacts have values of above $2q$ on the auxiliary function [Figure 11].

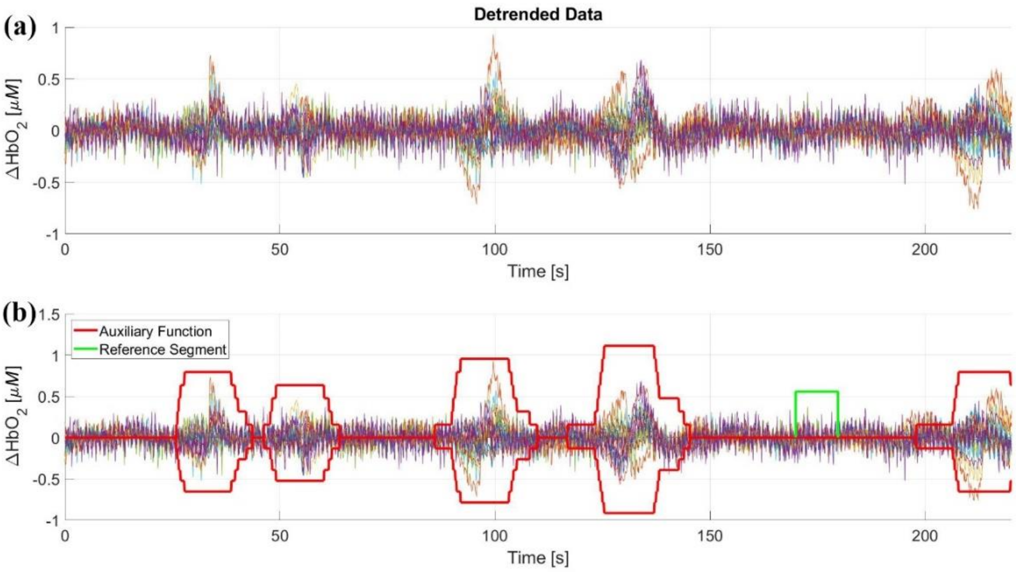

Figure 11. Panel (a) - changes in HbO$_2$ for all channels. Panel (b) - The auxiliary function is displayed in red both as positive values and symmetrically flipped: $\pm f(n)$. The amplitude was normalized to match the signal's as it holds no significance. The green section shows the detected reference segment.

Therefore, let $\{(n_{2m-1}, n_{2m})\}_{m=1}^{d}$ be a sequence of all ordered pairs where the values of the auxiliary function are above 2q:

$$\forall n \in \bigcup_{m=1}^{d} [n_{2m-1}, n_{2m}] \quad , \quad 3q \leq f(n)$$

Where d is the number of such pairs. In order to improve the temporal resolution of identifying artifacts, we further divide these noisy signal segments into sub-segments that have a length of 1s and an overlap of 0.5s:

$$\bigcup_{m=1}^{d} \left\{ \left(n_{2m-1}, n_{2m-1} + \tilde{f_s}\right), \left(n_{2m-1} + \frac{1}{2}\tilde{f_s}, n_{2m-1} + \frac{3}{2}\tilde{f_s}\right), \dots, \left(n_{2m} - \tilde{f_s}, n_{2m}\right) \right\}$$

Where $\tilde{f_s}$ is a number of samples within 1s, meaning it is equal to the sampling frequency f_s.

For convenience, let us redefine the ordered pairs as follows:

$$\begin{cases} \left(n_1, n_1 + \tilde{f_s}\right) & = & (x_1, y_1) \\ \left(n_1 + \frac{1}{2}\tilde{f_s}, n_1 + \frac{3}{2}\tilde{f_s}\right) & = & (x_2, y_2) \\ \vdots & \vdots & \vdots \\ \left(n_{2d} - \tilde{f_s}, n_{2d}\right) & = & (x_\alpha, y_\alpha) \end{cases}$$

The new set is denoted as $P_A = \bigcup_{j=1}^{\alpha} \{(x_j, y_j)\}$, where α is the number of artifact sub-segments. Similarly, we divide segment (t_s, t_e) and redefine the pairs:

$$\left\{ \left(t_s, t_s + \tilde{f_s}\right), \left(t_s + 1, t_s + \tilde{f_s} + 1\right), \dots, \left(t_e - \tilde{f_s}, t_e\right) \right\}$$

$$\begin{cases} \left(t_s, t_s + \tilde{f_s}\right) & = & (u_1, v_1) \\ \left(t_s + 1, t_s + \tilde{f_s} + 1\right) & = & (u_2, v_2) \\ \vdots & \vdots & \vdots \\ \left(t_e - \tilde{f_s}, t_e\right) & = & (u_\beta, v_\beta) \end{cases}$$

$$P_R = \bigcup_{\tau=1}^{\beta} \{(u_\tau, v_\tau)\}$$

Where β is the number of reference sub-segments. The sets representing reference segments P_R and the potential artifact segments P_A are then used to compare the statistical behavior of potential artifacts and the reliable, reference data. The average variability of a reference segment was calculated by:

$$\sigma_1^2 = \frac{1}{\eta(t_e - t_s)} \sum_{n=t_s}^{t_e} \sum_{c=1}^{\eta} \left[\hat{S}_c(n) - \frac{1}{\eta} \sum_{c=1}^{\eta} \hat{S}_c(n) \right]^2$$

Followed by the calculation of the variability in a potential artifact segment and the combined statistics of both reference segment and a potential artifact segment:

$$\forall (x_j, y_j) \in P_A \quad , \quad \sigma_2^2(j) = \frac{1}{\eta \tilde{f}_s} \sum_{n=x_j}^{y_j} \sum_{c=1}^{\eta} \left[\hat{S}_c(n) - \frac{1}{\eta} \sum_{c=1}^{\eta} \hat{S}_c(n) \right]^2$$

$$\mu_{j,\tau}(n) = \begin{cases} \frac{1}{2\eta} \sum_{c=1}^{\eta} \left(\hat{S}_c(n) + \hat{S}_c(n - x_j + u_\tau) \right) & , \quad x_j \le n \le y_j \\ \frac{1}{2\eta} \sum_{c=1}^{\eta} \left(\hat{S}_c(n) + \hat{S}_c(n - u_\tau + x_j) \right) & , \quad u_\tau \le n \le v_\tau \end{cases}$$

$$\sigma_3^2(j) = \frac{1}{2\beta\eta\tilde{f}_s} \sum_{\tau=1}^{\beta} \left[\sum_{n=x_j}^{y_j} \sum_{c=1}^{\eta} \left[\hat{S}_c(n) - \mu_{j,\tau}(n) \right]^2 + \sum_{n=u_\tau}^{v_\tau} \sum_{c=1}^{\eta} \left[\hat{S}_c(n) - \mu_{j,\tau}(n) \right]^2 \right]$$

Where $\mu_{j,\tau}(n)$ is the expectation approximation over all the channels from both reference and potential artifacts combined. Note that the distance between each ordered pair of indices in P_A and P_R is equivalent to one second, thus: $\forall j, \tau \quad y_j - x_j = v_\tau - u_\tau = \tilde{f}_s + 1$. If the statement $\left(th_{1,3} \cdot \sigma_1^2 < \sigma_3^2(j) \right) \quad \vee \quad \left(th_{1,2} \cdot \sigma_1^2 < \sigma_2^2(j) \right)$ is true, the corresponding segment $[x_j, y_j]$ is labeled as an artifact, where $th_{1,3} = 12$ and $th_{1,2} = 2.75$ are empirically determined thresholds. Note that each of the two variability parameters σ_2^2, σ_3^2 are sensitive to different types of artifacts. The σ_2^2 parameter is more sensitive to artifacts that produce dispersion between the channels while σ_3^2 is more sensitive to artifacts that create a channel-wise synchronized spike. Next, an iterative process was applied to account for the attenuation of the artifact:

$$x_j^{(i+1)} = \max_n \left\{ n \in \left[x_j^{(i)} - 2N, x_j^{(i)} - 1 \right] \quad \middle| \quad f(n) < f\left(x_j^{(i)} \right) \right\}$$

$$y_j^{(i+1)} = \min_n \left\{ n \in \left[y_j^{(i)} + 1, y_j^{(i)} + 2N \right] \quad \middle| \quad f(n) < f\left(y_j^{(i)} \right) \right\}$$

The process is repeated until convergence $\forall j$. The purpose of the last step is to inspect the sections just before and after the detected segment. Using the proposed procedure, the slope of the auxiliary function was assessed and if it was sharp (meaning that: $f(n_2) - f(n_1) > 0$), the detected segment was extended to include it.

fNIRS: Spike Detection

In addition to prolonged motion artifacts, sudden spikes may also appear on one or more channels as can be seen in Figure 12.

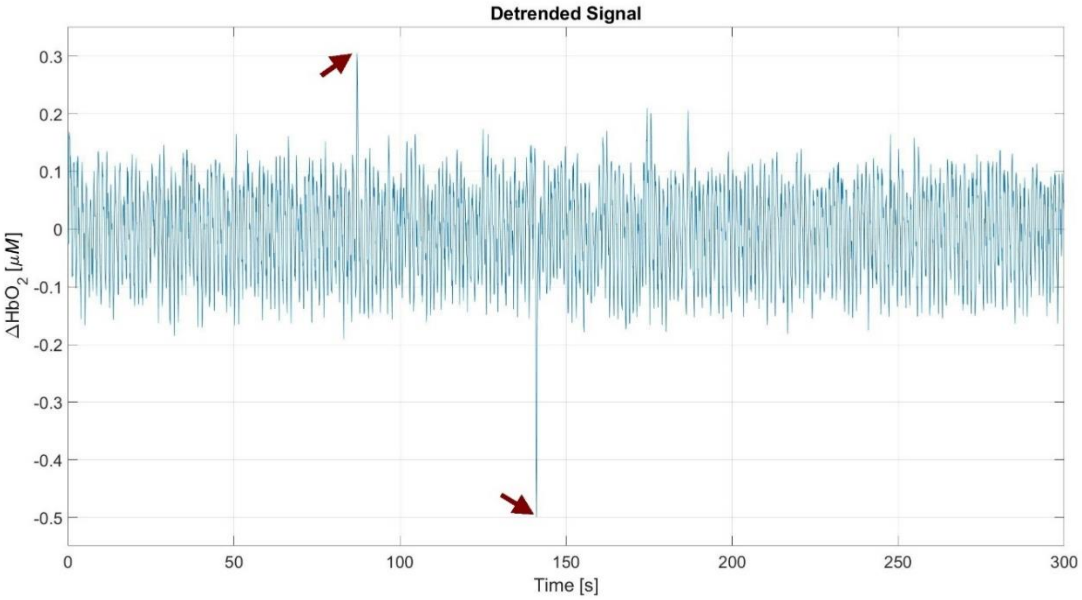

Figure 12. Graph presents a single channel with visible spike artifacts.

We propose a procedure that allows for the detection of such artifacts using scaled Median Absolute Deviation (sMAD). Samples that exceed three sMAD away from the median, were detected as outliers that represent high amplitude artifacts such as spikes. Each non-NC was assessed using the suggested outlier detection. The resulting detection is very localized to the spikes' occurrences and does not include the area close to the spike itself which is commonly affected by the spike as well. To compensate, morphological dilation, with a structure element size of 2N, was applied. From our observations, we deduced that the affected period after the artifact is longer than the period before it. Therefore, additional morphological dilation with the size of N was performed only on the periods after the artifacts.

fNIRS: CCFA – Detrending

The temporal information in fNIRS signals is non-stationary. Some of the components are quasi-periodic, while others are not. Therefore, CCFA algorithm was used to approximate and remove the time dependent first statistical moment $m_{[1]}(n)$ where $n = 1,2,\dots,L$. In this case, the Open-Loop ($\lambda = 0$) approximation was used due to its relative smoothness compared to other sub-procedure types and its relative robustness to noise within the initial data. The value of k_{ord} was empirically concluded to be $k_{ord} = 45N$. A linear polynomial curve fitting function ($p_{ord} = 1$) was used for the approximation procedure. Reliability weights were neutralized $\forall j,\ \ \beta_j = 1$ since there were no missing samples and we had no information regarding the accuracy of the sampling process. All the remaining parameters were defined as suggested by default, the uniform distribution for the recombination weights was set to $\omega_{k-m} = \frac{1}{k_{ord}}$ and source function weight was set to zero, $\omega_0 = 0$. Under the settings defined above, the simplified equation can be used:

$$\tilde{s}_n = \frac{\omega_0 \cdot s_n^{(0)} + \sum_{m=0}^{k-1} \omega_{k-m} \cdot f_{m+1}^{(n-m-1)}}{\sum_{m=0}^{k} \omega_{k-m}}$$

Once the recombination weights are assigned, the equation becomes even simpler:

$$\overleftrightarrow{m}_{[1]}(n) = \frac{1}{k_{ord}} \cdot \sum_{m=0}^{k-1} f_{m+1}^{(n-m-1)}$$

The proposed procedure provides the $m_{[1]}(n)$ function that is subtracted from the raw signal. Just like many other window-based procedures, CCFA requires padding of the signal to avoid information loss at the borders. The type of padding is very important for CCFA, as it will strongly affect the resulted approximation near the borders of the signal. We used a weighted trend padding to assure that window's entrance gradient matches the signal's gradient. The padding size is equal to k_{ord} on each side of the signal. The weights for the weighted line fit were assigned as one divided by the distance of the sample to the edge that is being extended. The extrapolation of the fitted line is defined to be the padding of the signal at that border. Let us denote the resulted padded signal as $\overleftrightarrow{S}_c(i)$. The time dependent first statistical moment is then calculated using the $\overleftrightarrow{m}_{[1]}(i)$ that is received by applying CCFA onto $\overleftrightarrow{S}_c(i)$ and trimmed as follows:

$$m_{[1]}(n) = \overleftrightarrow{m}_{[1]}(n + k_{ord})$$

where $n = 1,2, \dots, L$ and L is the length of the signal. The detrended signal is then simply calculated: $\hat{S}_c(n) = S_c(n) - m_{[1]}(n)$, where $S_c(n)$ is the raw signal and $\hat{S}_c(n)$ is the resulting detrended one.

fNIRS: ICF

When processing the temporal information in fNIRS signals, it is essential to firmly understand what type of information is relevant for the study. The recorded signals create a phenomenon often called a "cocktail party". It basically means that the recorded signals contain mixed inputs from multiple sources. Those sources are referred to as "signal components". It is important to identify as many such components as possible in order to reduce the effects of the irrelevant ones on the target of the study. We refer to all components obscuring the target of the study as noise. For example, the cardio-vascular or cardio-respiratory system has a very dominant and robust, quasi-periodic component within the recorded signals, but it has no significant information regarding neuronal activation patterns or brain hemodynamics. Therefore, to analyze them, the cardio-vascular system's component should be removed from the signals, meaning that it can be considered as part of the noise contaminating the desired information.

When using standard spectral filtering techniques, one should be careful since these methods may not be applicable for all of the components of the signals. This is due to the stationarity assumption of most of the standard filtering methods, which may not be true for some of the components. Therefore, unless it is clear that there are no significantly non-stationary components within the signals, one should avoid using standard Spectral Band Filtering (SBF) (e.g. Fourier transform based filtering). Since we know that the fNIRS signals are non-stationary and we have no knowledge regarding which components are non-stationary and how far are they from the definition of WSS, we propose an alternative method of filtration named Intrinsic Component Filtering (ICF).

Empirical Mode Decomposition (EMD) from the Hilbert-Huang Transform (HHT) [87] was used to decompose each channel into Intrinsic Mode Functions (IMFs). EMD does not assume stationarity when decomposing the signals. The extracted IMFs are components containing the information originating from some phenomena rather than a predefined frequency range, meaning that each component contains the whole spectrum of frequencies corresponding to that same phenomenon. For each IMF, the Power Spectral Density (PSD) was calculated. It is true that PSD assumes stationarity, but in our approach, we do not use it for the filtration procedure. In this method, the PSD is used to select the components that should be removed, thus allowing for the usage of a band-based filtering logic while avoiding the stationarity assumption in the filtration procedure itself. The absolute PSD is filtered using Median Filter with a window size of $2N$ to reduce the effects of narrow spectrum subcomponents on the calculation. The energy of the resulted function is then calculated using a running window integration with a window size of $2N$. The resulting Spectral Energy Distribution (SED) function is then used to decide if the component should remain, or if it should be removed from the signal. Similarly to SBF, the Low Pass, Band Pass, Band Stop and High Pass filters can be defined. We used an Intrinsic Component Low Pass Filter (IC-LPF) at 0.1Hz. The components in which the area of the SED for frequencies above 0.1Hz (colored parts of Figure 13, panel (c)) being greater than the area below 0.1Hz (uncolored parts of panel (c)), are removed from the signal entirely. The IMFs with SED's maximal value above 0.1Hz are also removed [Figure 13].

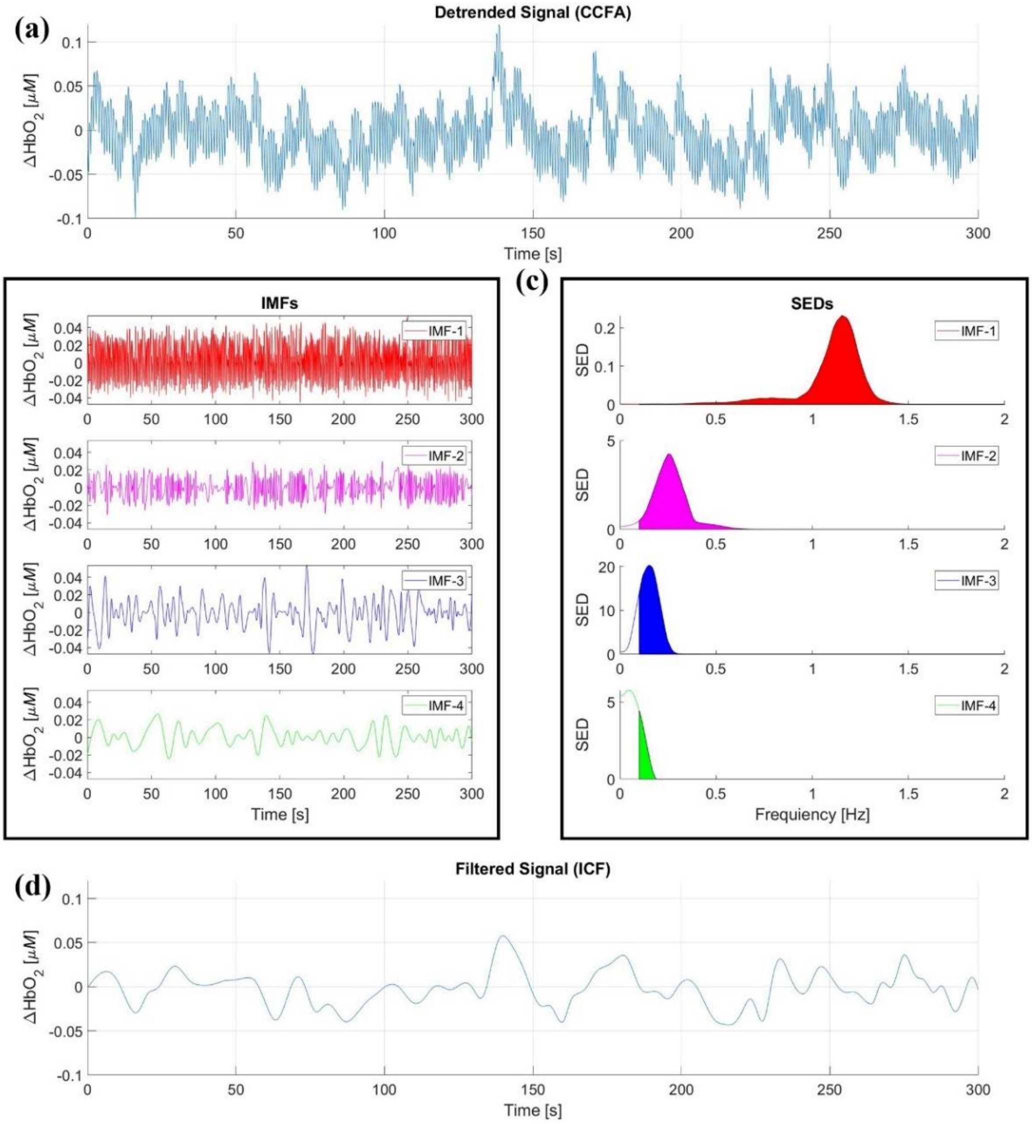

Figure 13. Panel (a) shows the detrended signal using CCFA. Panel (b) shows the first four IMFs of the signal shown in panel (a). Panel (c) shows the SED functions of the first four IMFs expanded to the range of 0~2Hz. The colored areas of the graph correspond to the frequency range of IC-LPF (above 0.1Hz). Panel (d) shows the filtered signal using the ICF approach based on all the remaining IMFs derived from that signal.

The filtered signal is then reconstructed by simply summing the remaining components (i.e. after removing the upper three IMFs shown in panel (b) of Figure 13. Since the filtering itself removes the entire component, this technique is suitable for non-stationary signals. ICF can also be done directly from the PSD rather than the SED. Using the PSD will be more sensitive to short frequency spectrum subcomponents of the IMF. Note that in case of the PSD, the removal must be based only on the ratio of the areas and not on the maximal frequency-value due to high sensitivity to the short frequency spectrums. The detrending procedure should be performed prior to the ICF step.

fNIRS: Data Simulation for Filtration Assessment

For the effectiveness evaluation a synthetic dataset was constructed in the following way: The Hemodynamic Response Function (HRF) was defined in accordance with [92] using the Gamma Function described by equation 14 in section 3.2.2. According to Santosa H. et.al. [92], the HRF peaks at 6-8 seconds following the stimulation. Therefore, the parameters were set to create a HRF with a peak at 7s and $b_1 = 1\left[\frac{1}{s}\right]$. Next, using Dirac comb approach, Hemodynamic Response Trial (HRT) was simulated:

$$HRT = HRF * \sum_{i=0}^{r} \tau_i \cdot \delta(t - T \cdot i)$$

$$\delta(j) = \begin{cases} 1, & j = 0 \\ 0, & elsewhere \end{cases}$$

Where $*$ is a convolution operator, $\delta(\cdot)$ is Kronecker delta function, r is the number of desired HRF occurrences in the constructed signal, T is HRF occurrence rate, $\tau_i \in \{0,1\}$ and t is the time stamp in seconds. In our setting, the parameters were as follows: at random, four of the τ_i values were set to 0 while others are equal to 1, $r = 14$ and $T = 20[s]$. The signals for testing were then defined as in [86], however, the amplitude multipliers were chosen based on [93]:

$$\check{S}_\chi = \tilde{S}_\chi + A \cdot HRT$$

$$\begin{cases} \{A_1, \dots, A_5\} = \{0.05, 0.08, 0.1, 0.2, 0.3\} & [for \ \mathrm{HbO_2}] \\ \{A_1, \dots, A_5\} = \left(-\frac{1}{3}\right) \cdot \{0.05, 0.08, 0.1, 0.2, 0.3\} & [for \ \mathrm{HbR}] \end{cases}$$

$$A \in \{A_1, \dots, A_5\}$$

Where $\check{S}_\chi$ is the synthesized, raw fNIRS signal with HRF occurrences, $\tilde{S}_\chi$ is a raw signal recorded during the resting state phase of the study and $\chi = 1, \dots, \mathrm{X}$ is an index numbering the signals. An amplitude multiplier A was defined taking into consideration the HRF values described in [93]. The results of [93] indicate that the amplitude of the HRF has a significant variability, thus the above multipliers were chosen to assess the performance for different amplitudes of the HRF that may appear in the real data. The limits, however, were chosen based on our resting state data and GLM approximation limitations.

When testing GLM using random HRF locations on a resting state signal, we concluded that the error margin of the method is around 0.02, thus the smallest multiplier was set to be 0.05 for HbO_2. On the other end of the range, we know that the SNR of those signals cannot be above 0dB if calculated as defined in this work. This is due to the fact that HRF cannot have a higher amplitude than the recorded signal itself, which should also contain random HRF occurrences. The multiplier of 0.3 on average, provided a borderline amplitude that led to a SNR close to 0dB, thus it was chosen as an upper range limit. Note that in [86] the HRF is convolved with a functional block, whereas we chose an instantaneous HRF. This is due to the fact that our cognitive task involves instantaneous actions that will be analyzed in future publications. Let $\breve{S}_{\chi}^{(A_i)}$ be a signal with an amplitude multiplier $A = A_i, i \in \{1, \dots, 5\}$. Every signal was then filtered twice independently; Once using the DCT and SBF methods and once using the CCFA and ICF methods. This was done for each of the amplitude multipliers. The SBF was defined as a Finite Impulse Response (FIR) LPF of 500th order with a cutoff at 0.1Hz (the same as IC-LPF). The signal resulting from DCT and SBF filtration is defined as $\ddot{S}$ and the one resulting from CCFA and ICF filtration as $\dddot{S}$.

fNIRS: General Linear Model Procedure:

Using the GLM model:

$$Y = XB + \epsilon$$

Where Y is the filtered signal ($\ddot{S}\ or\ \dddot{S}$), X is a matrix with first column containing ones and the second column containing the product $A \cdot HRT$, B is the regression coefficients vector and ϵ is the error vector. Once the values of B were estimated, $B(1)$ contains offset coefficient and $B(2)$ contains amplitude gain factor resulting from the filtration process. We denote $\beta_{\chi} = B(2)$ calculated for signal number χ. A high-quality filtration process should remove the noise sources, without affecting the HRT. Therefore, we calculated the relative change in the values of the β coefficients, in relation to the A coefficients as proposed by Pinti et. al. in [86]. As expected, the post-filtration values of the β are always reduced due to the negative gain of the filtration procedures. For each of the filtration methods, the β reduction fraction was calculated following both the detrending step and the complete filtration. The calculation was done as follows:

$$\beta_{\rho} = \frac{100}{|A|} \left| A - \underset{\chi}{\mathrm{Per}_{\rho}}(\beta_{\chi}) \right| [\%]$$

Where Per_{ρ} is a function providing the percentile ρ and β_{ρ} is the reduction fraction of the percentile ρ. The β value fraction reduction was calculated for percentiles 25, 50 and 75.

fNIRS: Signal to Noise Ratio Procedure:

The SNR value, ζ_{χ} was calculated as the ratio of the summed squared magnitudes of the signal to the noise. The signal was defined as: $HRT \cdot \beta_{\chi}$ and the noise were defined as: $\ddot{S} - HRT \cdot \ddot{\beta}_{\chi}$ for DCT and SBF filtration and $\dddot{S} - HRT \cdot \dddot{\beta}_{\chi}$ for CCFA and ICF filtration method. Where $\dddot{\beta}_{\chi}$ is a β-value using CCFA and ICF method and $\ddot{\beta}_{\chi}$ is a β-value using DCT and SBF filtering method. The multiplication by β was done to exclude the effect of the negative gain produced by filtration, from the SNR assessment. It allows for the assessment of the dominance of the signal over the noise after the filtering procedure. Then, the percentiles 25, 50 and 75 were calculated for the SNR.

Results

CCFA Algorithm

CCFA algorithm is a general-purpose solution of filtering, resampling and approximating missing samples for nonlinear and non-stationary signals. The target process does not have to be temporal or quasi-periodic. In this work, CCFA was used for missing samples' approximation in gait analysis section and for filtration in brain research section. In both cases we present statistical evaluation of the method compared to the commonly used solutions, in their respective sections. Here we present some graphical examples of CCFA's performance and capabilities:

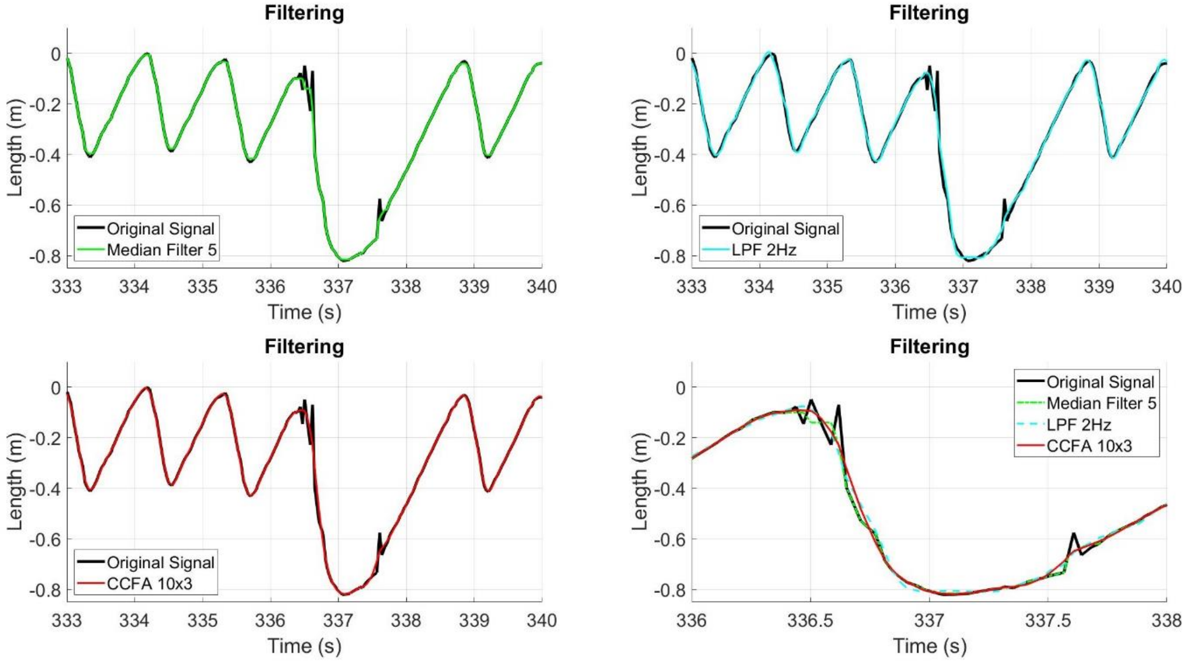

Figure 14. Black line is human gait signal containing some noise. Green line shows the result of median filter of 5th order. Light blue line is the result of LPF using cutoff frequency of 2Hz. Red line is the result of using polynomial based CCFA with k-order of 10 and polynomial degree of 3.

Figure 14 shows the comparison of non-Gaussian noise filtration using three different methods: median filter, LPF and CCFA. Although median filter reduces the noise, it fails to produce the smooth waveform that we expect to see in the noisy area. LPF on the other hand, produces a smooth waveform as one would expect to see in the noisy regions, but at the same time it creates many distortions along the entire signal. CCFA however, provides smooth waveform that seems to be the best result out of these three and at the same time produces almost no distortions of the data.

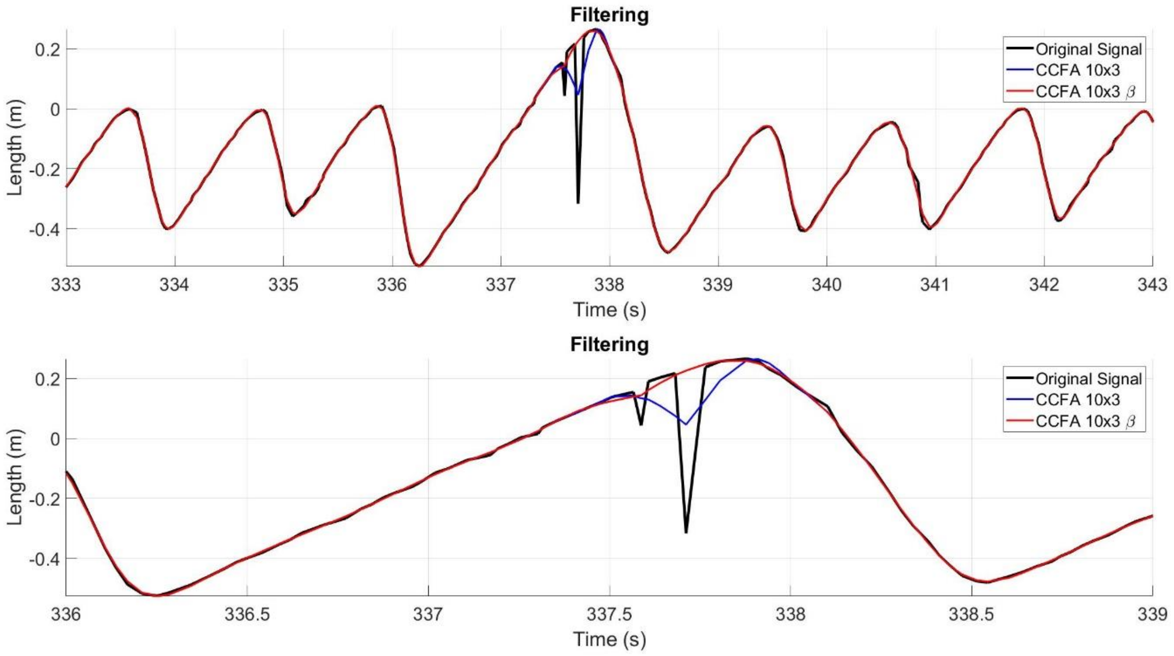

Figure 15. In black is human gait signal with a strong spiky noise. In blue is CCFA based filtering using polynomial curve fitting with k-order 10 and polynomial degree of 3. In red is CCFA based filtering using the same parameters as used for blue line, but with approximated β reliability weights.

As can be seen in Figure 15, strong non-Gaussian noise will affect the performance of CCFA. However, β reliability weights can be used to negate these effects. In the example above, the reliability weights were estimated using a simple derivative. The reliability of each sample in the signal was defined based on the derivative value at that point. High derivative means low reliability and vise-versa. We can see that once the estimated reliability weights were provided, the effect of high-amplitude spike was almost completely subdued.

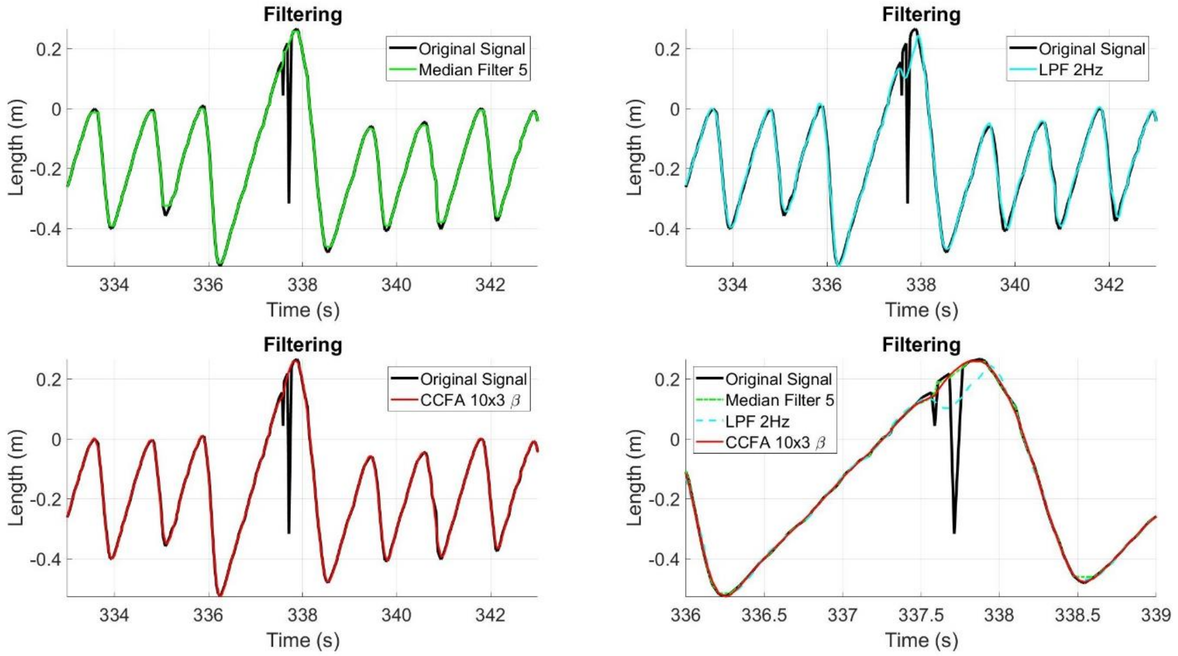

Figure 16. In black is the human gait signal with high-amplitude spike noise. Green is the filtration result using median filter of 5th order. In light blue is the result of LPF with a cutoff frequency of 2Hz. In red is the result using CCFA based on polynomial curve fitting with k-order of 10, polynomial degree of 3 and approximated β reliability weights.

Figure 16 shows the comparison between median filter, LPF and CCFA on the signal from Figure 15. As expected, median filter removes spiky noise very effectively, but at the same time distorts the signal in the local extrema locations. LPF fails to remove the high-amplitude spike and creates distortions along the entire signal. CCFA on the other hand, removes the noise and preserves the original function quite well.

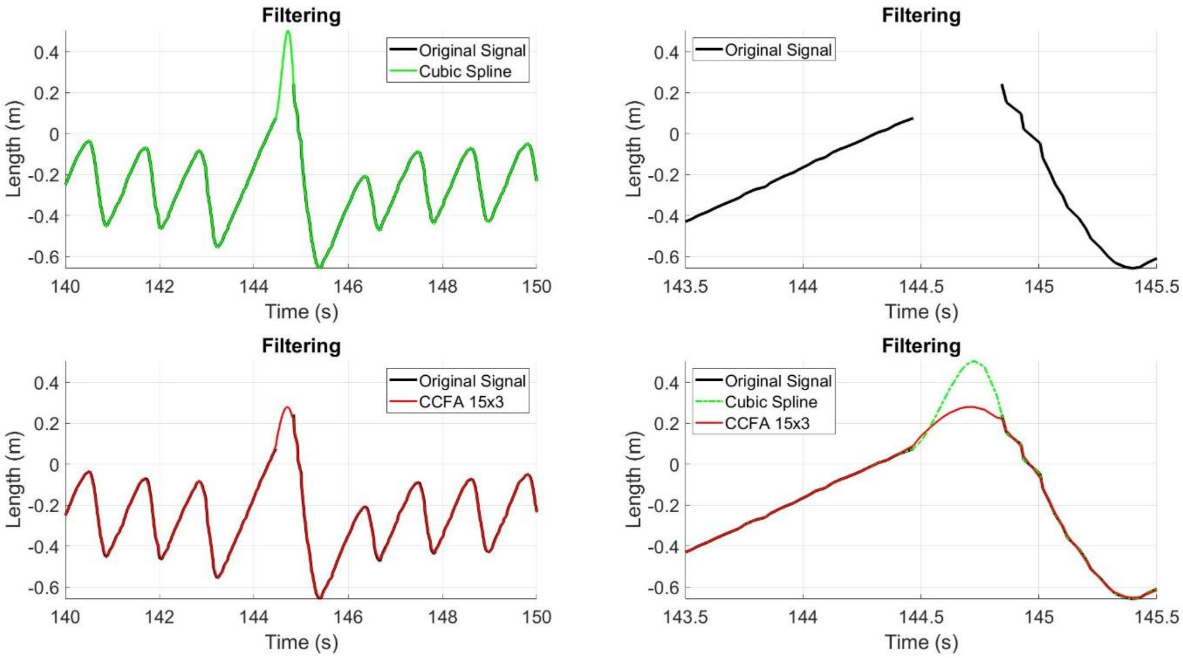

Figure 17. In black is the human gait signal with a missing section. In green is the cubic spline interpolation-based reconstruction of the section. In red is polynomial based CCFA using k-order of 15 and polynomial degree of 3.

When examining the reconstruction using cubic spline [Figure 17], we can see a severe "overshoot" in the reconstructed area. This is probably due to small noise near the borders of the missing section that distort the direction of the samples at the edge. Since CCFA is not sensitive to noise, this distortion does not affect its reconstruction curve, thus providing a much more reliable result.

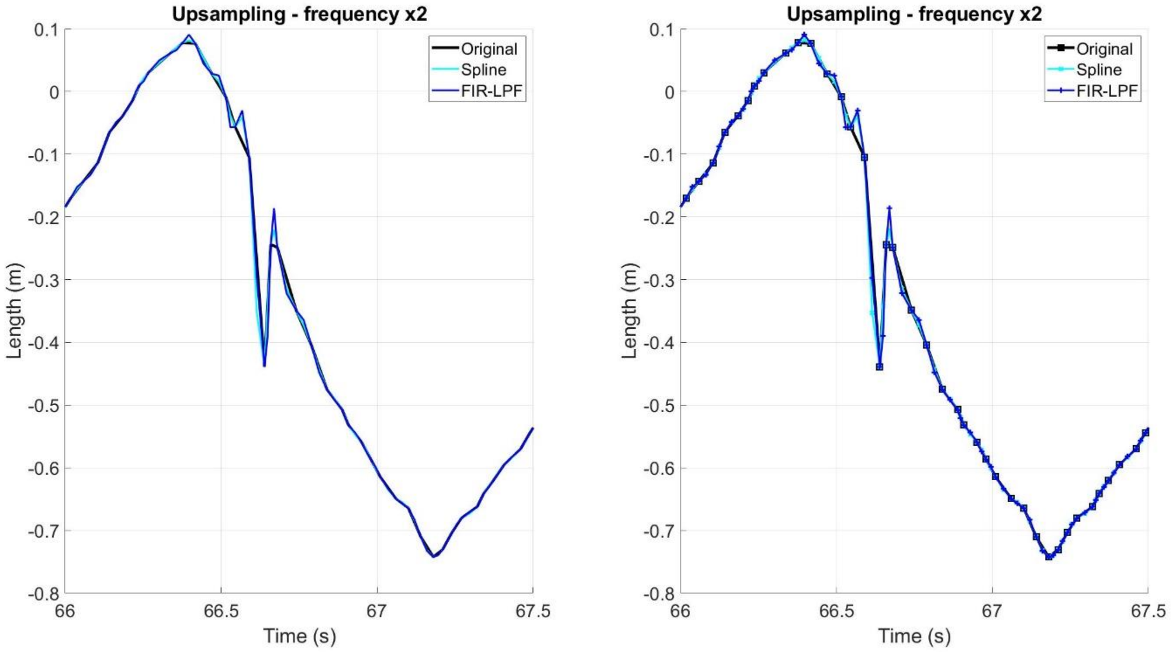

Figure 18. Black is the human gait signal. In light blue is the result of up-sampling of the signal using cubic spline. In dark blue is the result of up-sampling using Finite Impulse Response (FIR) LPF – anti-aliasing filter.

It is a known fact that any type of resampling produces additional noise. It can be clearly seen on both up-sampled signals [Figure 18], as new high-frequency noise were added to the existing noise sources.

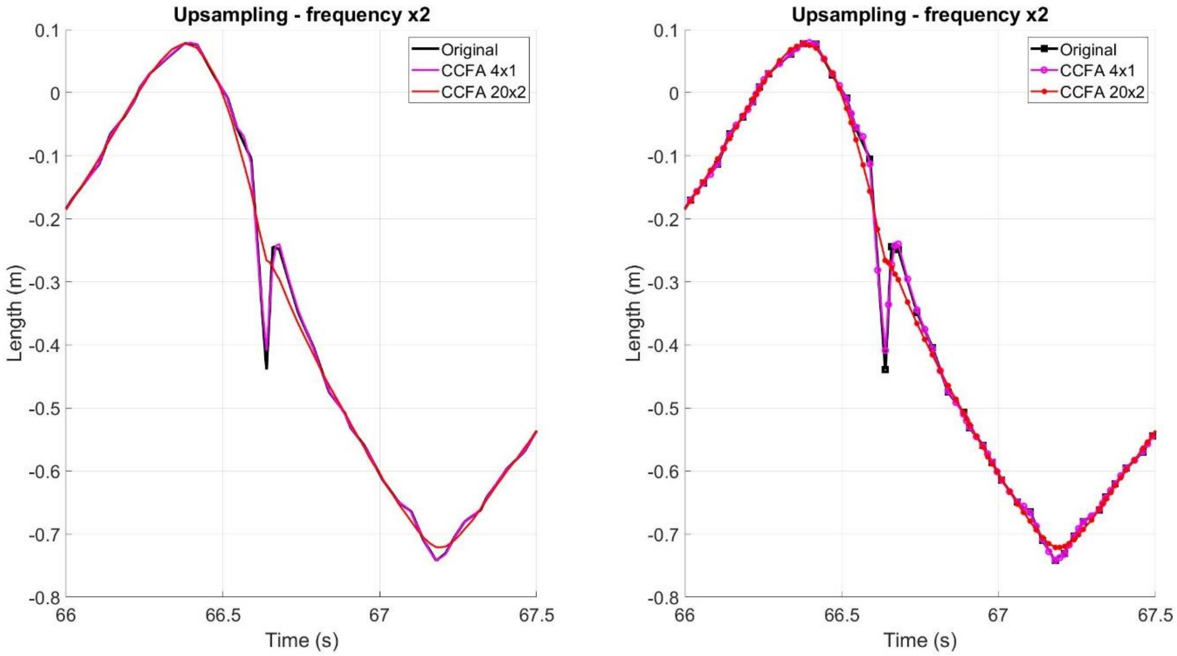

Figure 19. In black is human gait signal. In magenta is up-sampled signal using CCFA without noise reduction. In red is CCFA up-sampled signal using its noise reduction ability.

When using CCFA for resampling, the magnitude of the produced noise is quite small [Figure 19]. If we examine the up-sampled signal without noise reduction, that has a magenta color in Figure 19, we can see that the resulted signal follows the original one very closely and even slightly reducing the noise, while producing almost no high frequency noise that can be seen in methods used in Figure 18. In addition, CCFA is capable of reducing the noise while performing resampling of the signal. The example of up-sampling with noise reduction is shown in red in Figure 19, where we can see a significant reduction of the spike noise, even without the usage of approximated reliability weights. When resampling is performed with denoising, CCFA will not produce any high-frequency noise, but it will affect the shape of the signal according with the filtration settings as can be seen in the area of the local minima just after 67 seconds timestamp [Figure 19].

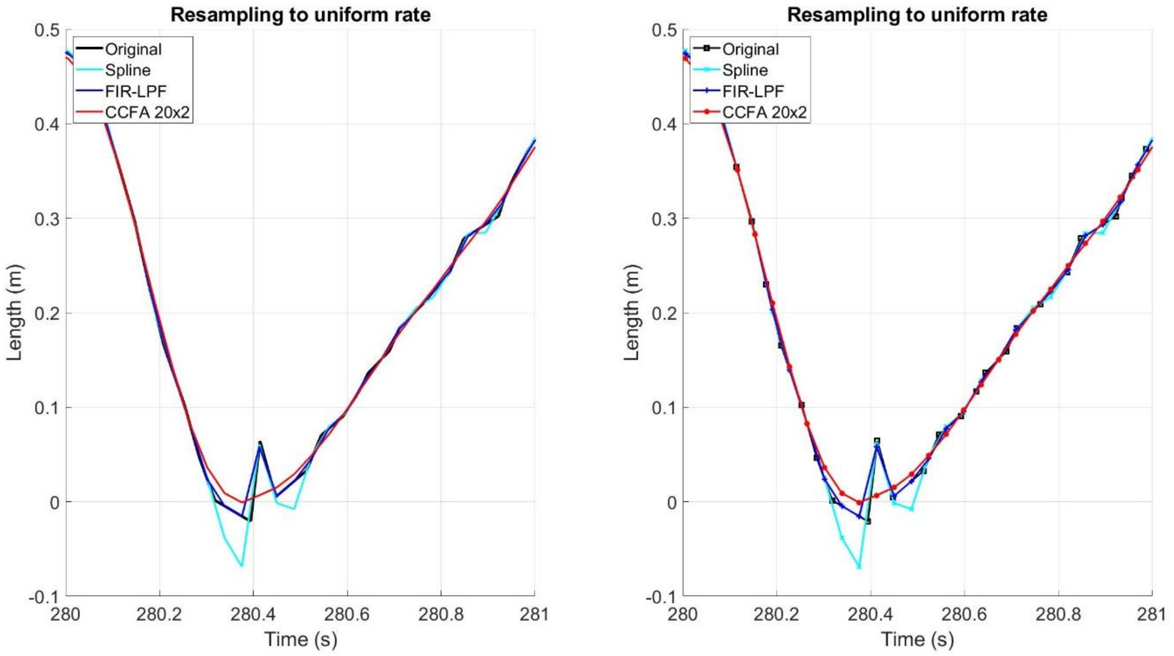

Figure 20. In black is human gait signal with non-uniform sampling rate. In light blue is resampling of the signal to uniform rate using cubic spline interpolations. In dark blue is resampling of the signal to uniform rate using FIR LPF – anti-aliasing filter. In red is resampling to uniform rate with noise reduction using polynomial CCFA.

In Figure 20 we can see a closeup of signal’s section resampled to uniform sampling rate using three different methods. It is evident that both cubic spline and FIR LPF produce high-frequency noise when resampling [Figure 18, Figure 20]. CCFA however, does not produce these noise and even reduces the effects of the existing noise in the resampled signal [Figure 19, Figure 20]. The small “undershoot” that can be seen in Figure 20, can also be reduced by providing the reliability weights to the algorithms.

Gait Analysis

Gait: SDET Peak Detection

Using SDET, all the local extremum points that were global within their period on the quasi-periodic temporal signal were estimated in [30]. Since there were no classified reference data (true extremum point locations), more than a hundred of different signals were inspected visually. Almost no miscalculated points were found other than the local extremum near the beginning and the end of the signal or in regions with severe data loss [Figure 21].

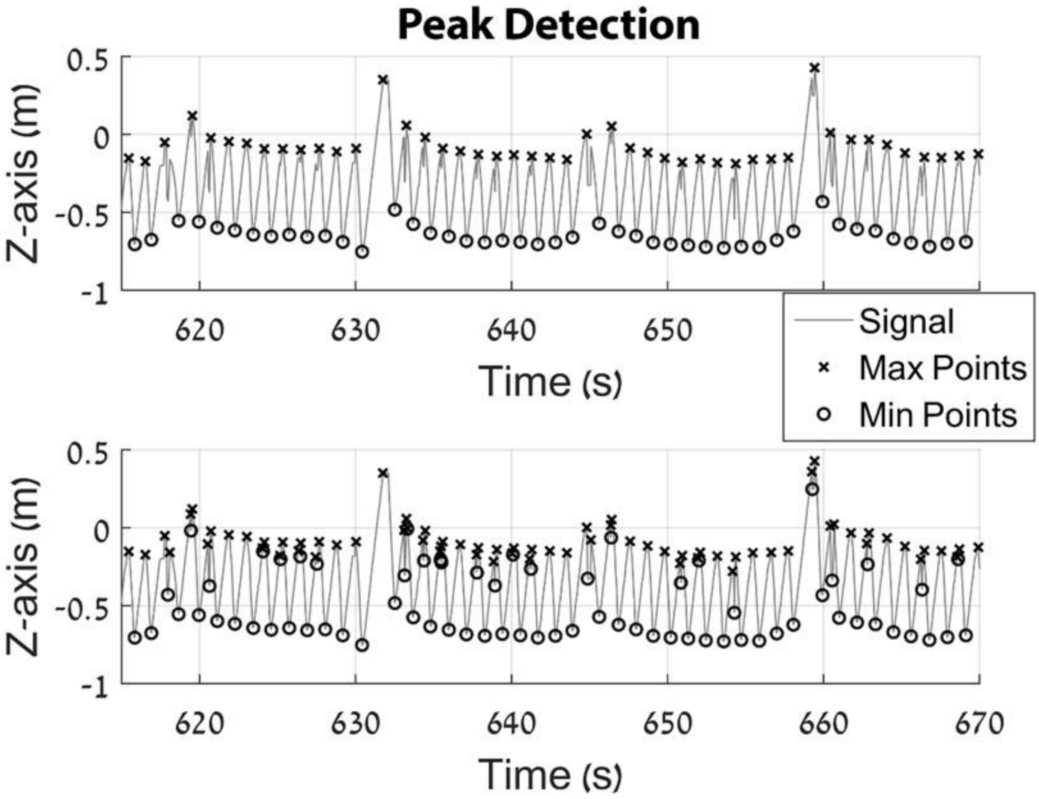

Figure 21. Peak detection using SDET on the gait signal. Lower panel shows the detection of all local extrema within the time section. The upper panel shows the detection of extrema points using the proposed method.

Gait: Detection of Gait Abnormalities

Using the proposed temporal segmentation, the segments corresponding to obstacle avoidance were detected. The kernel-based clustering allowed for the detection of the irregular steps. By combining the two solutions, we received the preparation phase for the obstacle avoidance, its recovery phase and the irregular steps within these phases [Figure 22]. The detection results were selectively inspected by the medical specialists and were confirmed to be reliable.

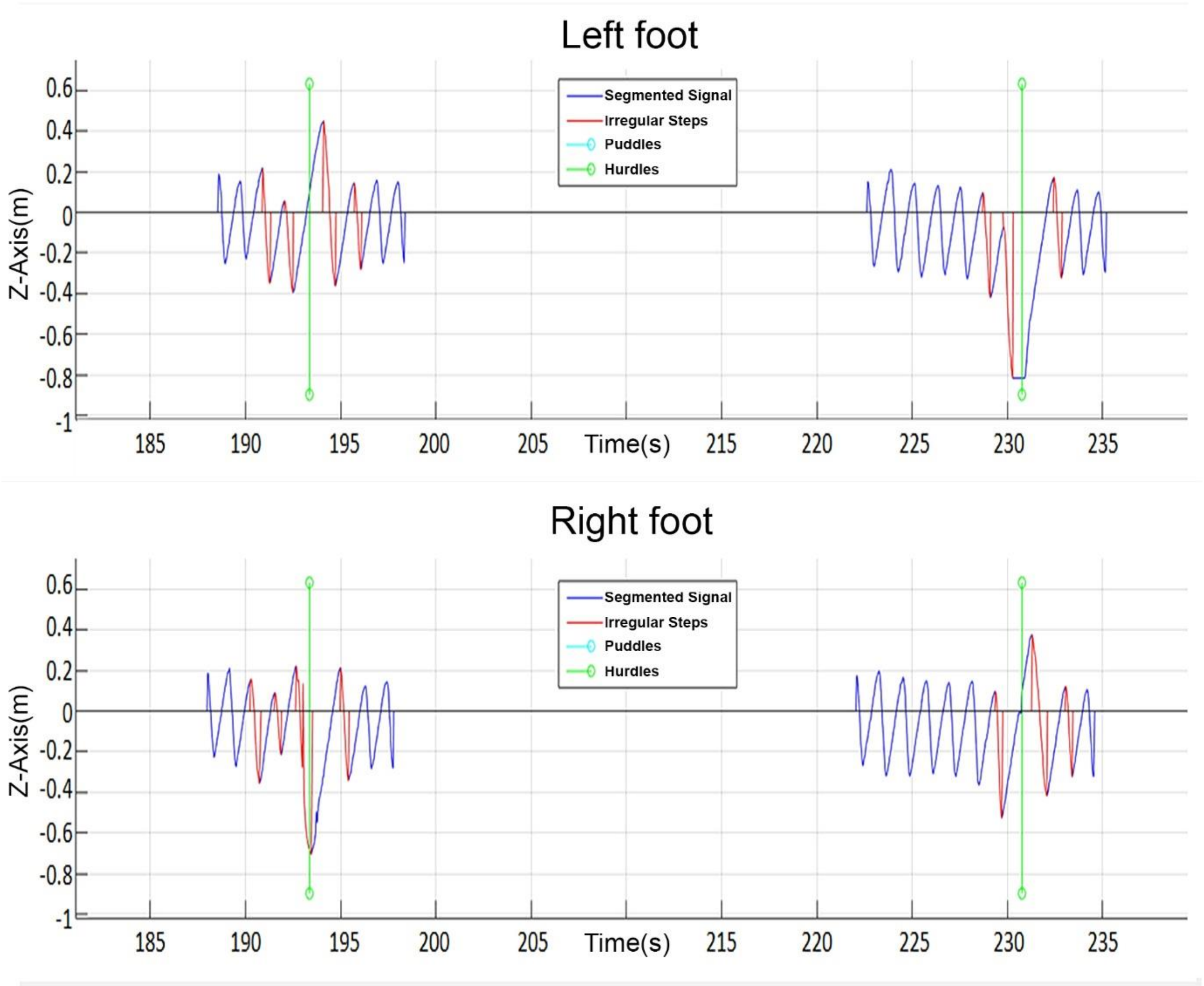

Figure 22. Segments related to obstacle avoidance task for each foot. Section before the obstacle is the preparation phase, section after the obstacle is the recovery phase. The abnormal steps are marked in red.

Gait: CCFA – Missing Samples Approximation

To examine the accuracy of the proposed CCFA model, it was compared to Linear Interpolation, Cubic Spline Interpolation and to back and forth Auto-Regressive fitting model. Almost 850,000 examples of signals with missing samples were used. These data were collected from 37 different gait trials done by 5 different subjects. The results were compared in terms of Root Mean Square Error (RMSE). CCFA was tested with a range of parameters for algorithm order k_{ord} and polynomial degree p_{ord} where: $1 < k \leq 50 \quad and \quad 1 \leq p \leq 5$ [Table 1].

Method	**RMSE**
Linear Interpolation	4.34 (cm)
Cubic Spline Interpolation	2.49 (cm)
Auto Regressive Model	2.42 (cm)
CCFA (Optimal k and p in range)	0.75 (cm)

Table 1. CCFA model performance comparison to other models when optimal parameters within the predefined range are used.

The proposed ML algorithm for CCFA parameters prediction was tested 30 times with different random seeds for data separation. This was done in order to roll out the possibility of favorable division of the data. The results are shown in [Table 2]:

CCFA using parameters k and p predicted by the ML model over 30 tests	**RMSE**
Maximum	1.25 (cm)
Minimum	1.24 (cm)
Mean	1.25 (cm)
Median	1.25 (cm)

Table 2. CCFA model performance using the input parameters predicted by the proposed ML algorithm.

Although the proposed ML algorithm did not yield the best possible results (see Table 1), it has still provided much better accuracy than that of Interpolations and the Auto-Regressive Model.

Gait: Walking Performance Analysis

Using the result from the proposed methods, gait performance of all participants was analyzed. Based on the result, it is evident that V-TIME system improves walking performance. One of the common issues among elderly is the reduced step length and walking speed. In Figure 23, it can be clearly seen that step length is increasing while step time is decreasing, indicating the improvement of the walking speed and overall performance.

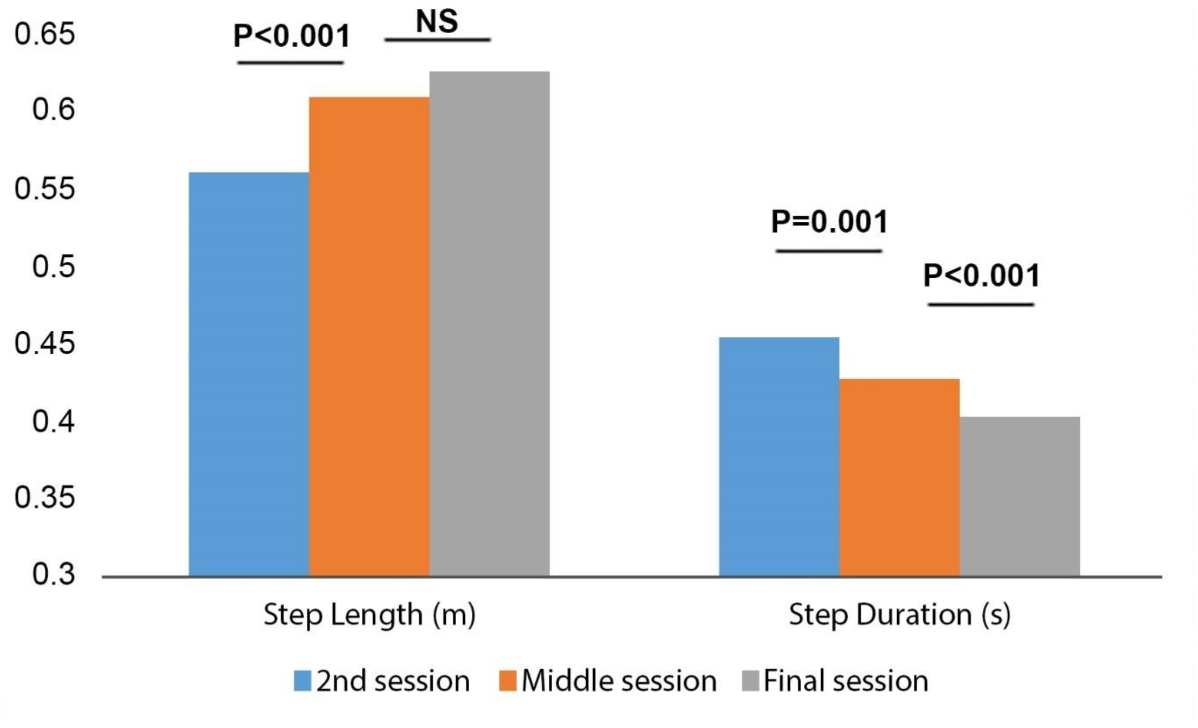

Figure 23. The bars show the average step length and duration from second session, middle session and final session of the training course. Significant improvement of the steps can be seen throughout the training course. The scale is in meters for length and in seconds for duration.

Gait and the Brain

EEG: Analysis

Using the procedures as described in the methods section, EEG data was processed and analyzed. SDET was able to accurately detect the peak locations of the neuronal activation patterns during gait dual task walking. Based on the detected peaks, APC provided comprehensive information regarding the differences of the brain activation patterns between different subject groups.

Assessment of the effects of aging and PD on cognitive performance during dual task walking [64].

The analysis showed that MOCA, gait speed, and CTT scores were significantly lower in patients with PD, compared to healthy young [Table 3].

Parameter	**Healthy young N=11**	**Elderly N=10**	**PD N=10**	**p-values**
Age (years)	32.3 ± 1.8	67.1 ± 1.7 *	60.5 ± 3.6 **	< 0.001
Gender(M/F)	7/6	4/6	6/4	0.853
Treadmill Gait Speed (m/s)	0.8 ± 0.02	0.6 ± 0.03	0.6 ± 0.02 **	0.015
MOCA	28.2 ± 0.4	27.7 ± 0.5	25.2 ± 0.8 ** #	0.003
CTT (s)	32.2 ± 4.2	51.8 ± 3.4	67.9 ± 14.7 **	0.014
Disease Duration (years)	N/A	N/A	2.9 ± 0.5	N/A
UPDRS Motor	N/A	N/A	20.2 ± 3.4	N/A
LEDD (mg)	N/A	N/A	303 ± 114	N/A

Table 3. Participants' characteristics. PD - Parkinson's disease, M - Male, F - Female, MOCA - Montreal Cognitive Assessment, CTT - Color Trail Test, UPDRS - Unified Parkinson Disease Rating Scale, LEDD - Levodopa Equivalent Daily Dose. * - Significant difference between healthy elderly and young. ** - Significant difference between PD and young. # - Significant difference between PD and elderly.

All participants were engaged in the oddball task and demonstrated high accuracy of performance during standing (healthy young 100 ± 0.0%, healthy older adults 98 ± 1.7%, and patients with PD 97.4 ± 1.1%) and during walking (healthy young 99.2 ± 0.4%, healthy older adults 99.4 ± 0.4%, and patients with PD 99.4 ± 0.4%). The P300 potentials of 1 healthy older adult and two patients with PD could not be achieved. Therefore, the data of these three subjects were not included in the analysis. Table 4 summarizes the P300 latency and amplitude during standing and walking.

Condition	Standing				Walking			
Variable	Subject (n)	Latency (ms)	Amplitude (mamp)	Achieved P300 (%)	Subject (n)	Latency (ms)	Amplitude (mamp)	Achieved P300 (%)
Young	11	396 ± 29	7.1 ± 1.6	91.7	11	415 ± 23	7.7 ± 1.0	75
Elderly	9	456 ± 32	6.9 ± 0.9	80	9	526 ± 27	7.3 ± 0.7	70
PD	8	478 ± 13	6.2 ± 0.9	70	8	558 ± 33	3.8 ± 0.6	50

Table 4. P300 latency and amplitude during each condition in each group.

Analysis of differences between conditions (i.e. standing and walking) showed prolonged P300 latency during walking compared to standing in all groups (p = 0.005), while P300 amplitude was similar between conditions (p = 0.528). Similar results were observed after controlling for LEDD (latency: p = 0.014, amplitude: p = 0.687) or MOCA (latency: p = 0.012, amplitude: p = 0.687). P300 latency during walking was significantly shorter in the healthy young subjects compared to the healthy older adults (p = 0.032) and to the patients with PD (p = 0.005). No differences were observed between the healthy older adults and the patients with PD in this condition (p = 0.976). Between group differences in P300 latency during standing were only observed between healthy young and patients with PD (p = 0.041). A significant condition by group interaction was found for P300 amplitude (p = 0.008). Similar amplitude between standing and walking was shown in healthy individuals (both healthy young and healthy older adults) and a smaller P300 amplitude during walking (compared to standing) was demonstrated in patients with PD (p = 0.023, Figure 24).

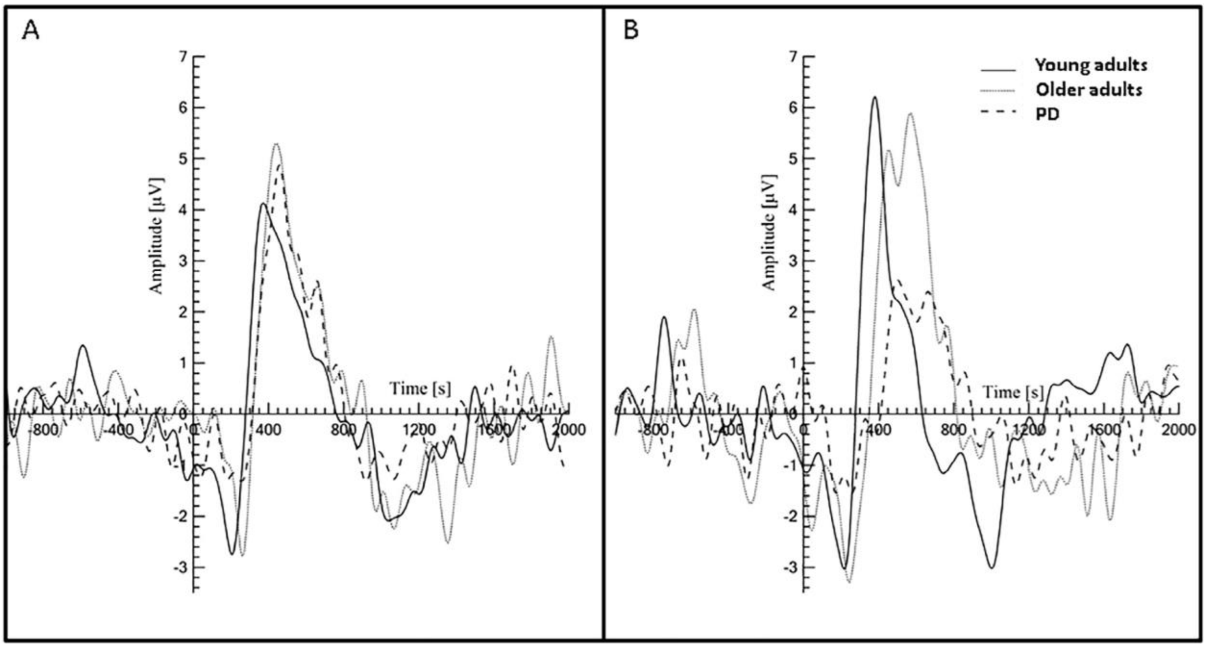

Figure 24. P300 during (A) standing and (B) walking in young adults, elderly, and patients with PD. No differences in P300 latency and amplitude are observed between the groups during standing. In contrast, P300 amplitude is significantly lower in patients with PD (dash line) compared to young and elderly during walking (p = 0.023).

Young healthy adults showed higher stride (p = 0.037) and step regularity (p = 0.050) compared to patients with PD during oddball walking. Trend toward significant was observed during usual walking (stride regularity p = 0.072, step regularity (p = 0.071). No differences in dual task cost between the groups were observed (dual task cost stride time p = 0.616, DT-cost stride regularity p = 0.971, DT-cost step regularity p = 0.295). Gait speed was significantly lower in patients with PD (p = 0.018) [Table 3].

P300 latency was inversely correlated to gait speed (r = -0.457, p = 0.014) in all participants indicating that lower gait speed (worse motor ability) was associated with prolongation of P300. In addition, a significant correlation was found between CTT and P300 latency. P300 amplitude was not associated with cognitive or gait measures.

Assessment of gait related potential [31].

Walking speed on the treadmill during both usual and oddball walking was lower in the older adults compared to young adults (p=0.030). Among all subjects (no effect of group), compared to usual walking, stride time (task effect: p=0.009, group effect: p=0.068) and stride time variability (task effect: p=0.021, group effect: p=0.488) were lower during oddball walking [Table 5].

	Stride Time mean (s)		Stride Time CV (%)	
Task (mean ± SE)	Usual Walk	Oddball Walk	Usual Walk	Oddball Walk
Young	1.39 ± 0.04	1.38 ± 0.04	2.47 ± 0.23	2.53 ± 0.24
Elderly	1.36 ± 0.04	1.33 ± 0.04	2.79 ± 0.28	2.36 ± 0.11
Task Effect (p-value)	0.009		0.021	

Table 5. Gait measurements during usual and dual task in young and elderly.

In Figure 25 we can see that the electrical brain pattern during a gait cycle consisted of two main positive GRPs, P1 during the stance phase and P2 during the swing phase. The graph shows three channels, Pz, Cz and Fz comparing young and elderly subjects during usual walk and an oddball task. At the bottom of Figure 25, human gait cycle phases are synchronized with the timeline of the GRPs. Stance and swing phases can be seen at 30% and 75% of the gait cycle.

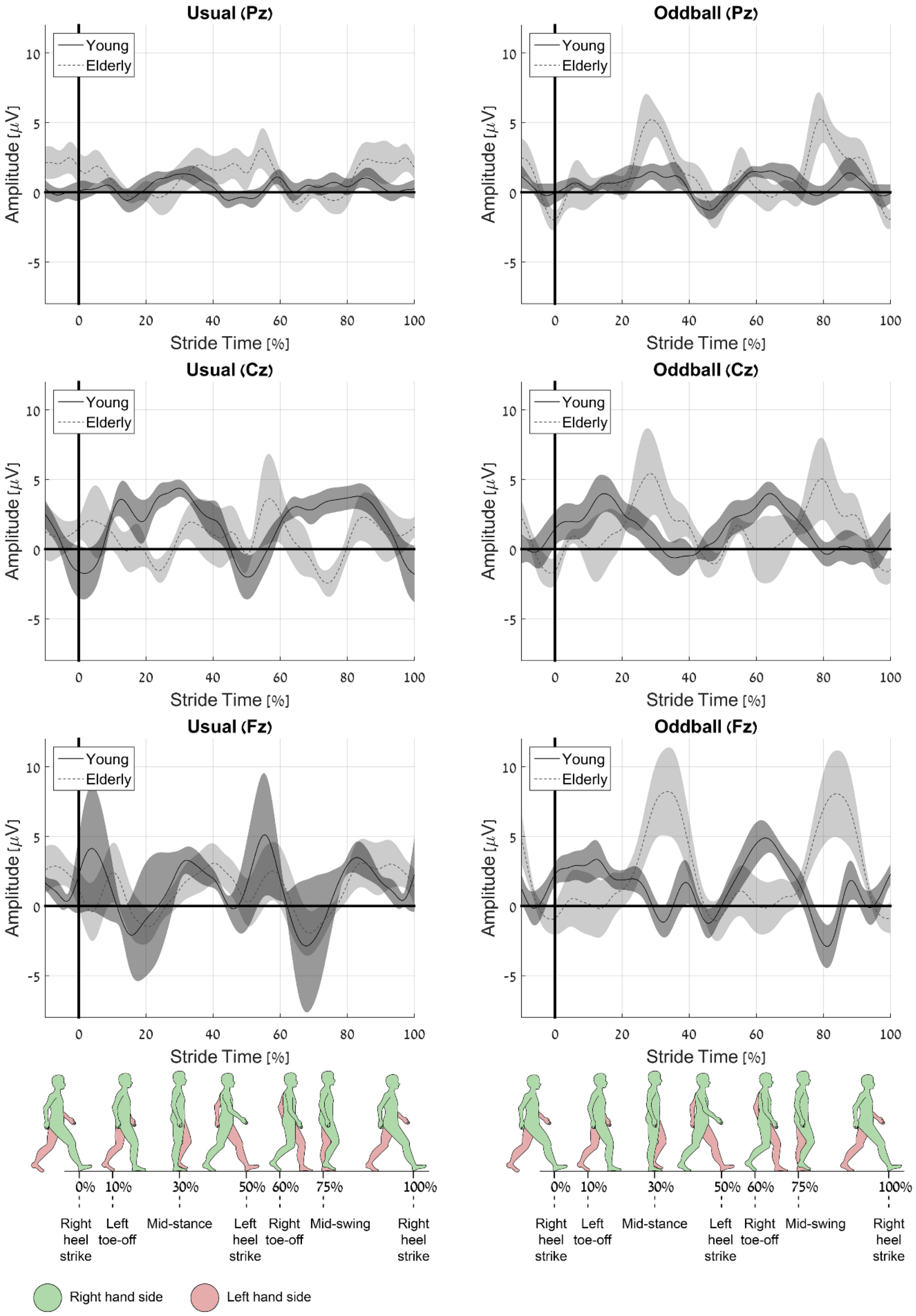

Figure 25. The grand mean of gait related potentials (GRP) within a gait cycle during usual and oddball walking in young and elderly in Pz, Cz, and Fz.

These GRPs differed between young and older adults in Pz by amplitude and in Cz by APC. In Pz, the older adults had higher peak amplitudes compared to the young adults (P1: p=0.006, P2: p=0.010) [Figure 26]. In Cz, the older adults had lower APC values than in the young adults (p=0.025).

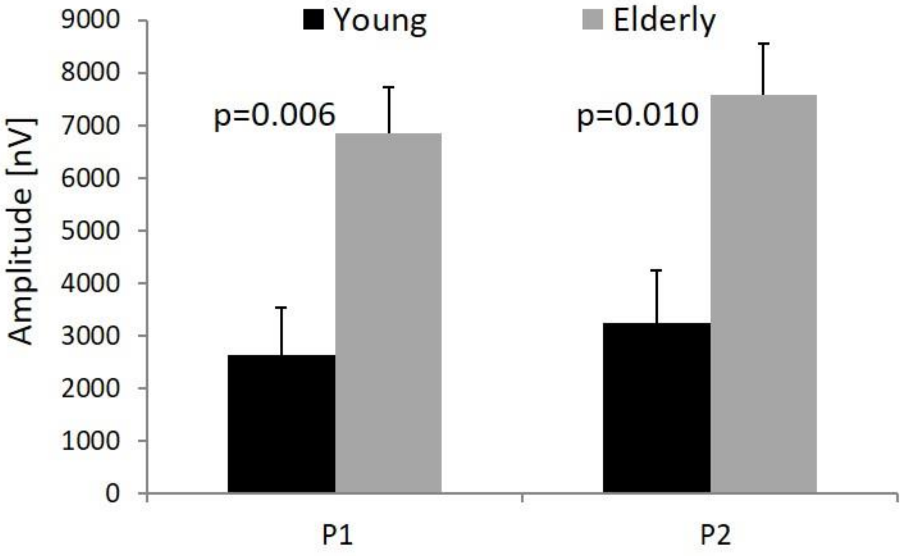

Figure 26. The differences in amplitude's peak between young and elderly in Pz. Average and standard error.

Comparison between usual and oddball walking tasks revealed significant differences in peak latency in Cz and Fz among all subjects. More specifically, in Cz, both groups showed shorter latency in oddball walking compared to usual walking (task effect: p=0.040), while in Fz the young adults presented shorter latency and older adults longer latency during oddball walking (interaction effect, p=0.045). In addition, significant differences in APC were found in Cz. While the young adults showed lower APC during oddball walking compared to usual walking, the older adults demonstrated the opposite effect, i.e. higher APC during oddball walking compared to usual walking (group X task interaction: p=0.006) [Figure 27].

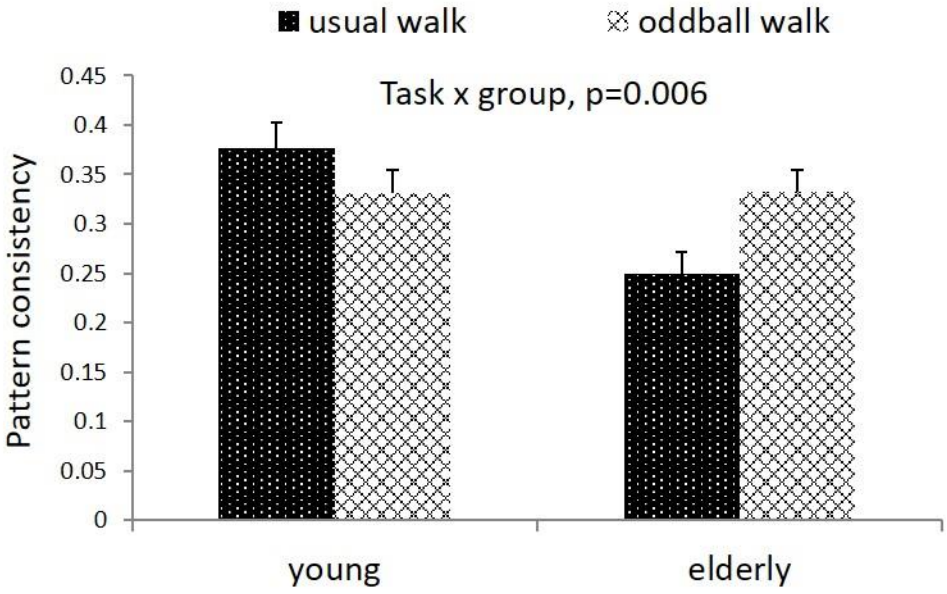

Figure 27. The differences in Amplitude Pattern Consistency (APC) between and within young and elderly in Cz.

Changes in auditory ERPs (e.g., P300) were previously published, showing direct evidence of physiological recruitment of attentional networks during walking and their impact by aging and disease [64]. Interestingly, the addition of the auditory events during the oddball task did not affect the GRPs. No differences were found in GRPs amplitude (p > 0.097), peak latency (p > 0.154), or APC (p < 0.132) between gait cycles in which the oddball sounds were displayed in the first half (stance phase) and gait cycles in which the oddball sounds were displayed in the second half (swing phase) [Figure 28].

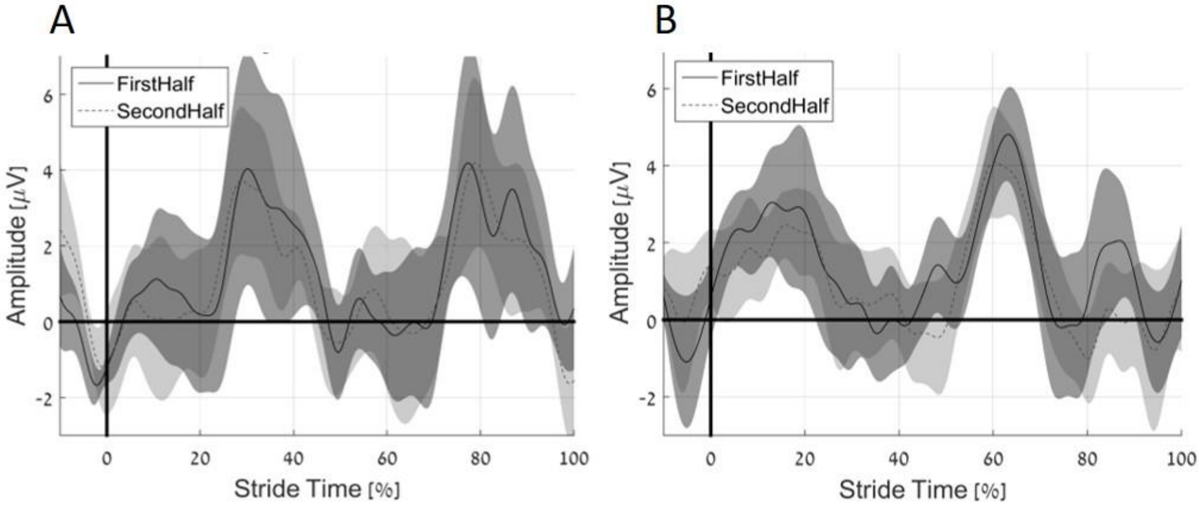

Figure 28. The electrical brain pattern of gait cycles in which the oddball sounds were heard at the first half and gait cycles in which the oddball sounds were heard at the second half in (A) older adults and (B) young adults in channel Cz.

Gait speed was correlated with APC (r=0.599, p=0.011) in all subjects. Specifically, a higher gait speed on the treadmill was correlated with a higher APC in Cz [Figure 29A]. In addition, stride time variability was negatively correlated with APC in Cz only in the older adults (r=−0.703, p=0.023). Older adults with higher stride time variability (worse gait performance) demonstrated lower APC [Figure 29B]. No correlations between gait measures, MOCA, and GRPs amplitude and latency were found (p > 0.050).

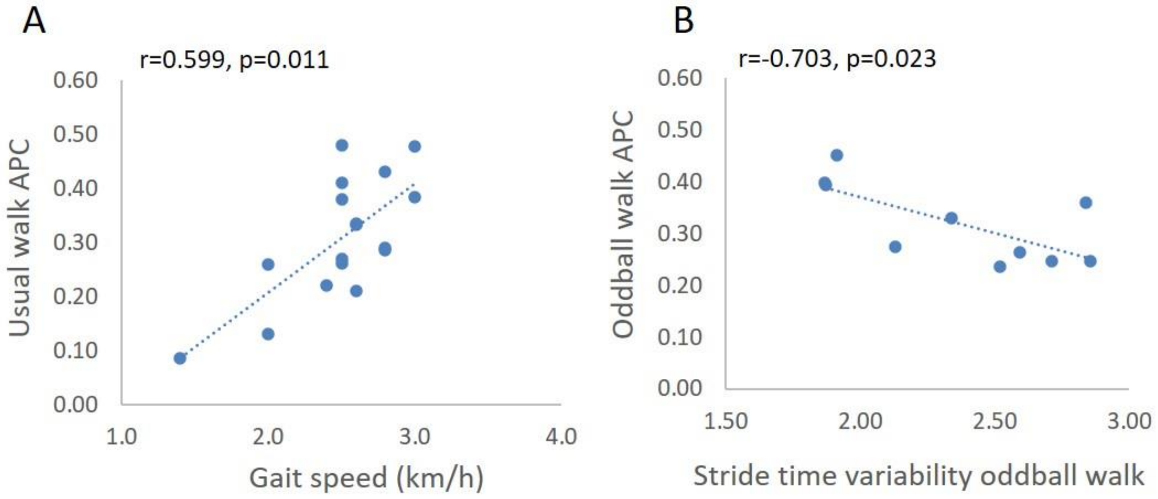

Figure 29. Correlations between: (A) gait speed and APC during usual walking in all subjects, and (B) stride time variability and APC during oddball walking in elderly.

Brain Research

fNIRS: MVE

The validation of the method was done by visually inspecting the signals, which is currently the most commonly used method of detecting such faulty channels. Three independent researchers inspected each of the 24 recorded channels from 22 different subjects, in total: 528 signals. Every signal received a label: Clean, Borderline or Noisy channel. Clean channels are those that have a clearly visible heartbeat on the raw signals. Borderline channels are those that have a heart beat visible only after removing the high frequency noise (above 1.6Hz). Noisy channels are those that have no visible heartbeat even after the removal of the high frequency noise. An entire session of a resting state block followed by three blocks of a cognitive task was collected in one continuous recording, when subjects were allowed to move a little in between the blocks. Each block was processed independently, therefore, the resulting number of labeled signals was 2112 (528 signals X 4 blocks). The MVE algorithm was then applied to every block in order to classify the 24 channels of that block as clean channels or NCs. The results of the classification were then compared to the labels provided by the researchers. Table 6 summarizes the classification, where the columns represent the reviewers' labeling and the rows the MVE algorithm's classification. Channels that were labeled as Borderline are hard to classify even for an expert, thus we have no solid conclusions whether these channels should be considered usable for further assessment or not. Therefore, we excluded the Borderline channels from the accuracy calculations.

Label	Clean channels	Borderline channels	Noisy channels
MVE Detected as Clean	1614	216	43
MVE Detected as NCs	19	65	155

Table 6. The number of signals classified using the MVE algorithm, as either clean or NC, for each label type provided by the experts.

Based on the remaining signals, the MVE's sensitivity is 98.84%, specificity is 78.28% and classification accuracy is 96.61%. Following, all channels that were not classified as NCs by the algorithm were used for assessment of motion artifacts and noise removal. MVE's performance in respect to sensitivity and specificity can be adjusted to the needs of the specific research by increasing or decreasing the skewness threshold that is set to 1 by default. The default value of 1 was theoretically concluded, but in cases where sensitivity or specificity is preferred over the other, it may be reduced to improve specificity or increased to improve sensitivity.

fNIRS: CSV

Using CSV algorithm, we were able to automatically detect artifact occurrences within the recorded signals, as shown in Figure 30.

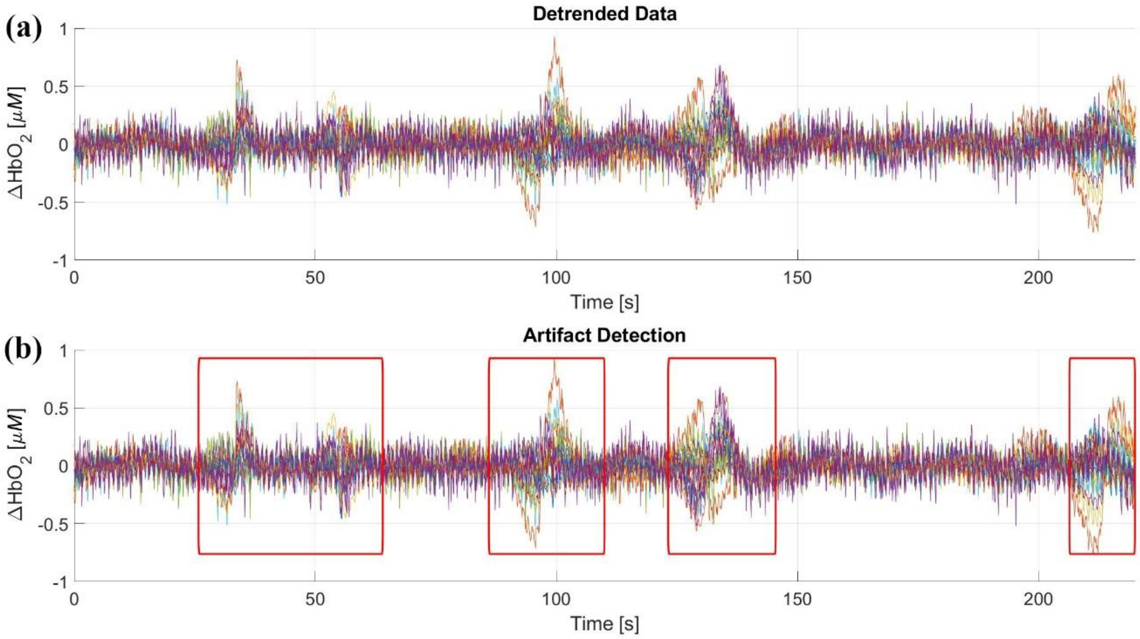

Figure 30. Output of the CSV algorithm. Panels (a)&(b) show the detrended signals. The red rectangles in panel (b) show the segments detected as motion artifacts.

The validation of the method was done by visually inspecting the signals, and grading the quality of detection by the experts, which is a common method for validating motion artifact detection in real-life data. In a follow-up publication we will describe the use of this method for targeted artifact removal. To validate our approach, we performed a visual inspection of the detection output. Each session was observed and evaluated in terms of accuracy of artifact detection by two independent research members. The given score was between zero and ten where zero represents an extremely poor detection and ten represents a perfect detection of the artifacts (under the subjective decision of the researcher). The mean score for the above-mentioned thresholds was 9.22 with a standard deviation of 1.13, indicating a reasonably high accuracy of detection with a low variability.

fNIRS: Artifact Detection

Using the proposed approach, we were able to detect spike artifacts that occurred in a single channel and include the affected area into the detection frame as can be seen in Figure 31.

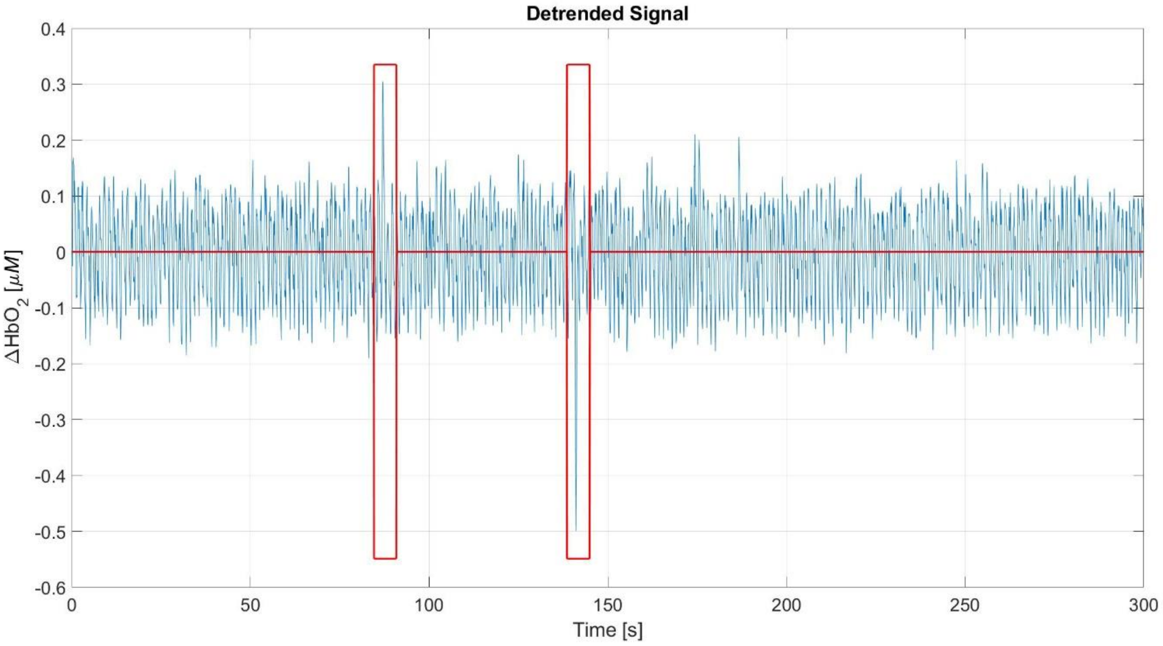

Figure 31. Red line presents spike artifact detection using the proposed procedure.

Motion artifacts that produce spikes usually affect multiple channels thus allowing for their detection using the CSV algorithm. The spikes appearing on a single channel or only on a few of the channels are not detected by the CSV algorithm as they are not its designated targets. On the other hand, the spike detection procedure, though capable of accurately detecting the spike artifacts, often fails to detect less sudden artifacts with a longer duration that are common in cases of motion artifacts. Thus, the CSV algorithm and the spike detection complement each other and allow for the detection of almost all types of the artifacts. Figure 32 presents an artifact detection map that can be constructed to assess the quality of the data.

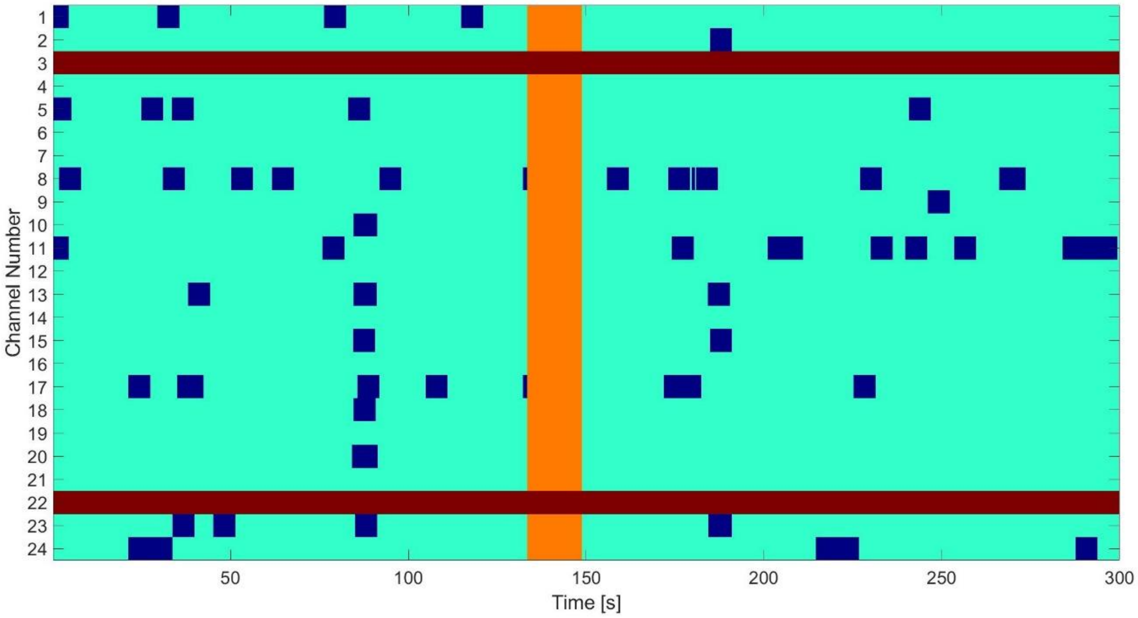

Figure 32. Artifact detection map for all channels (rows): Spike regions in dark blue, motion artifact regions detected by the CSV algorithm in orange and NCs (channels 3 and 22) detected by the MVE algorithm in dark red.

fNIRS: CCFA Detrending

Using the CCFA algorithm, with $k_{ord} = 4N$ for artifact detection purposes and $k_{ord} = 45N$ for data filtering ($N = 2.5sec$), we removed the time dependent first statistical moment (i.e. trend). We compare our method to the DCT based approach. To better understand the limitations, two different filtrations were done using DCT; One was the filtration proposed in the SPM toolbox [81], using the default suggested parameter (128 seconds). The other was a suppression of the first 17 coefficients of DCT using an exponential function. The 17th coefficient and all of the following ones are unchanged, while the first sixteen ones are suppressed in an increasing manner from 16th to the 1st coefficient, using an exponential function with a power in range of 0 and -20, equally spaced between the 17 components.

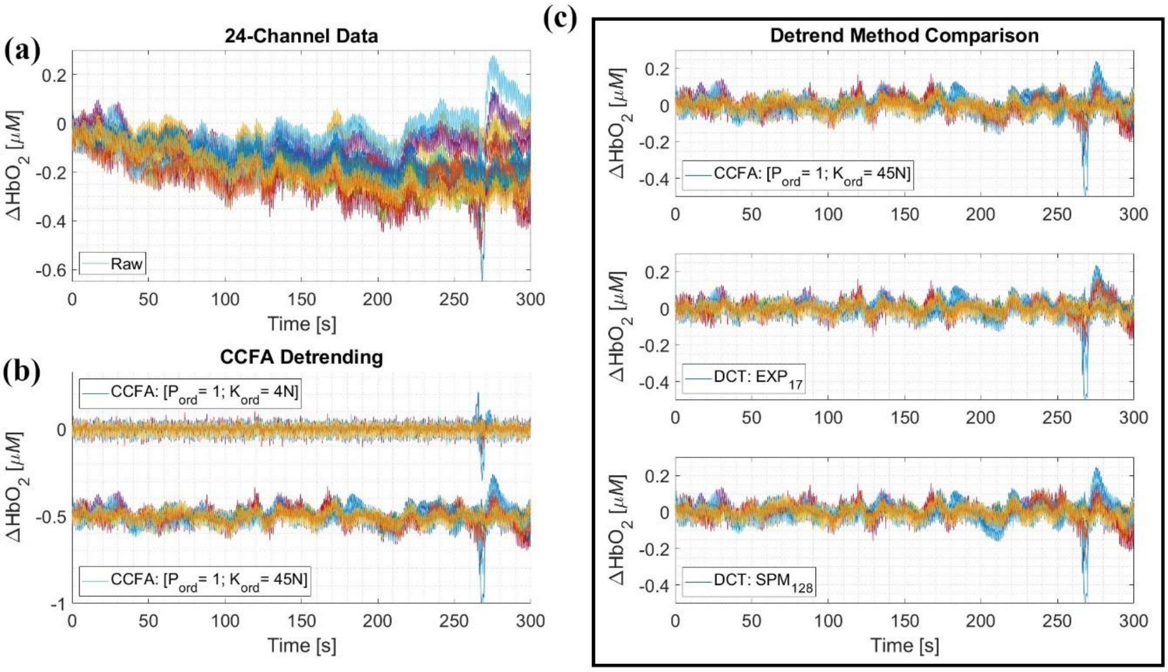

Figure 33. The graphs show the result of detrending using the CCFA algorithm and compares it to the DCT method for non-NC. Panel (a) - the original raw data, (b) - detrended data comparison using CCFA algorithm $k_{ord} = 4N$ and $k_{ord} = 45N$. The latter was given a negative offset of 0.5 for clarity. (c) - detrended signals using three different filtration methods, CCFA using $k_{ord} = 45N$, proposed DCT (EXP_{17}) and DCT from the SPM toolbox.

Figure 33 compares the detrending of the raw data (panel (a)) using the proposed CCFA with different orders (panel (b)) and DCTs based filters (panel (c)). Visually, detrending provides similar results for each of the presented methods. Nonetheless, our proposed method can be used for detrending while avoiding any stationarity assumptions. For detrending purposes, setting the $p_{ord} = 1$ would be the optimal choice for most applications. The k_{ord} parameter value will then regulate the strength of the effect produced by the filter. As can be seen in panel (b), a smaller input parameter ($k_{ord} = 4N$) allows for easier identification of motion artifacts, whereas a larger input parameter ($k_{ord} = 45N$) preserves the hemodynamics in the signal with a higher fidelity.

The synthesized data (as described above) was used to assess the performance of the filtering methods. For each HRF multiplier, the performance was compered in terms of β-value reduction and SNR. Any noisy channels were priorly removed using the MVE algorithm as explained in *"Artifact Detection in fNIRS Data and non-Stationary Preprocessing Methods"* by D.Patashov et.al., resulting in 502 samples in our dataset. Figure 34 shows the effect of the detrending methods on the reduction of the β-values and on the SNR of the signals. The graph presents the output for each of the amplitude multipliers of the HRF for HbO_2 and HbR. Panels (a)&(c) present the β value reduction for HbO_2 and HbR respectively, while (b)&(d) present their SNR value.

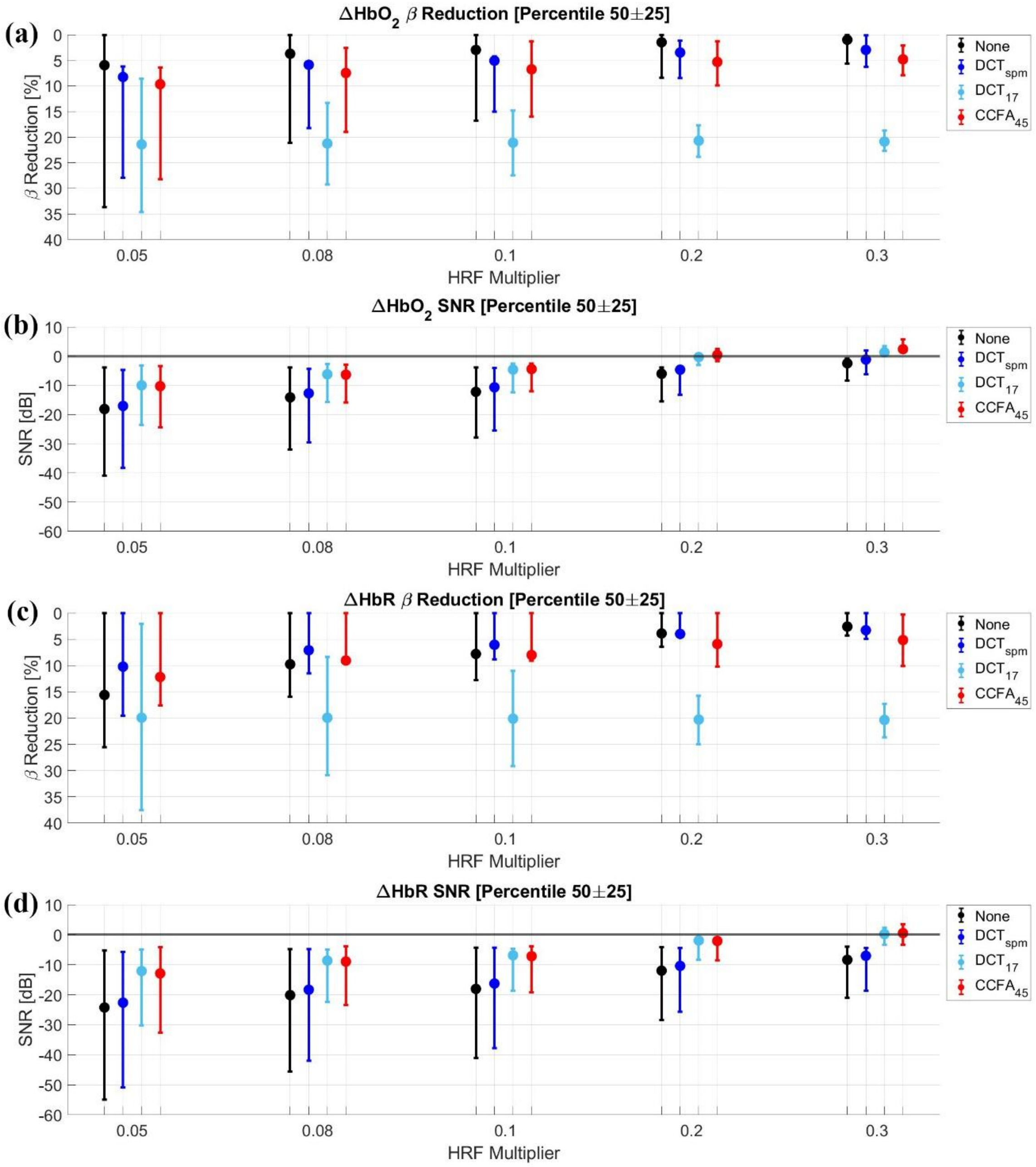

Figure 34. The graphs show a comparison of the evaluation parameters for non-filtered raw signal (black), the proposed CCFA filtration method (red), the DCT based method as used in the SPM (dark blue) and the proposed DCT based method (light blue). Panels (a)&(c) show β-value reduction and panels (b)&(d) present the SNR. Each graph shows the median value and percentiles 25 and 75 for different HRF amplitudes. The actual value of HbR multipliers is third of the displayed value, as defined before. The black horizontal line in panels (b)&(d) indicates 0dB. Wilcoxon signed-rank test was used for comparison. Most comparisons between our method and spectral based ones were found to be significantly different ($p<0.05$). For amplitude multiplier of 0.05 two comparisons were not significantly different ($p>0.05$).

When inspecting the results, it is evident that low SNR affects the β values. Small HRF multipliers resulted in reduced β values obtained for the unprocessed signals. This is due to noise affecting the GLM's performance. The β values' reduction caused by the DCT method from SPM (labeled as DCT_{spm}) and CCFA are comparably small with some cases being slightly in favor of DCT_{spm}. The DCT that filters a larger frequency range using exponential filtering (labeled as DCT_{17}), produces a significant reduction of β values. When assessing the SNR values, CCFA and DCT_{17} provide comparable results, while DCT_{spm} provides a very small improvement over not performing detrending at all. The presented results show that using DCT for detrending of fNIRS signals will either create a distortion that significantly reduces the β values or will have almost no effect on the SNR of the HRF. In contrast, our proposed CCFA method improves the SNR while preserving the β values. It should be emphasized that DCT_{spm} based filtering removes low frequency noise as a matter of fact. Since the trend disappears, it means that certain noise source was removed. Nonetheless, β and SNR values are almost unchanged, meaning that the filtration produces its own noise adding to the contamination. This can be understood from the fact that β almost did not change, meaning that the filtration mainly removed the noise and not the signal. At the same time, SNR also has not changed much, meaning that some new noise appeared in place of the previous one. The β values reduction and SNR improvement tradeoff can be managed by the k_{ord} parameter. For instance, within a certain range of $45N$, lowering k_{ord} will improve the β values reduction, but will also lower the SNR, while increasing the parameter will create the opposite effect. For an overall acceptable efficiency, we recommend using the proposed order: $k_{ord} = 45N$.

fNIRS: ICF

Using non-stationary methods for the filtration of fNIRS temporal signals provided a more stable solution that has relatively low power loss of the information function, while providing higher SNR than the reference methods. Figure 35 presents the complete filtration using the three approaches. The label SBF_{spm} represents the DCT based detrending proposed by SPM, followed by LPF as described above (i.e. FIR-LPF of 500th order with a cutoff at 0.1Hz). Label SBF_{17} is for DCT_{17} detrending followed by the same LPF. The ICF_{45} label represents CCFA based detrending with $k_{ord} = 45N$, followed by IC-LPF using the same cutoff frequency as the regular LPF. When analyzing the results, it is evident that the different detrending methods or even different filtration cutoffs, lead to different effects produced by the filtration of the high frequencies in the following stages. Meaning that the reduction of β values and the improvement of the SNR when performing a Low-Pass filtration is partially dependent on the detrending procedure that was performed beforehand. The presented results indicate that CCFA and ICF enable the reduction of the noise within the signals with a higher efficiency when compared to the conventional DCT and SBF approach, while at the same time generating a relatively small distortion affecting the β values.

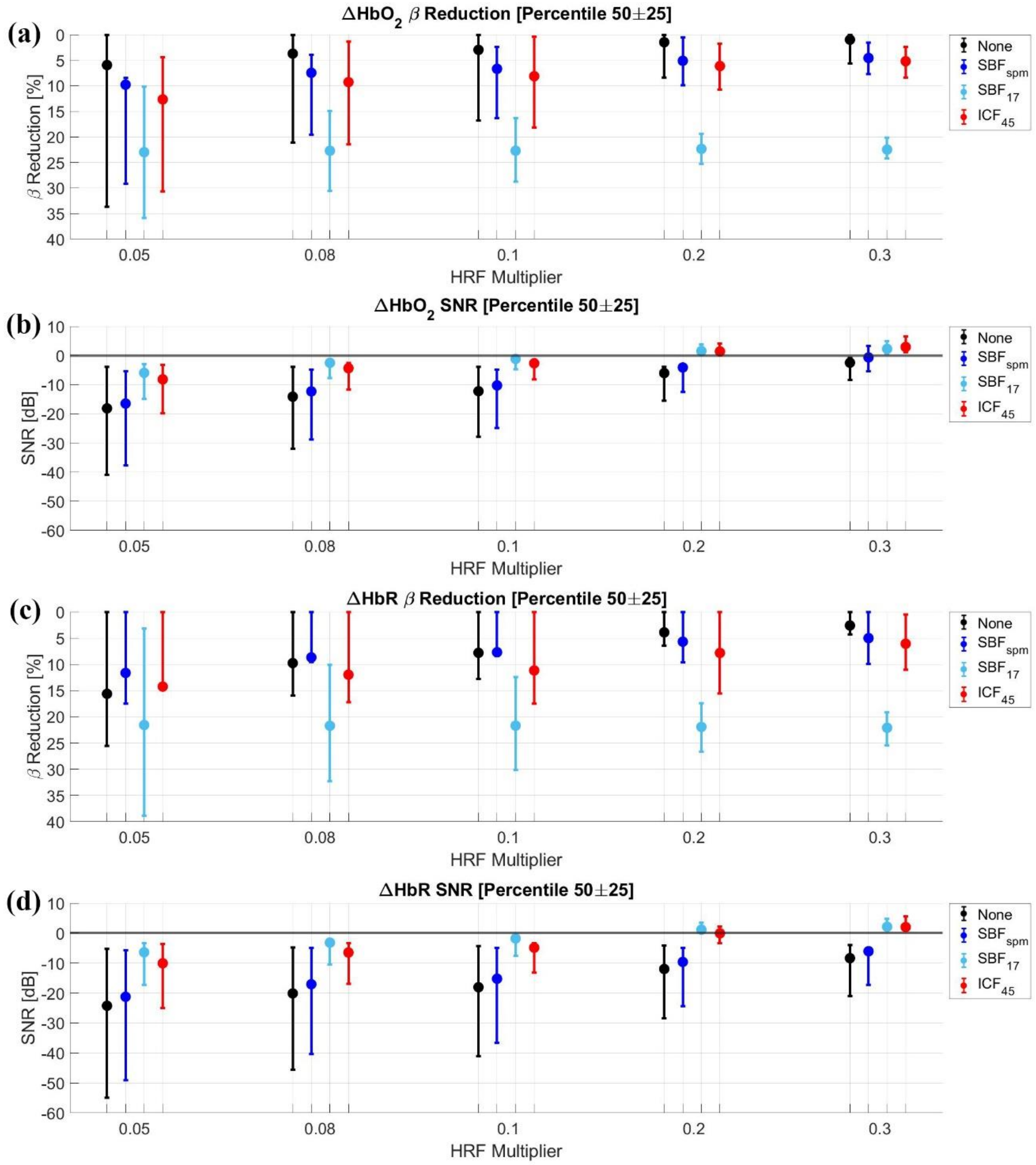

Figure 35. A comparison of the evaluation parameters for non-filtered raw signal (black), the proposed ICF$_{45}$ when the ICF filtration is performed after CCFA$_{45}$ (red), SBFspm when LPF is performed after detrending with DCT from SPM (dark blue) and SBF$_{17}$ when LPF is performed after the DCT$_{17}$ based detrending method (light blue). Panels (a)&(c) show β-value reduction while panels (b)&(d) present the SNR. Each graph shows the median value and percentiles 25 and 75 for different HRF amplitudes. The actual value of HbR multipliers is third of the displayed value, as defined before. The black horizontal line in panels (b)&(d) indicates 0dB. Wilcoxon signed-rank test was used for comparison. Most comparisons between our method and spectral based ones were found to be significantly different ($p<0.05$). For amplitude multiplier of 0.3 one comparison was not significantly different ($p>0.05$).

fNIRS: Analysis

The data collected from fNIRS and fMRI was assessed using GLM to better understand the similarities and differences of the information within. Figure 36 shows the statistical result of the assessment for two subject groups (i.e. Healthy and MDD) using two devices. From examining the results, we can see a similar behavior when using different devices. The fNIRS result seems to be more noisy, but that could be due to the difference in the number of subjects assessed using each device.

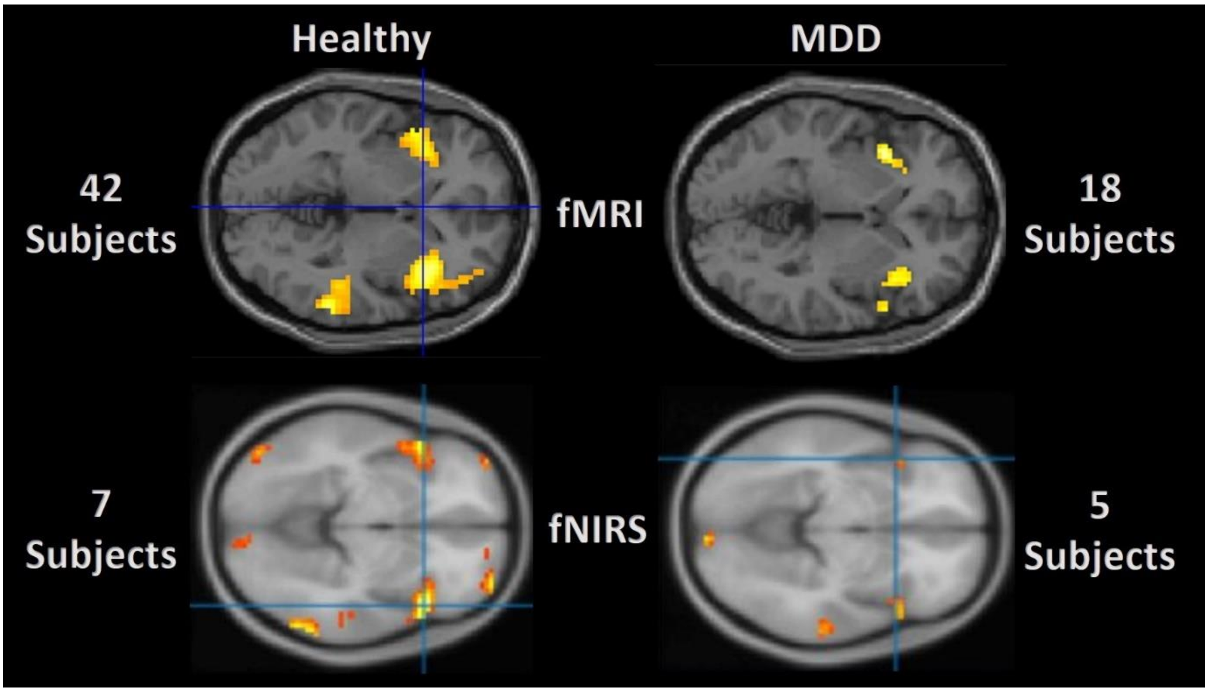

Figure 36. Comparison of the active regions when performing Go-NoGo task. Assessment was done using GLM.

When comparing Healthy and MMD subjects [Figure 36], it is evident that activity within the temporal regions of MDD subjects is reduced when compared to Healthy ones. Functional connectivity maps were calculated to assess the connectivity of the temporal regions both within each hemisphere (between the channels) and between the two hemispheres [Figure 37].

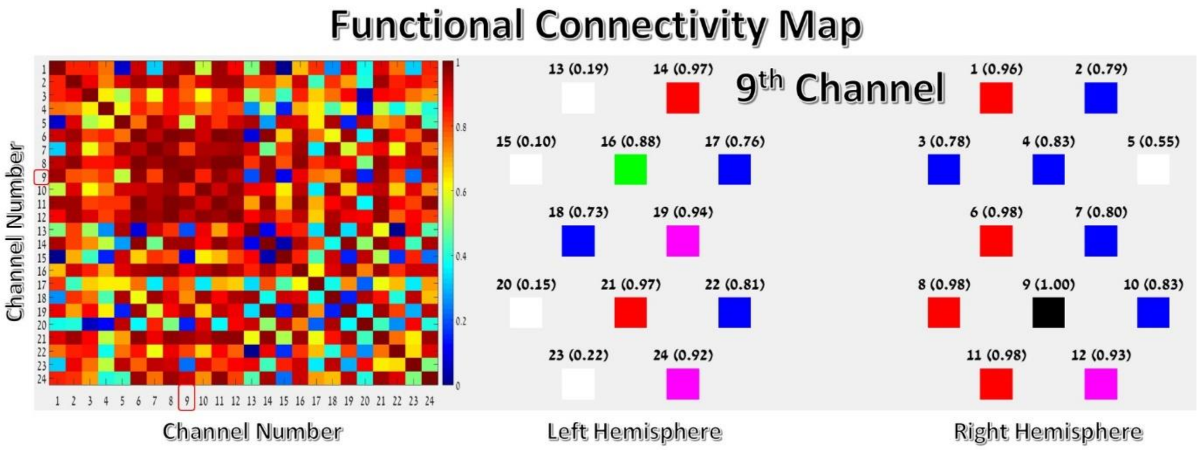

Figure 37. Example of a functional connectivity map from a single subject. The graphical representation on the right shows the relative positions of the channels on the temporal regions of the two hemispheres. The colormap of the single channel connectivity is based on correlation levels between each channel and the selected one. The color order is in ascending order from low to high correlation: White – Blue – Green – Purple – Red. Channel number and correlation level is shown above each node.

From examination of the connectivity maps [Figure 37] of all subjects, a reduction in connectivity levels was observed in MDD subjects when compared to Healthy [Figure 38].

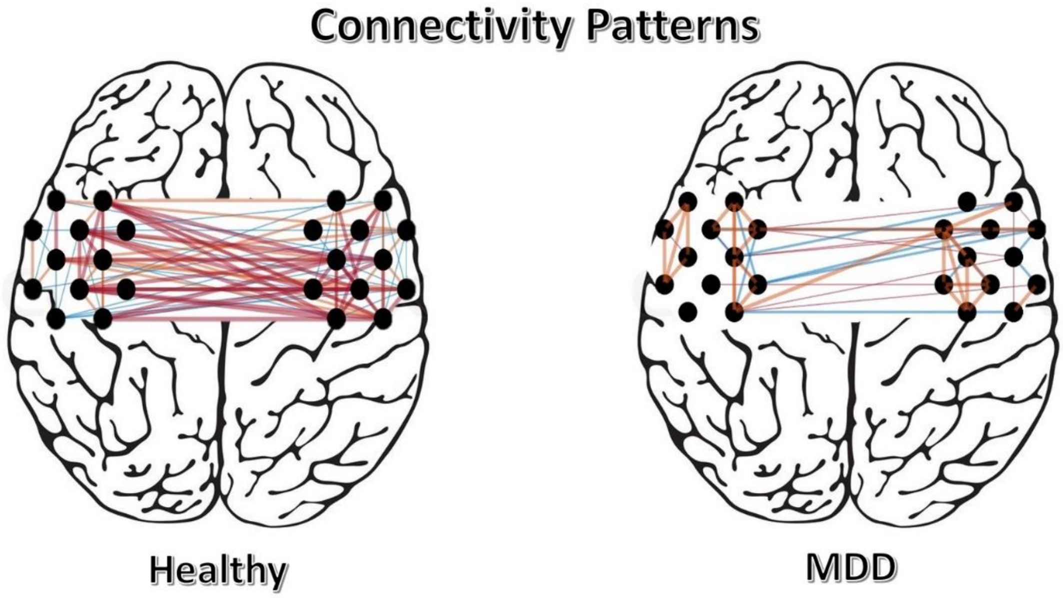

Figure 38. Connectivity patterns comparison between Healthy and MDD subjects. Color of the line shows the level of correlation in ascending order: Blue – Orange – Red. The weight of the line also represents the correlation level. The thicker the line the higher the correlation. The colors are based on the predefined levels while the line weights are gradations within those levels.

Discussion

The aim of this work is to develop accurate, robust and reliable algorithms dedicated for processing and analysis of the biomedical information. The proposed solutions were developed while addressing the unique qualities of the biomedical information, thus provide a better performance than the general-purpose methods integrated into the field.

Location of the extrema points is an important task that frequently arise in biomedical information processing and analysis. The SDET algorithm allows for the detection of all local extrema of quasi-periodic, noisy signals. Depending on the target of interest, using minor adjustments such as running fewer iterations or matching the optimal filtration method and point adjustment logic can provide more accurate results that are almost unaffected by noise. It can be seen in ([30], [31]) where different adjustments were made depending on the task at hand. In [30] the LPF-based smoothing procedure was defined that can be used as a general case solution for any task where LPF is applicable. That said, the point adjustment was tailormade for the task, thus should be considered separately if the proposed procedure is used. On the other hand, in [31], the used point adjustment procedure can be used for many other tasks, while the filtration procedure was tailormade for the specific task. This shows the flexibility and adjustability of the SDET algorithm. These adjustments allow for the solution of a wide spectrum of problems where peak detection of a quasi-periodic signal is required. The information source does not have to be temporal and based on the chose filtration procedure, it can also be suitable for non-stationary signals. By choosing the optimal filtration and point adjustment procedures, this method can solve almost any task of peak detection.

Obstacle avoidance strategy that includes the preparation phase and the recovery phase can shed light on motoric and neurological disorders of the subject when analyzed by a medical specialist. Therefore, it is important to detect and extract the information related to the obstacle avoidance task for further analysis by the physician. To address this matter, a simple signal segmentation method was designed [30]. The approach uses the variability of the signals' envelope to detect the pattern change. This solution is valid for walking on a treadmill only, because the constant pace dictated by the treadmill creates a very stable envelope in the walking signals along the treadmill length. Whenever this stability is distorted, it means that the subject's pace was disrupted, thus the irregularity in the walking pattern is the segment where the pattern is inconsistent. When subject performs an obstacle avoidance task, the walking pattern is usually disrupted. Therefore, we combined these two parts and extracted the inconsistent parts of gait around the obstacles. These parts can provide information regarding the obstacle avoidance strategy and allow the physician to analyze the performance. The irregular steps within the disrupted walking segment were detected using a simple kernel-based clustering [30]. While disrupted segments provide information regarding the avoidance strategy, detection of irregular steps within those segments can indicate disorders or walking irregularities which can lead to falls. Thus, it is very important to both assess the strategy of preparation and recovery phases of obstacle avoidance, and the irregularity in individual steps in close proximity to the obstacle.

Gait Related Potential (GRP) that was detected and assessed in [31] was very noisy and unstable due to gait performance while recording EEG. The developed APC parameter assesses the variability of the wave patterns in the recorded signal and provides additional information regarding brain performance. The idea of the measurement is to assess how stable are peak amplitudes of the different waves within the epoch (i.e. single stride cycle). Since some subjects had a more chaotic activation patterns while others had relatively stable ones, APC provides an added value to the assessment procedure. Using the APC, we were able to better understand the effects of ageing on dual-task walking [31].

Cumulative Curve Fitting Approximation is a filtration procedure with multiple capabilities (i.e. filtration, missing samples approximation and resampling). CCFA is a powerful tool that can be adjusted to almost any type of process. The process does not have to be quasi-periodic or temporal and no stationarity or linearity assumptions are being made regarding the target process. It has three main parameters – algorithm procedure type λ that defines open, semi-open or closed loop procedure, algorithm order k that defines procedure window size and the number of corrections performed on every sample, and the type of weighted curve fitting procedure along with any of its own parameters. For example, in case of weighted polynomial curve fitting, the degree of the polynomial p_{ord} that is used for the approximation, becomes the third input parameter. These parameters should be carefully selected for each task separately. For the majority of tasks, all the remaining parameters can be set to their default values as suggested in the methods section. Nonetheless, they can also be adjusted for each case independently to achieve maximum accuracy. It should be noted though, that selection of optimal parameters may be a difficult task of its own and is one of the limitations of the algorithm. That said, if the optimal parameters are provided, the accuracy of the algorithm becomes exceptionally high.

It is not uncommon for systems to provide faulty results due to some errors, miscalculations or unforeseen events. At times, it results in missing or untrustworthy data. For some types of algorithms, these missing data occurrences are devastating when it comes to providing accurate results, even if they are not in the regions of interest. CCFA approximates the curvature of the process based on the existing samples and can take into account the inaccuracy of samples if such information is available. Inaccuracy is defined by weights corresponding to the samples that can have values between zero and one. One represents a well recorded sample, while fraction represents an inaccurate one. The value of the fraction describes how inaccurate the sample is. The lower the value the less accurate the sample is with zero being the extreme case of inaccuracy which is treated as missing sample. Depending on the remaining input parameters, CCFA can simultaneously perform filtration and missing samples approximation or either of them separately. The resampling can be done using algorithm's ability to approximate missing samples, as new sampling locations can be treated as missing samples. In gait analysis study, V-TIME system occasionally produced missing samples [30]. CCFA was used to approximate these samples. It is very flexible in terms of adaptation to signal structure as long as provided with correct input parameters. Though these parameters are not always easy to estimate, they can be predicted using ML techniques such as the one presented in our work [30]. We anticipate that if we were to use a better suited forecasting algorithm, even better results could be reached. The basis to that statement is the accuracy achieved when using the optimal input parameters within a predefined range [Table 1]. It shows the potential of the method that may be achieved if a more accurate input parameters' prediction procedure is used.

CCFA can be used almost on any type of signal, given the correct input parameters. A good example to that statement is the use of CCFA for detrending of the fNIRS signals. Detrending of these signals is performed in order to remove low frequency drifts from the data. Several methods have been reported, starting from High Pass Filter (HPF) [86] and DCT [81] to wavelet minimum description length (MDL)[107]. CCFA was used for the filtration of the first statistical moment within the fNIRS signals (i.e. detrending) and compared to detrending using two approaches of DCT based filtering. The filtration is performed by accumulation of weighted polynomial-fitted functions, within the overlap of their respective windows. The size of the window (k_{ord}) and the degree of the polynomial fit (p_{ord}), determine the filtering response of the CCFA approach. As seen in panel (b) of Figure 33, a lower k_{ord} parameter results in filtration of higher frequency components. Whereas a higher p_{ord} value results in filtration of higher frequency components (not demonstrated). For removal of the first statistical moment, $p_{ord} = 1$ was applied. This approach is non-linear and does not assume stationarity as opposed to the HPF or DCT methods, thus is more suitable for processing of fNIRS data. In order to test the performance of our novel approach that uses CCFA, we have chosen to follow the method described by Pinti et. al. [86], and constructed an artificial comb of HRFs that was added to the resting state period in our dataset for all optimally-coupled channels (termed Artificial Data here). The Artificial Data was constructed using the amplitudes described by [93], for both oxygenated and deoxygenated hemoglobin. Following, we have filtered the Artificial Data using DCT detrending or using CCFA filtering. For the two filtered datasets we have calculated the change in the GLM extracted β-values, that corresponds to the contribution of the HRF to the Artificial Data, and the SNR. The SNR was defined by accounting for the different amplitudes of the HRF and the β-values' reduction. There are several differences in our process, compared to the one described in [86]: Our dataset includes five minutes of rest, followed by a cognitive task with short stimuli, separated by two (2) seconds on average. In order to apply our algorithm to this cognitive dataset in the future, we have decided to use a Dirac comb, with a period of 20 seconds for convolution with the HRF and not 20 seconds blocks, as in [86]. We have observed that the calculated β-values were not normally distributed and that even a small change in the mean value resulted in a significant p-value. Our results indicate that the SNR obtained using our methods is higher in comparison to the ones obtained following the conventional filtering (using DCT from SPM), for all of the amplitudes of the HRF. At the same time, β-values' reduction remains considerably small, in comparison to the proposed DCT$_{17}$. This implies that the HRF contributions that lie within the frequency range of our filters are not affected much, while the noise that reside in the same spectral band are reduced more significantly when compared to the conventional DCT filters. The combination of β-values' reduction and SNR measurements provides additional information when examined together. Any detrending procedure removes some information from the signal. The important question is what information is being removed and how does it affect the information that we would like to assess. β-values' reduction shows how much power loss had occurred in the target component. When using DCT$_{spm}$, information power loss is quite low. Meaning that the procedure does not damage the relevant information component within the signal. Which is a very good sign since it means that we mainly remove the noise component. When we assess the SNR improvement produced by DCT$_{spm}$, we find a very low improvement. Which is surprising at first glance. If we reduced the noise, and we know for a fact that we did, then the SNR value should have increased since the information source was almost unaffected, but it did not. The explanation to this phenomena can be the non-stationarity of the signals. Since DCT is a method that assumes stationarity, it creates distortion within the fNIRS signals when used. Meaning that, although we removed some type of noise, the fact that there was almost no improvement in the SNR suggests that a new type of noise was introduced in place of the removed one. The distortion of the target function by the stationarity assumption can perfectly explain the results.

Hemodynamic Response Function (HRF) is the information function that we aim to assess when analyzing the fNIRS signals. It is well known that HRF mainly resides in low-frequency spectrum of the signals. Therefore, high-frequency contamination of the signals should be removed to allow for more accurate assessment of the HRF. For that purpose, ICF method was developed. The idea of this approach is to decompose the signals into their IMFs using EMD. Since EMD does not assume stationarity or linearity of the process it is applied to, it is a suitable method for processing fNIRS data. Our proposed solution uses PSD of the IMFs to allow for thresholding base on desired frequency ranges. Meaning that any frequency ranges that previously provided reasonable results, can be used in ICF while avoiding the stationarity assumption made by standard spectral based filtering methods. This is due to the filtration procedure used in the ICF. When IMF's SED is mainly within the frequency range that we wish to remove, the entire IMF is removed before the recombination of the signal. Since IMFs were calculated without the linearity or stationarity assumptions, their removal produces less distortion than the one produced by methods that have those assumptions. Thus resulting in a more reliable and accurate removal of the information contamination sources. Result shown in Figure 35 indicate that just like with the detrending approach, low pass filtering using IC-LPF is more stable and reliable than standard LPF procedure.

Conclusions

Some of the developed methods are dedicated for the very specific tasks within this study, while others may serve as general-purpose solutions for almost any type of signals. SDET algorithm is a heuristic, general purpose solution that can be applied to any quasi-periodic signal for peak detection. The target signal does not have to be temporal, but it must have similar qualities to those of a temporal signal. Depending on the filtration procedure used for smoothing, this method can be used on non-stationary signlas. It should be noted that SDET is not limited to 1-dimensional signals and can be applied to high-dimensional data as well. The disadvantages and limitations of this method are the requirement to adjust it to every type of peak detection task manually and the assumption that it is possible to filter out any unnecessary peaks while preserving the number of relevant ones in their respective areas. In some cases, this type of filtration is unachievable, thus may lead to incorrect detections on such signals.

Signal segmentation and kernel-based clustering are solutions that were specifically developed for this study and may not be usable for other types of data. While the approach of assessment of the complex envelopes can be used as a segmentation method in many types of signals, the developed auxiliary function and the further procedure of segmentation rely on signal properties that are normally only present when performing gait on a treadmill. Similar limitations are present in the kernel-based clustering. Though the kernel function itself is a general purpose one, the full procedure was developed specifically for this study.

CCFA algorithm is yet another general-purpose solution that can be applied to any type of signal. The signal does not have to be quasi-periodic or temporal. Also, this method does not assume stationarity or linearity of the processes it is applied to. The algorithm can perform different tasks, such as: filtering, resampling and approximation of missing samples. It is very robust to noise and other data impurities, and provides a very flexible solution that can be adjusted to solve many different tasks with a reasonably high accuracy. In theory, CCFA is not limited to 1-dimensional signals, but extending it to higher dimensionality is quite hard and severely complicates the solution with each added dimension. The disadvantages and limitations of this algorithm are the large number of input parameters that sometimes are hard to estimate, even though many of them can be defined using default values as proposed in this work; The relatively long runtime of the algorithm makes it impractical for many real-time applications.

Artifact detection algorithms: MVE and CSV are dedicated solutions for fNIRS data. The core assumptions of these methods are related to human physiology and how that physiology affects fNIRS data. Though they may be suitable to fNIRS data collected from animals or other types of data that have qualities matching the method's assumptions. Also, both methods were developed for multi-channel systems, and cannot be used on systems with just a few channels. However, these algorithms can be used in real-time systems with very minor adjustments.

Filtration algorithm termed ICF is a general-purpose solution for filtration of nonlinear and non-stationary data. Filtered process does not have to be quasi-periodic, but should have properties similar to those of a temporal process. This algorithm can be used in place of Fourier based filtering to reduce the distortions created by the stationarity and linearity assumptions. Any passband or stopband filter that can be defined for Fourier domain, can be defined for ICF. The most important part is that the frequency ranges for spectral-band filtering can be used exactly the same as in Fourier based filtering. The limitations of this method are similar to the limitations of Fourier-based filtering, but without the assumption of stationarity or linearity of the filtered signal. In addition, although ICF is not limited to 1-dimensional data, the increase of dimensionality leads to complication of the procedure.

The provided solutions allow for classic gait analysis to be performed by the physicians based on the extracted information. SDET algorithm accurately detects the peaks of the gait [30] that can be used to calculate stride/step length and duration, and assess their variability, degeneration due to fatigue through the trial and improvement of the performance through the training course. It also allows for analysis of different gait phases. Segmentation and kernel-based clustering allow the physicians to assess performance related to obstacle avoidance task, to analyze the strategy and to identify abnormalities. This information can provide insights on the neuromuscular diseases, physiological abnormalities or disorders. Missing data approximation procedure (CCFA) as proposed in our study [30] was able to estimate the missing samples with an outstanding accuracy [Table 1 & Table 2], outperforming the commonly used methods by a large margin.

The proposed SDET solution for the analysis of GRPs is very robust and insensitive to noise, thus providing us with accurate information regarding neuronal activation patterns [31]. APC was successful in expanding the knowledge that we have regarding the differences of neuronal activation patterns between different subject groups [31]. The proposed procedures and algorithms provide solutions that allow for assessment of the effects of aging and a parallel motoric task on the performance of cognitive task (i.e. odd ball)[64]. Furthermore, they allow for the assessment of GRP and of the effects of ageing and parallel cognitive task on the performance of gait [31].

The developed methods for the preprocessing of the fNIRS signals provide the complete information regarding the integrity of the collected data [Figure 32]. The signals affected by artifacts (MVE [Figure 9]) or affected signal segments (CSV [Figure 30] and spike detection [Figure 31]) are accurately detected allowing the user to take them into consideration for further analysis and processing such as artifact removal [108], for example. Non-stationary filtering methods (CCFA and ICF) were shown to reduce the noise affecting the signals better than the commonly used solutions, while preserving the information function just as well (CCFA [Figure 34] and ICF [Figure 35]). When performing functional connectivity analysis like in [89], the proposed methods may improve the accuracy of the assessment and allow for more information to be extracted. To conclude, it is evident that methods proposed in this study provide additional, robust tools that have a reasonably high accuracy. The solutions take into account the unique characteristics and qualities of the assessed data, thus create less distortions of the analyzed information. Quantitative accuracy assessments of the proposed algorithms show that our methods can achieve higher quality results than those produced by the commonly used methods. Therefore, our findings provide a justification for our assumptions and statements throughout this work.

Acknowledgements

Gait related research was supported in part by the European Commission (FP7 project V-TIME-278169).
Partial funding was provided by the BSMT consortium of the Israeli Innovation authority for the fNIRS related study.

The data for the experiments and development were collected at Tel Aviv Sourasky Medical Center's: Center for the study of Movement, Cognition and Mobility (CMCM), Department of Neurology, Laboratory for Early Markers of Neurodegeneration (LEMON) and the Laboratory for Brain and Emotion Experience Sagol Brain Institute, Wohl Institute for Advanced Imaging.

The processing equipment and fNIRS device were provided by Holon Institute of Technology (HIT). All the data was processed at Mathematical Modelling Center, HIT.

References

[1] J. A. Stevens, M. F. Ballesteros, K. A. Mack, R. A. Rudd, E. DeCaro, and G. Adler, “Gender Differences in Seeking Care for Falls in the Aged Medicare Population,” *Am. J. Prev. Med.*, vol. 43, no. 1, pp. 59–62, Jul. 2012, doi: 10.1016/j.amepre.2012.03.008.

[2] J. L. O’Loughlin, Y. Robitaille, J.-F. Boivin, and S. Suissa, “Incidence of and Risk Factors for Falls and Injurious Falls among the Community-dwelling Elderly,” *Am. J. Epidemiol.*, vol. 137, no. 3, pp. 342–354, Feb. 1993, doi: 10.1093/oxfordjournals.aje.a116681.

[3] B. Kaymak and A. R. Soylu, “Fundamentals of Quantitative Gait Analysis,” in *Musculoskeletal Research and Basic Science*, Cham: Springer International Publishing, 2016, pp. 93–106.

[4] J. B. Dingwell and B. L. Davis, “A Rehabilitation Treadmill With Software for Providing Real-Time Gait Analysis and Visual Feedback,” *J. Biomech. Eng.*, vol. 118, no. 2, pp. 253–255, May 1996, doi: 10.1115/1.2795968.

[5] J. B. Dingwell, B. L. Davis, and D. M. Frazder, “Use of an instrumented treadmill for real-time gait symmetry evaluation and feedback in normal and trans-tibial amputee subjects,” *Prosthetics Orthot. Int.*, vol. 20, no. 2, pp. 101–110, Aug. 1996, doi: 10.3109/03093649609164426.

[6] R. C. NELSON, C. J. DILLMAN, P. LAGASSE, and P. BICKETT, “Biomechanics of overground versus treadmill running,” *Med. Sci. Sport. Exerc.*, vol. 4, no. 4, p. 233, 1972, doi: 10.1249/00005768-197200440-00029.

[7] J. C. WALL and J. CHARTERIS, “A kinematic study of long-term habituation to treadmill walking,” *Ergonomics*, vol. 24, no. 7, pp. 531–542, Jul. 1981, doi: 10.1080/00140138108924874.

[8] L. F. Reed, S. R. Urry, and S. C. Wearing, “Reliability of spatiotemporal and kinetic gait parameters determined by a new instrumented treadmill system,” *BMC Musculoskelet. Disord.*, vol. 14, no. 1, p. 249, Dec. 2013, doi: 10.1186/1471-2474-14-249.

[9] N. Mannering, T. Young, T. Spelman, and P. F. Choong, “Three-dimensional knee kinematic analysis during treadmill gait,” *Bone Joint Res.*, vol. 6, no. 8, pp. 514–521, Aug. 2017, doi: 10.1302/2046-3758.68.BJR-2016-0296.R1.

[10] G. S. de S. e Souza, F. B. Rodrigues, A. O. Andrade, and M. F. Vieira, “A simple, reliable method to determine the mean gait speed using heel markers on a treadmill,” *Comput. Methods Biomech. Biomed. Engin.*, vol. 20, no. 8, pp. 901–904, Jun. 2017, doi: 10.1080/10255842.2017.1309395.

[11] L. Tesio, C. Malloggi, N. M. Portinaro, L. Catino, N. Lovecchio, and V. Rota, “Gait analysis on force treadmill in children: comparison with results from ground-based force platforms,” *Int. J. Rehabil. Res.*, vol. 40, no. 4, pp. 315–324, Dec. 2017, doi: 10.1097/MRR.0000000000000243.

[12] C. Cho, W. Hwang, S. Hwang, and Y. Chung, “Treadmill Training with Virtual Reality Improves Gait, Balance, and Muscle Strength in Children with Cerebral Palsy,” *Tohoku J. Exp. Med.*, vol. 238, no. 3, pp. 213–218, 2016, doi: 10.1620/tjem.238.213.

[13] M. Oh-Park, R. Holtzer, J. Mahoney, C. Wang, and J. Verghese, “Effect of Treadmill Training on Specific Gait Parameters in Older Adults With Frailty,” *J. Geriatr. Phys. Ther.*, vol. 34, no. 4, pp.

184–188, Oct. 2011, doi: 10.1519/JPT.0b013e3182193165.

[14] A. Peruzzi, A. Cereatti, U. Delia Croce, I. R. Zarbo, and A. Mirelman, “Treadmill-virtual reality combined training program to improve gait in multiple sclerosis individuals,” in *2015 International Conference on Virtual Rehabilitation (ICVR)*, Jun. 2015, pp. 18–23, doi: 10.1109/ICVR.2015.7358581.

[15] A. Mirelman *et al.*, “V-TIME: a treadmill training program augmented by virtual reality to decrease fall risk in older adults: study design of a randomized controlled trial,” *BMC Neurol.*, vol. 13, no. 1, p. 15, Dec. 2013, doi: 10.1186/1471-2377-13-15.

[16] A. Mirelman *et al.*, “Addition of a non-immersive virtual reality component to treadmill training to reduce fall risk in older adults (V-TIME): a randomised controlled trial,” *Lancet*, vol. 388, no. 10050, pp. 1170–1182, Sep. 2016, doi: 10.1016/S0140-6736(16)31325-3.

[17] S. R. Shema *et al.*, “Clinical Experience Using a 5-Week Treadmill Training Program With Virtual Reality to Enhance Gait in an Ambulatory Physical Therapy Service,” *Phys. Ther.*, vol. 94, no. 9, pp. 1319–1326, Sep. 2014, doi: 10.2522/ptj.20130305.

[18] K. Harmer, G. Howells, W. Sheng, M. Fairhurst, and F. Deravi, “A Peak-Trough Detection Algorithm Based on Momentum,” in *2008 Congress on Image and Signal Processing*, 2008, pp. 454–458, doi: 10.1109/CISP.2008.704.

[19] K. H. Jarman, D. S. Daly, K. K. Anderson, and K. L. Wahl, “A new approach to automated peak detection,” *Chemom. Intell. Lab. Syst.*, vol. 69, no. 1–2, pp. 61–76, Nov. 2003, doi: 10.1016/S0169-7439(03)00113-8.

[20] N. Mtetwa and L. S. Smith, “Smoothing and thresholding in neuronal spike detection,” *Neurocomputing*, vol. 69, no. 10–12, pp. 1366–1370, Jun. 2006, doi: 10.1016/j.neucom.2005.12.108.

[21] Z. Nenadic and J. W. Burdick, “Spike Detection Using the Continuous Wavelet Transform,” *IEEE Trans. Biomed. Eng.*, vol. 52, no. 1, pp. 74–87, Jan. 2005, doi: 10.1109/TBME.2004.839800.

[22] A. Wee, D. B. Grayden, Y. Zhu, K. Petkovic-Duran, and D. Smith, “A continuous wavelet transform algorithm for peak detection,” *Electrophoresis*, vol. 29, no. 20, pp. 4215–4225, Nov. 2008, doi: 10.1002/elps.200800096.

[23] F. Scholkmann, J. Boss, and M. Wolf, “An Efficient Algorithm for Automatic Peak Detection in Noisy Periodic and Quasi-Periodic Signals,” *Algorithms*, vol. 5, no. 4, pp. 588–603, Nov. 2012, doi: 10.3390/a5040588.

[24] P. Du, W. A. Kibbe, and S. M. Lin, “Improved peak detection in mass spectrum by incorporating continuous wavelet transform-based pattern matching,” *Bioinformatics*, vol. 22, no. 17, pp. 2059–2065, Sep. 2006, doi: 10.1093/bioinformatics/btl355.

[25] A. Ukil and R. Zivanovic, “Automatic signal segmentation based on abrupt change detection for power systems applications,” in *2006 IEEE Power India Conference*, 2006, p. 8 pp., doi: 10.1109/POWERI.2006.1632488.

[26] P. Hubert, L. Padovese, and J. Stern, “A Sequential Algorithm for Signal Segmentation,” *Entropy*, vol. 20, no. 1, p. 55, Jan. 2018, doi: 10.3390/e20010055.

[27] H. Hassanpour and M. Shahiri, “Adaptive Segmentation Using Wavelet Transform,” in *2007 International Conference on Electrical Engineering*, Apr. 2007, pp. 1–5, doi: 10.1109/ICEE.2007.4287348.

[28] S. D. Conte, *Numerical analysis*, vol. 9, no. 7. New York, NY: Springer New York, 1966.

[29] P. J. Brockwell and R. A. Davis, *Introduction to Time Series and Forecasting*. Cham: Springer International Publishing, 2016.

[30] D. Patashov *et al.*, “Methods for Gait Analysis During Obstacle Avoidance Task,” *Ann. Biomed. Eng.*, vol. 48, no. 2, pp. 634–643, Feb. 2020, doi: 10.1007/s10439-019-02380-4.

[31] I. Maidan *et al.*, “A new approach to quantifying the EEG during walking: Initial evidence of gait related potentials and their changes with aging and dual tasking,” *Exp. Gerontol.*, vol. 126, p. 110709, Oct. 2019, doi: 10.1016/j.exger.2019.110709.

[32] M. Montero-Odasso, J. Verghese, O. Beauchet, and J. M. Hausdorff, “Gait and Cognition: A Complementary Approach to Understanding Brain Function and the Risk of Falling,” *J. Am. Geriatr. Soc.*, vol. 60, no. 11, pp. 2127–2136, Nov. 2012, doi: 10.1111/j.1532-5415.2012.04209.x.

[33] M. Woollacott and A. Shumway-Cook, “Attention and the control of posture and gait: a review of an emerging area of research,” *Gait Posture*, vol. 16, no. 1, pp. 1–14, Aug. 2002, doi: 10.1016/S0966-6362(01)00156-4.

[34] J. M. Hausdorff, A. Schweiger, T. Herman, G. Yogev-Seligmann, and N. Giladi, “Dual-Task Decrements in Gait: Contributing Factors Among Healthy Older Adults,” *Journals Gerontol. Ser. A Biol. Sci. Med. Sci.*, vol. 63, no. 12, pp. 1335–1343, Dec. 2008, doi: 10.1093/gerona/63.12.1335.

[35] G. Yogev-Seligmann, J. M. Hausdorff, and N. Giladi, “The role of executive function and attention in gait,” *Mov. Disord.*, vol. 23, no. 3, pp. 329–342, Feb. 2008, doi: 10.1002/mds.21720.

[36] O. Segev-Jacubovski, T. Herman, G. Yogev-Seligmann, A. Mirelman, N. Giladi, and J. M. Hausdorff, “The interplay between gait, falls and cognition: can cognitive therapy reduce fall risk?,” *Expert Rev. Neurother.*, vol. 11, no. 7, pp. 1057–1075, Jul. 2011, doi: 10.1586/ern.11.69.

[37] I. Maidan *et al.*, “Altered brain activation in complex walking conditions in patients with Parkinson’s disease,” *Parkinsonism Relat. Disord.*, vol. 25, pp. 91–96, Apr. 2016, doi: 10.1016/j.parkreldis.2016.01.025.

[38] D. S. Peterson, K. A. Pickett, R. P. Duncan, J. S. Perlmutter, and G. M. Earhart, “Brain activity during complex imagined gait tasks in Parkinson disease,” *Clin. Neurophysiol.*, vol. 125, no. 5, pp. 995–1005, May 2014, doi: 10.1016/j.clinph.2013.10.008.

[39] F. Nieuwhof *et al.*, “Impaired dual tasking in Parkinson’s disease is associated with reduced focusing of cortico-striatal activity,” *Brain*, vol. 140, no. 5, pp. 1384–1398, May 2017, doi: 10.1093/brain/awx042.

[40] J. M. Shine *et al.*, “Freezing of gait in Parkinson’s disease is associated with functional decoupling between the cognitive control network and the basal ganglia,” *Brain*, vol. 136, no. 12, pp. 3671–3681, Dec. 2013, doi: 10.1093/brain/awt272.

[41] R. Holtzer, J. R. Mahoney, M. Izzetoglu, C. Wang, S. England, and J. Verghese, “Online fronto-cortical control of simple and attention-demanding locomotion in humans,” *Neuroimage*, vol. 112, pp. 152–159, May 2015, doi: 10.1016/j.neuroimage.2015.03.002.

[42] F. G. Metzger *et al.*, “Functional brain imaging of walking while talking – An fNIRS study,” *Neuroscience*, vol. 343, pp. 85–93, Feb. 2017, doi: 10.1016/j.neuroscience.2016.11.032.

[43] A. Mirelman, I. Maidan, H. Bernad-Elazari, S. Shustack, N. Giladi, and J. M. Hausdorff, “Effects of aging on prefrontal brain activation during challenging walking conditions,” *Brain Cogn.*, vol. 115, pp. 41–46, Jul. 2017, doi: 10.1016/j.bandc.2017.04.002.

[44] I. Maidan *et al.*, “The Role of the Frontal Lobe in Complex Walking Among Patients With Parkinson’s Disease and Healthy Older Adults,” *Neurorehabil. Neural Repair*, vol. 30, no. 10, pp. 963–971, Nov. 2016, doi: 10.1177/1545968316650426.

[45] M. Ferrari and V. Quaresima, “A brief review on the history of human functional near-infrared spectroscopy (fNIRS) development and fields of application,” *Neuroimage*, vol. 63, no. 2, pp. 921–935, Nov. 2012, doi: 10.1016/j.neuroimage.2012.03.049.

[46] T. C. Bulea, J. Kim, D. L. Damiano, C. J. Stanley, and H.-S. Park, “Prefrontal, posterior parietal and sensorimotor network activity underlying speed control during walking,” *Front. Hum. Neurosci.*, vol. 9, May 2015, doi: 10.3389/fnhum.2015.00247.

[47] J. T. Gwin, K. Gramann, S. Makeig, and D. P. Ferris, “Electrocortical activity is coupled to gait cycle phase during treadmill walking,” *Neuroimage*, vol. 54, no. 2, pp. 1289–1296, Jan. 2011, doi: 10.1016/j.neuroimage.2010.08.066.

[48] S. Pizzamiglio, H. Abdalla, U. Naeem, and D. L. Turner, “Neural predictors of gait stability when walking freely in the real-world,” *J. Neuroeng. Rehabil.*, vol. 15, no. 1, p. 11, Dec. 2018, doi: 10.1186/s12984-018-0357-z.

[49] M. Seeber, R. Scherer, J. Wagner, T. Solis-Escalante, and G. R. MÃ¼ller-Putz, “EEG beta suppression and low gamma modulation are different elements of human upright walking,” *Front. Hum. Neurosci.*, vol. 8, Jul. 2014, doi: 10.3389/fnhum.2014.00485.

[50] G. Lisi and J. Morimoto, “EEG Single-Trial Detection of Gait Speed Changes during Treadmill Walk,” *PLoS One*, vol. 10, no. 5, p. e0125479, May 2015, doi: 10.1371/journal.pone.0125479.

[51] C. C. Duncan *et al.*, “Event-related potentials in clinical research: Guidelines for eliciting, recording, and quantifying mismatch negativity, P300, and N400,” *Clin. Neurophysiol.*, vol. 120, no. 11, pp. 1883–1908, Nov. 2009, doi: 10.1016/j.clinph.2009.07.045.

[52] T. W. Picton *et al.*, “Guidelines for using human event-related potentials to study cognition: Recording standards and publication criteria,” *Psychophysiology*, vol. 37, no. 2, pp. 127–152, Mar. 2000, doi: 10.1111/1469-8986.3720127.

[53] G. F. Woodman, “A brief introduction to the use of event-related potentials in studies of perception and attention,” *Atten. Percept. Psychophys.*, vol. 72, no. 8, pp. 2031–2046, Nov. 2010, doi: 10.3758/APP.72.8.2031.

[54] J. Polich, “Clinical application of the P300 event-related brain potential,” *Phys. Med. Rehabil. Clin. N. Am.*, vol. 15, no. 1, pp. 133–161, Feb. 2004, doi: 10.1016/S1047-9651(03)00109-8.

[55] W.-J. Huang, W.-W. Chen, and X. Zhang, “The neurophysiology of P 300--an integrated review.,” *Eur. Rev. Med. Pharmacol. Sci.*, vol. 19, no. 8, pp. 1480–8, Apr. 2015, [Online]. Available: http://www.ncbi.nlm.nih.gov/pubmed/25967724.

[56] K. A. Kiehl, K. R. Laurens, T. L. Duty, B. B. Forster, and P. F. Liddle, “Neural sources involved in auditory target detection and novelty processing: an event-related fMRI study.,” *Psychophysiology*, vol. 38, no. 1, pp. 133–42, Jan. 2001, [Online]. Available: http://www.ncbi.nlm.nih.gov/pubmed/11321614.

[57] R. T. Knight, “Contribution of human hippocampal region to novelty detection,” *Nature*, vol. 383, no. 6597, pp. 256–259, Sep. 1996, doi: 10.1038/383256a0.

[58] K. R. Daffner *et al.*, “The central role of the prefrontal cortex in directing attention to novel events,” *Brain*, vol. 123, no. 5, pp. 927–939, May 2000, doi: 10.1093/brain/123.5.927.

[59] K. R. Daffner, “Disruption of attention to novel events after frontal lobe injury in humans,” *J. Neurol. Neurosurg. Psychiatry*, vol. 68, no. 1, pp. 18–24, Jan. 2000, doi: 10.1136/jnnp.68.1.18.

[60] S. Berti, U. Roeber, and E. Schröger, “Bottom-Up Influences on Working Memory: Behavioral and Electrophysiological Distraction Varies with Distractor Strength,” *Exp. Psychol.*, vol. 51, no. 4, pp. 249–257, Jan. 2004, doi: 10.1027/1618-3169.51.4.249.

[61] F. T. Yilmaz, S. S. Özkaynak, and E. Barçin, “Contribution of auditory P300 test to the diagnosis of mild cognitive impairment in Parkinson’s disease,” *Neurol. Sci.*, vol. 38, no. 12, pp. 2103–2109, Dec. 2017, doi: 10.1007/s10072-017-3106-3.

[62] L. Batterink, C. M. Karns, and H. Neville, “Dissociable Mechanisms Supporting Awareness: The P300 and Gamma in a Linguistic Attentional Blink Task,” *Cereb. Cortex*, vol. 22, no. 12, pp. 2733–2744, Dec. 2012, doi: 10.1093/cercor/bhr346.

[63] N. Benz *et al.*, “Slowing of EEG background activity in Parkinson’s and Alzheimer’s disease with early cognitive dysfunction,” *Front. Aging Neurosci.*, vol. 6, Nov. 2014, doi: 10.3389/fnagi.2014.00314.

[64] I. Maidan *et al.*, “Changes in event-related potentials during dual task walking in aging and Parkinson’s disease,” *Clin. Neurophysiol.*, vol. 130, no. 2, pp. 224–230, Feb. 2019, doi: 10.1016/j.clinph.2018.11.019.

[65] T. W. Picton *et al.*, “Guidelines for using human event-related potentials to study cognition: recording standards and publication criteria.,” *Psychophysiology*, vol. 37, no. 2, pp. 127–52, Mar. 2000, [Online]. Available: http://www.ncbi.nlm.nih.gov/pubmed/10731765.

[66] B. R. Malcolm, J. J. Foxe, J. S. Butler, and P. De Sanctis, “The aging brain shows less flexible reallocation of cognitive resources during dual-task walking: A mobile brain/body imaging (MoBI) study,” *Neuroimage*, vol. 117, pp. 230–242, Aug. 2015, doi: 10.1016/j.neuroimage.2015.05.028.

[67] S. Fantini, B. Frederick, and A. Sassaroli, “Perspective: Prospects of non-invasive sensing of the human brain with diffuse optical imaging,” *APL Photonics*, vol. 3, no. 11, p. 110901, Nov. 2018, doi: 10.1063/1.5038571.

[68] R. C. Mesquita, M. A. Franceschini, and D. A. Boas, “Resting state functional connectivity of the whole head with near-infrared spectroscopy,” *Biomed. Opt. Express*, vol. 1, no. 1, p. 324, Aug.

2010, doi: 10.1364/BOE.1.000324.

[69] B. R. White *et al.*, “Resting-state functional connectivity in the human brain revealed with diffuse optical tomography,” *Neuroimage*, vol. 47, no. 1, pp. 148–156, Aug. 2009, doi: 10.1016/j.neuroimage.2009.03.058.

[70] Quaresima and Ferrari, “A Mini-Review on Functional Near-Infrared Spectroscopy (fNIRS): Where Do We Stand, and Where Should We Go?,” *Photonics*, vol. 6, no. 3, p. 87, Aug. 2019, doi: 10.3390/photonics6030087.

[71] C. Caballero-Gaudes and R. C. Reynolds, “Methods for cleaning the BOLD fMRI signal,” *Neuroimage*, vol. 154, pp. 128–149, Jul. 2017, doi: 10.1016/j.neuroimage.2016.12.018.

[72] F. Scholkmann *et al.*, “A review on continuous wave functional near-infrared spectroscopy and imaging instrumentation and methodology,” *Neuroimage*, vol. 85, pp. 6–27, Jan. 2014, doi: 10.1016/j.neuroimage.2013.05.004.

[73] S. M. Hernandez and L. Pollonini, “NIRSplot: A Tool for Quality Assessment of fNIRS Scans,” in *Biophotonics Congress: Biomedical Optics 2020 (Translational, Microscopy, OCT, OTS, BRAIN)*, 2020, p. BM2C.5, doi: 10.1364/BRAIN.2020.BM2C.5.

[74] T. Fekete, D. Rubin, J. M. Carlson, and L. R. Mujica-Parodi, “The NIRS Analysis Package: Noise Reduction and Statistical Inference,” *PLoS One*, vol. 6, no. 9, p. e24322, Sep. 2011, doi: 10.1371/journal.pone.0024322.

[75] G. Bauernfeind, S. C. Wriessnegger, I. Daly, and G. R. Müller-Putz, “Separating heart and brain: on the reduction of physiological noise from multichannel functional near-infrared spectroscopy (fNIRS) signals,” *J. Neural Eng.*, vol. 11, no. 5, p. 056010, Oct. 2014, doi: 10.1088/1741-2560/11/5/056010.

[76] F. Scholkmann, S. Spichtig, T. Muehlemann, and M. Wolf, “How to detect and reduce movement artifacts in near-infrared imaging using moving standard deviation and spline interpolation,” *Physiol. Meas.*, vol. 31, no. 5, pp. 649–662, May 2010, doi: 10.1088/0967-3334/31/5/004.

[77] S. Jahani, S. K. Setarehdan, D. A. Boas, and M. A. Yücel, “Motion artifact detection and correction in functional near-infrared spectroscopy: a new hybrid method based on spline interpolation method and Savitzky–Golay filtering,” *Neurophotonics*, vol. 5, no. 01, p. 1, Feb. 2018, doi: 10.1117/1.NPh.5.1.015003.

[78] Y. Zhang, D. H. Brooks, M. A. Franceschini, and D. A. Boas, “Eigenvector-based spatial filtering for reduction of physiological interference in diffuse optical imaging,” *J. Biomed. Opt.*, vol. 10, no. 1, p. 011014, 2005, doi: 10.1117/1.1852552.

[79] S. Brigadoi *et al.*, “Motion artifacts in functional near-infrared spectroscopy: A comparison of motion correction techniques applied to real cognitive data,” *Neuroimage*, vol. 85, pp. 181–191, Jan. 2014, doi: 10.1016/j.neuroimage.2013.04.082.

[80] T. J. Huppert, S. G. Diamond, M. A. Franceschini, and D. A. Boas, “HomER: a review of time-series analysis methods for near-infrared spectroscopy of the brain,” *Appl. Opt.*, vol. 48, no. 10, p. D280, Apr. 2009, doi: 10.1364/AO.48.00D280.

[81] J. YE, S. TAK, K. JANG, J. JUNG, and J. JANG, “NIRS-SPM: Statistical parametric mapping for near-

infrared spectroscopy," *Neuroimage*, vol. 44, no. 2, pp. 428–447, Jan. 2009, doi: 10.1016/j.neuroimage.2008.08.036.

[82] T. Sato *et al.*, "Reduction of global interference of scalp-hemodynamics in functional near-infrared spectroscopy using short distance probes," *Neuroimage*, vol. 141, pp. 120–132, Nov. 2016, doi: 10.1016/j.neuroimage.2016.06.054.

[83] H. Santosa, X. Zhai, F. Fishburn, P. J. Sparto, and T. J. Huppert, "Quantitative comparison of correction techniques for removing systemic physiological signal in functional near-infrared spectroscopy studies," *Neurophotonics*, vol. 7, no. 03, Sep. 2020, doi: 10.1117/1.NPh.7.3.035009.

[84] S. Tak and J. C. Ye, "Statistical analysis of fNIRS data: A comprehensive review," *Neuroimage*, vol. 85, pp. 72–91, Jan. 2014, doi: 10.1016/j.neuroimage.2013.06.016.

[85] A. M. Chiarelli, E. L. Maclin, M. Fabiani, and G. Gratton, "A kurtosis-based wavelet algorithm for motion artifact correction of fNIRS data," *Neuroimage*, vol. 112, pp. 128–137, May 2015, doi: 10.1016/j.neuroimage.2015.02.057.

[86] P. Pinti, F. Scholkmann, A. Hamilton, P. Burgess, and I. Tachtsidis, "Current Status and Issues Regarding Pre-processing of fNIRS Neuroimaging Data: An Investigation of Diverse Signal Filtering Methods Within a General Linear Model Framework," *Front. Hum. Neurosci.*, vol. 12, Jan. 2019, doi: 10.3389/fnhum.2018.00505.

[87] X. CHEN, Z. WU, and N. E. HUANG, "THE TIME-DEPENDENT INTRINSIC CORRELATION BASED ON THE EMPIRICAL MODE DECOMPOSITION," *Adv. Adapt. Data Anal.*, vol. 02, no. 02, pp. 233–265, Apr. 2010, doi: 10.1142/S1793536910000471.

[88] C. M. Sweeney-Reed, S. J. Nasuto, M. F. Vieira, and A. O. Andrade, *Empirical Mode Decomposition and its Extensions Applied to EEG Analysis: A Review*, vol. 10, no. 02. 2018.

[89] D. Patashov, D. Goldstein, and M. Balberg, "Homologous Connectivity Maps Can Discriminate Diseased from Healthy Brains," in *Biophotonics Congress: Optics in the Life Sciences Congress 2019 (BODA,BRAIN,NTM,OMA,OMP)*, 2019, p. BW4A.3, doi: 10.1364/BRAIN.2019.BW4A.3.

[90] P. T. K. Chi, V. N. Tuan, N. H. Thuong, H. T. K. Khanh, H. Yu, and N. D. Thang, "Noise Removal of Functional Near Infrared Spectroscopy Signals Using Emperical Mode Decomposition and Independent Component Analysis," 2018, pp. 925–929.

[91] Y. Gu, J. Han, Z. Liang, J. Yan, Z. Li, and X. Li, "Empirical mode decomposition-based motion artifact correction method for functional near-infrared spectroscopy," *J. Biomed. Opt.*, vol. 21, no. 1, p. 015002, Jan. 2016, doi: 10.1117/1.JBO.21.1.015002.

[92] H. Santosa, X. Zhai, F. Fishburn, and T. Huppert, "The NIRS Brain AnalyzIR Toolbox," *Algorithms*, vol. 11, no. 5, p. 73, May 2018, doi: 10.3390/a11050073.

[93] J. Mehnert *et al.*, "Developmental changes in brain activation and functional connectivity during response inhibition in the early childhood brain," *Brain Dev.*, vol. 35, no. 10, pp. 894–904, Nov. 2013, doi: 10.1016/j.braindev.2012.11.006.

[94] Z. S. Nasreddine *et al.*, "The Montreal Cognitive Assessment, MoCA: A Brief Screening Tool For Mild Cognitive Impairment," *J. Am. Geriatr. Soc.*, vol. 53, no. 4, pp. 695–699, Apr. 2005, doi: 10.1111/j.1532-5415.2005.53221.x.

[95] K. Gramann, J. T. Gwin, N. Bigdely-Shamlo, D. P. Ferris, and S. Makeig, "Visual Evoked Responses During Standing and Walking," *Front. Hum. Neurosci.*, vol. 4, 2010, doi: 10.3389/fnhum.2010.00202.

[96] A. Delorme and S. Makeig, "EEGLAB: an open source toolbox for analysis of single-trial EEG dynamics including independent component analysis," *J. Neurosci. Methods*, vol. 134, no. 1, pp. 9–21, Mar. 2004, doi: 10.1016/j.jneumeth.2003.10.009.

[97] J. T. Gwin, K. Gramann, S. Makeig, and D. P. Ferris, "Removal of Movement Artifact From High-Density EEG Recorded During Walking and Running," *J. Neurophysiol.*, vol. 103, no. 6, pp. 3526–3534, Jun. 2010, doi: 10.1152/jn.00105.2010.

[98] J. Polich, "Updating P300: An integrative theory of P3a and P3b," *Clin. Neurophysiol.*, vol. 118, no. 10, pp. 2128–2148, Oct. 2007, doi: 10.1016/j.clinph.2007.04.019.

[99] R. M. Sakia, "The Box-Cox Transformation Technique: A Review," *Stat.*, vol. 41, no. 2, p. 169, 1992, doi: 10.2307/2348250.

[100] J. M. Barden, C. A. Clermont, D. Kobsar, and O. Beauchet, "Accelerometer-Based Step Regularity Is Lower in Older Adults with Bilateral Knee Osteoarthritis," *Front. Hum. Neurosci.*, vol. 10, Dec. 2016, doi: 10.3389/fnhum.2016.00625.

[101] N. E. Huang, *Hilbert–Huang Transform and Its Applications*. 2014.

[102] J. A. Urigüen and B. Garcia-Zapirain, "EEG artifact removal—state-of-the-art and guidelines," *J. Neural Eng.*, vol. 12, no. 3, p. 031001, Jun. 2015, doi: 10.1088/1741-2560/12/3/031001.

[103] D. Trojaniello, A. Cereatti, A. Ravaschio, M. Bandettini, and U. Della Croce, "Assessment of gait direction changes during straight-ahead walking in healthy elderly and Huntington Disease patients using a shank worn MIMU," in *2014 36th Annual International Conference of the IEEE Engineering in Medicine and Biology Society*, Aug. 2014, pp. 2508–2511, doi: 10.1109/EMBC.2014.6944132.

[104] G. G. Roussas, *An Introduction to Probability and Statistical Inference*. Elsevier, 2015.

[105] J. Gillard, *A First Course in Statistical Inference*. Cham: Springer International Publishing, 2020.

[106] M. Ahsanullah, *Extreme Value Distributions*, vol. 8. Paris: Atlantis Press, 2016.

[107] K. E. Jang, S. Tak, J. Jung, J. Jang, Y. Jeong, and J. C. Ye, "Wavelet minimum description length detrending for near-infrared spectroscopy," *J. Biomed. Opt.*, vol. 14, no. 3, p. 034004, 2009, doi: 10.1117/1.3127204.

[108] D. Patashov, Y. Menahem, Y. Kameda, D. Goldstein, and M. Balberg, "fNIRS Artifact Removal Using Selective Source Separation," in *Biophotonics Congress: Optics in the Life Sciences Congress 2021, OSA Technical Digest (Optical Society of America)*, 2021, p. BF1B.2.

Presentations

<1> fNIRS Artifact Removal Using Selective Source Separation; Patashov Dmitry, Menahem Yakir, Kameda Yoshinari, Goldstein Dmitry, Balberg Michal; Type: Oral Presentation; *OSA Biophotonics Congress: Optics in the Life Sciences*; Virtual Conference, USA; 12-16.04.2021;

<2> Artifact detection based on statistical properties; Patashov Dmitry, Menahem Yakir, Kameda Yoshinari, Goldstein Dmitry, Balberg Michal; Type: Oral Presentation; *fNIRS Datablitz 2020*; Virtual Conference, Boston, USA; The Society for functional Near Infrared Spectroscopy; 12-14.10.2020;

<3> The effects of dual tasking and aging on event related potential (ERP) components of gait cycle; Inbal Maidan, Shiran Shustak, Dmitry Patashov, Eran Gazit, Boris Shapiro, Aviran Levy, Nir Giladi, Jeff Hausdorff, Anat Mirelman; Type: Oral Presentation; *The International Society of Posture and Gait Research*; Edinburgh International Conference Centre, Edinburgh, United Kingdom; ISPGR; 30.06-04.07.2019

<4> Homologous Connectivity Maps Can Discriminate Diseased from Healthy Brains; Dmitry Patashov, Dmitry Goldstein, Michal Balberg; Type: Oral Presentation; *OSA Biophotonics Congress: Optics in the Life Sciences*; Loews Ventana Canyon Resort, Tucson, Arizona, USA; 14-17.04.2019

<5> Near Infrared Assessment of Brain Disease; D.Patashov, Y.Menahem, G.Gurevitch, T.Handler, D.Goldstein, M.Balberg; Type: Poster Presentation; *IBT - Israel Brain Technologies: BrainTech 2019, 4th International Brain Technology Conference*; InterContinental David, Tel Aviv, Israel; 04-05.03.2019

<6> The effects of dual tasking and aging on event related potential (ERP) components of gait cycle; *Maidan I, *Patashov D, Shustak S, Gazit E, Shapiro B, Levy A, Sosnik R, Giladi N, Hausdorff JM, Mirelman A; *Authors with equal contribution; Type: Poster Presentation; *IBT - Israel Brain Technologies: BrainTech 2019, 4th International Brain Technology Conference*; InterContinental David, Tel Aviv, Israel; 04-05.03.2019

<7> fNIRS and fMRI Comparison in Healthy Subjects and Patients with Brain Disease; D.Patashov, D.Tchertov, E.Tzdaka, Y.Zamir, G.Gurevitch, T.Handler, D.Goldstein, M.Balberg; Type: Poster Presentation; *fNIRS 2018, Biennial meeting of the Society for fNIRS;* University of Tokyo, central Tokyo, Tokyo, Japan; 05-08.10.2018

<8> Development of a method to identify walking pattern and performance in a virtual reality obstacle course; Patashov Dmitry, Ben-Haim Ohad, Yakobi Shelly, Gazit Eran, Maidan Inbal, Mirelman Anat, Goldstein Dmitry, Hausdorff JM; Type: Poster Presentation; *ISMBE 2016, International conference on Biomedical Engineering;* International Convention Center, Haifa, Israel; 24.02.2016

Publications

Peer Reviewed Journal Articles:

<1> Methods for Gait Analysis During Obstacle Avoidance Task; Patashov Dmitry, Menahem Yakir, Ben-Haim Ohad, Gazit Eran, Maidan Inbal, Mirelman Anat, Sosnik Ronen, Goldstein Dmitry, Hausdorff Jeffrey M; Springer; *Annals of Biomedical Engineering; DOI: 10.1007/s10439-019-02380-4;*

<2> A new approach to quantifying the EEG during walking: Initial evidence of gait related potentials and their changes with aging and dual tasking; *Maidan I, *Patashov D, Shustak S, Fahoum F, Gazit E, Shapiro B, Levy A, Sosnik R, Giladi N, Hausdorff JM, Mirelman A; *Authors with equal contribution; Elsevier; Experimental Gerontology; DOI: 10.1016/j.exger.2019.110709;

<3> Changes in brain response (ERP) during dual task walking in aging and in Parkinson's disease; Inbal Maidan, PhD; Firas Fahoum, MD; Shiran Shustak, BSc; Eran Gazit, MSc; Dmitry Patashov, BSc; Dmitry Tchertov, BSc; Nir Giladi, MD; Jeffrey M Hausdorff, PhD; Anat Mirelman, PhD; Elsevier; Clinical Neurophysiology; DOI: 10.1016/j.clinph.2018.11.019;

Peer Reviewed Conference Papers:

<1> fNIRS Artifact Removal Using Selective Source Separation; Patashov Dmitry, Menahem Yakir, Kameda Yoshinari, Goldstein Dmitry, Balberg Michal; Biophotonics Congress: Optics in the Life Sciences Congress 2021, The Optical Society of America, 2021, paper BF1B.2;

<2> Homologous Connectivity Maps Can Discriminate Diseased from Healthy Brains; Dmitry Patashov, Dmitry Goldstein, Michal Balberg; Biophotonics Congress: Optics in the Life Sciences Congress 2019, The Optical Society of America, 2019, paper BW4A.3; DOI: 10.1364/BRAIN.2019.BW4A.3;

Main Author Publications

<1> fNIRS Artifact Removal Using Selective Source Separation; Patashov Dmitry, Menahem Yakir, Kameda Yoshinari, Goldstein Dmitry, Balberg Michal; Biophotonics Congress: Optics in the Life Sciences Congress 2021, The Optical Society of America, 2021, paper BF1B.2;

<2> Methods for Gait Analysis During Obstacle Avoidance Task; Patashov Dmitry, Menahem Yakir, Ben-Haim Ohad, Gazit Eran, Maidan Inbal, Mirelman Anat, Sosnik Ronen, Goldstein Dmitry, Hausdorff Jeffrey M; Springer; *Annals of Biomedical Engineering; DOI: 10.1007/s10439-019-02380-4;*

<3> A new approach to quantifying the EEG during walking: Initial evidence of gait related potentials and their changes with aging and dual tasking; *Maidan I, *Patashov D, Shustak S, Fahoum F, Gazit E, Shapiro B, Levy A, Sosnik R, Giladi N, Hausdorff JM, Mirelman A; *Authors with equal contribution; Elsevier; Experimental Gerontology; DOI: 10.1016/j.exger.2019.110709;

<4> Homologous Connectivity Maps Can Discriminate Diseased from Healthy Brains; Dmitry Patashov, Dmitry Goldstein, Michal Balberg; Biophotonics Congress: Optics in the Life Sciences Congress 2019, The Optical Society of America, 2019, paper BW4A.3; DOI: 10.1364/BRAIN.2019.BW4A.3;